Dynamics of underground gas storage. Insights from numerical models for carbon dioxide and hydrogen.

Alvaro A. Sainz-Garcia

To cite this version:

Alvaro A. Sainz-Garcia. Dynamics of underground gas storage. Insights from numerical models for carbon dioxide and hydrogen.. Applied geology. Université Toulouse 3 Paul Sabatier (UT3 Paul Sabatier), 2017. English. NNT : . tel-01703296

HAL Id: tel-01703296
https://theses.hal.science/tel-01703296

Submitted on 7 Feb 2018

Université Fédérale
Toulouse Midi-Pyrénées

THÈSE

En vue de l'obtention du

DOCTORAT DE L'UNIVERSITÉ DE TOULOUSE

Délivré par :

Université Toulouse 3 Paul Sabatier (UT3 Paul Sabatier)

Présentée et soutenue par :
Álvaro Sáinz-García
le lundi 16 octobre 2017

Titre :

Dynamique de stockage souterrain de gaz. Aperçu à partir de modèles numeriques de dioxyde de carbone et d'hydrogène

---

École doctorale et discipline ou spécialité :
ED SDU2E : Surfaces et interfaces continentales, Hydrologie

Unité de recherche :
GET - Laboratoire Geosciences Environnement Toulouse

Directeur/trice(s) de Thèse :

Dr. Eric H. Oelkers
Dr. Fidel Grandia

Jury :
Dr. Vincent Lagneau - Rapporteur
Dr. Pascal Audigane - Rapporteur
Dr. Catherine Noiriel - Examinateur
Dr. Josep Soler - Examinateur
Dr. Eric H. Oelkers - Directeur de these
Dr. Fidel Grandia - Directeur de these

Abstract

Climate change mitigation is one of the major challenges of our time. The anthropogenic greenhouse gases emissions have continuously increased since industrial revolution leading to global warming. A broad portfolio of mitigation technologies has to be implemented to fulfill international greenhouse gas emissions agreements. Some of them comprises the use of the underground as a storage of various substances. In particular, this thesis addresses the dynamics of carbon dioxide (CO_2) and hydrogen (H_2) underground storage.

Numerical models are a very useful tool to estimate the processes taking place at the subsurface. During this thesis, a solute transport in porous media module and various multiphase flow formulations have been implemented in COMSOL Multiphysics (Comsol, 2016). These numerical tools help to progress in the understanding of the migration and interaction of fluids in porous underground storages.

Three models that provide recommendations to improve the efficiency, monitoring and safety of the storages are presented in this manuscript: two in the context of carbon capture and storage (CCS) and one applied to underground hydrogen storage (UHS). Each model focus on a specific research question:

Multiphase model on CCS. The efficiency and long-term safety of underground CO_2 storage depend on the migration and trapping of the buoyant CO_2 plume. The wide range of temporal and spatial scales involved poses challenges in the assessment of the trapping mechanisms and the interaction between them. In this chapter a two-phase dynamic numerical model able to capture the effects of capillarity, dissolution and convective mixing on the plume migration is applied to a syncline-anticline aquifer structure. In anticline aquifers, the slope of the aquifer and the distance of injection to anticline crest determine the gravity current migration and, thus, the trapping mechanisms affecting the CO_2. The anticline structure halts the gravity current and promotes free-phase CO_2 accumulation beneath the anticline crest, stimulating the onset of convection and, thus, accelerating CO_2 dissolution. Variations on the gravity current velocity due to the anticline slope can lead to plume splitting and different free-phase plume depletion time is observed depending on the injection location. Injection at short distances from the anticline crest minimizes the plume extent but retards CO_2 immobilization. On the contrary, injection at large distances from anticline crest leads

to large plume footprints and the splitting of the free-phase plume. The larger extension yields higher leakage risk than injection close to aquifer tip; however, capillary trapping is greatly enhanced, leading to faster free-phase CO_2 immobilization.

Reactive transport model on convective mixing in CCS. Dissolution of carbon-dioxide into formation fluids during carbon capture and storage (CCS) can generate an instability with a denser CO_2-rich fluid located above the less dense native aquifer fluid. This instability promotes convective mixing, enhancing CO_2 dissolution and favouring the storage safety. Convective mixing has been extensively analysed in the context of CCS over the last decade, however, the interaction between convective mixing and geochemistry has been insufficiently addressed. This relation is explored using a fully coupled model taking account the porosity and permeability variations due to dissolution-precipitation reactions in a realistic geochemical system based on the Hontomín (Spain) CCS pilot site project. This system, located in a calcite, dolomite, and gypsum bearing host rock, has been analyzed for a variety of Rayleigh and Damköhler values. Results show that chemical reactions tend to enhance CO_2 dissolution. The model illustrates the first stages of porosity channel development, demonstrating the significance of fluid mixing in the development of porosity patterns. The influence of non-carbon species on CO_2 dissolution shown in this study demonstrates the needs for realistic chemical and kinetic models to ensure the precision of physical models to accurately represent the carbon-dioxide injection process.

Multiphase model applied to seasonal UHS in northern Spain. A major disadvantage of renewable energies is their fluctuation, that can lead to temporary mismatches between demand and supply. The conversion of surplus energy to hydrogen and its storage in the underground is one of the options to balance this energy gap. This study evaluates the seasonal storage of hydrogen produced from wind power in Castilla-León region (northern Spain). An actual saline aquifer is analysed by means of a 3D multiphase numerical model. Different extraction well configurations are explored during three years of injection-production cycles. Results demonstrates that underground hydrogen storage in saline aquifers can be operated with reasonable recovery ratios: a maximum hydrogen recovery ratio of 78%, which leads to a global energy efficiency of 30%, has been estimated. Upconing emerge as the major risk on saline aquifer storage; however, extraction wells located in the upper part of the aquifer can deal with its effects. Steeply

dipping geological structures appears as a critical requisite for an efficient hydrogen storage.

Keywords: Geological gas storage, Numerical modelling, Multiphase flow, Reactive transport, Carbon capture and storage, Underground hydrogen storage

Résumé

L'atténuation du changement climatique est l'un des défis majeurs de notre époque. Les émissions anthropiques de gaz à effet de serre ont augmenté de façon continue depuis la révolution industrielle, provoquant le réchauffement climatique. Un ensemble de technologies très diverses doivent être mises en œuvre pour respecter les accords internationaux relatifs aux émissions de gaz à effet de serre. Certaines d'entre elles ont recours au sous-sol pour le stockage de diverses substances. Cette thèse traite plus particulièrement de la dynamique du stockage souterrain du dioxyde de carbone (CO_2) et de l'hydrogène (H_2).

Des modèles numériques de transport réactif et multiphasiques ont été élaborés pour mieux comprendre la migration et les interactions des fluides dans des milieux poreux de stockage souterrain. Ils fournissent des recommandations pour améliorer l'efficacité, la surveillance et la sécurité du stockage. Trois modèles sont présentés dans ce document, dont deux dans le domaine du captage et du stockage du CO_2 (CCS pour *Carbon Capture and Storage*), et le troisième s'appliquant au stockage souterrain de l'hydrogène (UHS pour *Underground Hydrogen Storage*). Chacun d'entre eux traite plus spécifiquement un aspect de la recherche :

Modèle multiphasique appliqué au CCS L'efficacité et la sécurité à long terme du stockage du CO_2 dépend de la migration et du piégeage du panache de CO_2 flottant. Les grandes différences d'échelles temporelles et spatiales concernées posent de gros problèmes pour évaluer les mécanismes de piégeage et leurs interactions. Dans cet article, un modèle numérique dynamique diphasique a été appliqué à une structure aquifère synclinale-anticlinale. Ce modèle est capable de rendre compte des effets de capillarité, de dissolution et de mélange convectif sur la migration du panache. Dans les aquifères anticlinaux, la pente de l'aquifère et la distance de l'injection à la crête de l'anticlinal déterminent la migration du courant gravitaire et, donc, les mécanismes de piégeage affectant le CO_2. La structure anticlinale arrête le courant gravitaire et facilite l'accumulation du CO_2 en phase libre, en dessous de la crête de l'anticlinal, ce qui stimule la mise en place d'une convection et accélère donc la dissolution du CO_2. Les variations de vitesse du courant gravitaire en raison de la pente de l'anticlinal peuvent provoquer la division du panache et une durée différente de résorption du panache en phase libre, qui dépend de l'endroit de l'injection. L'injection à faible distance de la crête de

l'anticlinal minimise la taille du panache mais retarde l'immobilisation du CO_2. Au contraire, l'injection à grande distance de la crête de l'anticlinal crée des panaches à empreinte étendue et leur division en plusieurs panaches en phase libre. Plus la distance à la crête est grande, plus le risque de fuite augmente. Cependant, elle favorise grandement le piégeage par capillarité, qui résulte en une immobilisation plus rapide du CO_2 en phase libre.

Modèle de transport réactif sur les mélanges convectifs en CCS. La dissolution du dioxyde de carbone dans des fluides de la formation pendant le captage et le stockage (CCS) peut générer une instabilité lorsqu'un fluide riche en CO_2 plus dense se trouve au-dessus du fluide de moindre densité existant dans l'aquifère. Cette instabilité favorise le mélange convectif, augmente la dissolution du CO_2 et va dans le sens d'une meilleure sécurité du stockage. Le mélange convectif a été largement étudié dans le domaine du CCS durant la dernière décennie, mais les interactions entre le mélange convectif et la géochimie restent insuffisamment traitées. Cette relation est examinée à l'aide d'un modèle totalement couplé, qui prend en compte les variations de porosité et de perméabilité dues aux réactions de dissolution-précipitation dans un système géochimique réaliste, sur la base du projet relatif au site CCS potentiel à Hontomín, en Espagne. Ce système se trouve dans une roche hôte constituée de gypse, de dolomite et de calcite. Il a été analysé et de nombreuses valeurs Rayleigh et Damköhler ont été relevées. Les résultats montrent que les réactions chimiques tendent à accroître la dissolution du CO_2. Le modèle illustre les premières étapes du développement d'un chenal de porosité, ce qui démontre l'importance du mélange convectif dans le développement de motifs de porosité. L'influence de composés inorganiques sur la dissolution du CO_2 constatée dans cette étude, démontre le besoin de modèles cinétiques et chimiques réalistes, permettant aux modèles physiques de représenter avec précision le processus d'injection du dioxyde de carbone.

Modèle multiphasique appliqué à l'UHS saisonnière dans le nord de l'Espagne. L'un des plus grands inconvénients des énergies renouvelables est qu'ils présentent des fluctuations, entraînant des déséquilibres entre la demande et l'approvisionnement en électricité. La transformation en hydrogène de l'énergie en excès et son stockage dans le sous-sol représente l'une des solutions pour y pallier. Cette étude évalue le stockage de l'hydrogène obtenu à partir de la production éolienne dans la région de Castille-et-

León, dans le nord de l'Espagne. Un aquifère salin est analysé à l'aide d'un modèle numérique multiphasique en 3D. Différentes configurations de puits d'extraction sont étudiées sur une période de trois ans de cycles d'injection-production. Les résultats montrent que le stockage souterrain de l'hydrogène dans les aquifères salins peut être exploité avec des taux de récupération raisonnables. Un taux maximal de récupération de l'hydrogène de 78 % a été atteint, ce qui correspond à une efficacité énergétique globale de 30 %. Le risque majeur posé par le stockage en aquifère salin est l'intrusion, qui peut cependant être évitée en situant les puits d'extraction à proximité de la surface supérieure de l'aquifère. Des structures géologiques à fort pendage semblent constituer un critère essentiel d'efficacité d'un stockage d'hydrogène.

Mots clés: Stockage géologique du gaz, Modélisation numérique, Transport réactifs, Flux multiphasique, Captage au stockage du CO_2, Stockage souterrain de l'hydrogen

Acknowledgments

The research leading to this PhD. manuscript has received funding from the CO2-REACT People Programme (Marie Curie Actions) of the European Union's Seventh Framework Programme FP7-2012-ITN under REA grant agreement n° 317235.

I would like to thank my supervisors Dr. Fidel Grandia and Dr. Eric Oelkers for their encouragement, guidance and support. My sincere thanks to Dr. Elena Abarca and Albert Nardi for their constant help and exceptional interest on science and to the colleagues of the CO2-REACT ITN, especially to Martin Voigt and Christian Grimm who have guided and helped me with the endless paperwork at the university.

I also want to thank Roberto Martínez-Orío from IGME (Instituto Geológico y Minero de España) for his support in the collection of the geological data used in the section 3.2 of this manuscript.

Last but not least, I want to thank those who have accompanied me during the development of the thesis, from near or from afar, but always with trust, support and joy.

Table of contents

List of figures

List of tables

1 Introduction

Climate change mitigation is one of the major challenges of our time. The anthropogenic greenhouse gases emissions have continuously increased since the industrial revolution (Stocker et al., 2013), leading to global warming. Over the past decades, the atmosphere and ocean temperature have risen, the amount of snow and ice have diminished and sea level has increased, demonstrating unequivocally the warming of the climate systems (Figure 1-1) (Stocker et al., 2013). International agreements (European Commission, 2012, 2010; Kioto Protocol, 1997; Paris Agreement, 2015; Rio Summit, 1992) highlight the necessity to take climate protection actions.

A broad portfolio of technologies has to be implemented to mitigate global warming. The increase of renewable energy generation, the implementation of carbon capture and storage, the use of nuclear power and the improvement of energy efficiency are the most promising options to reduce greenhouse gases emissions (Edenhofer et al., 2014). Most of these, use subsurface environments as a storage of various substances (i.e. nuclear waste repositories, underground carbon reservoirs...). In particular, this thesis analyzes the dynamics of underground gas storage for carbon dioxide (CO_2) and hydrogen (H_2).

Carbon capture and storage (CCS) consist of capturing waste carbon dioxide from large point sources (i.e. fossil fuel power plants, cement industries...), transporting it and storing it into underground geological formations (Metz et al., 2005). The CO_2 should be confined in the subsurface for a long time period (around 1000 years), preventing the release of carbon dioxide to the atmosphere. Underground hydrogen storage (UHS) comprises the injecting of a fluid (H_2) into the subsurface as well, but in a different time scale. The purpose is to use hydrogen storage as grid energy storage. Hydrogen is a suitable energy vector that can be produced from surplus energy from renewables (energy generated that exceeds the immediate needs of the electricity grid); stored in the subsurface and extracted during periods of energy shortage. This can be used to balance the mismatches between energy demand and supply due to renewable energies fluctuation.

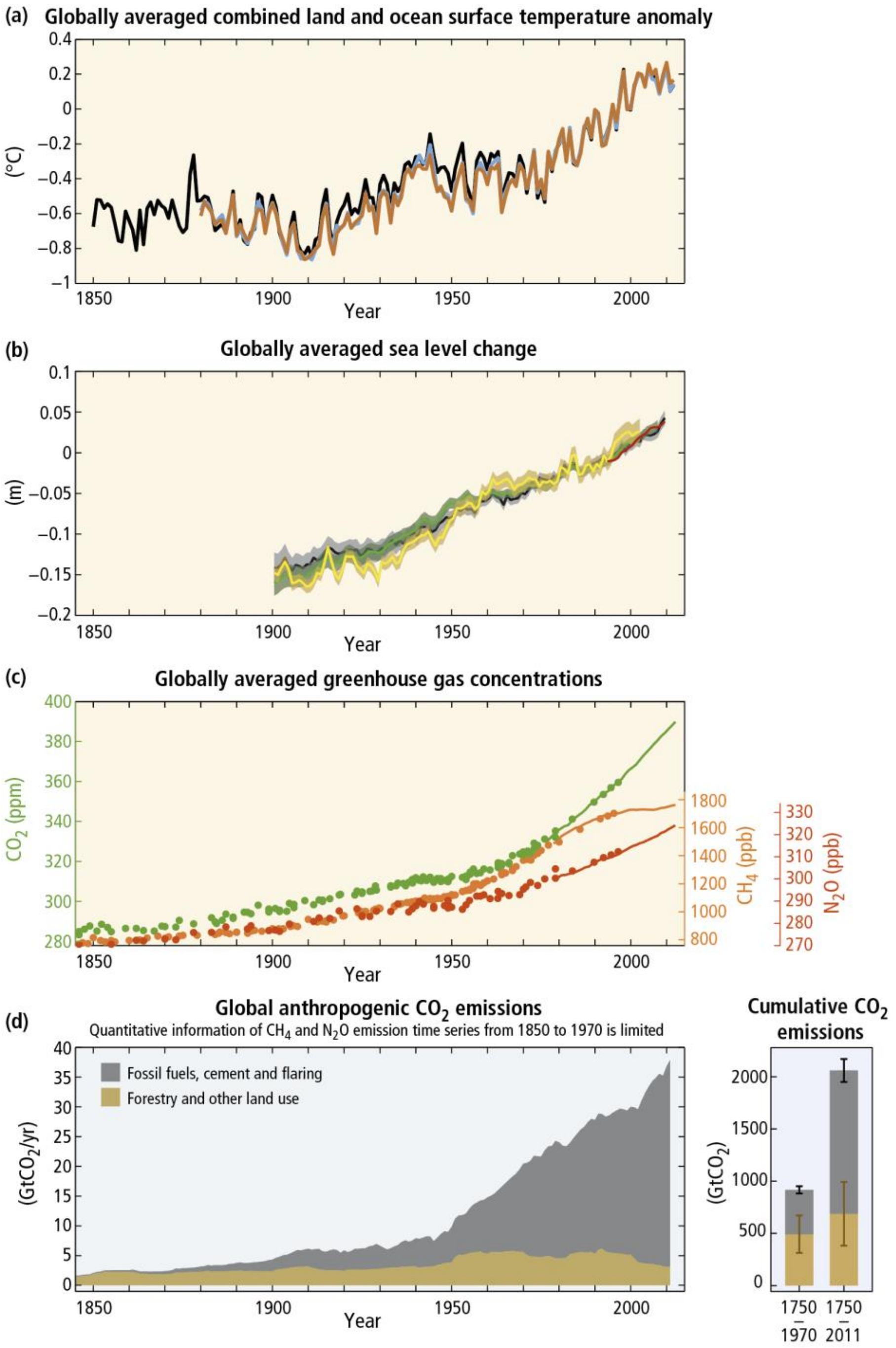

Figure 1-1. Reprint of the Figure SPM.1 of the 5th IPCC Synthesis Report (Pachauri et al., 2014) showing evidences and other indicators of a changing global climate system. Observations: (a) Annually and globally averaged combined land and ocean surface temperature anomalies relative to the average over the period 1986 to 2005. Colours indicate different data sets. (b) Annually and globally averaged sea level change relative to the average over the period 1986 to 2005 in the longest-running dataset. Colours indicate different data sets. All datasets are aligned to have the same value in 1993, the first year of satellite altimetry data (red). Where assessed, uncertainties are indicated by coloured shading. (c) Atmospheric concentrations of the greenhouse gases carbon dioxide (CO_2, green), methane (CH_4, orange) and nitrous oxide (N_2O, red) determined from ice core data (dots) and from direct atmospheric measurements (lines). Indicators: (d) Global anthropogenic CO_2 emissions from forestry and other land use as well as from burning of fossil fuel, cement production and flaring. Cumulative emissions of CO_2 from these sources and their uncertainties are shown as bars and whiskers, respectively, on the right hand side. The global effects of the accumulation of CH4 and N2O emissions are shown in panel c.

Despite the differences in the ultimate goal of the storage and the consequent contrasting time scales, both underground storage efforts share many aspects. For instance, the injection of a fluid phase in the subsurface, each with distinct physical and chemical properties than the native fluids, leads to the development of an interface between the phases with the subsequent capillary pressure. Factors such as the saturation or the effective permeability of the phases should be taken into account in multiphase flow conditions. Furthermore, the fluids injected in CCS and UHS operations are less dense and viscous than the native fluids; leading to their upward migration. An impervious overlaying seal is, thus, needed to ensure the confinement of the fluid within the geological formation. Other characteristics including high permeability, sufficient porosity and large volume capacity, which is indeed the main reason for considering underground storages, should be fulfilled by the underground storage structures. These similarities allow the transfer of knowledge from the extensively investigated carbon capture and storage field to the less mature field of underground hydrogen storage.

The dynamics of the gas once injected in the subsurface and their impact on the host aquifer are complex to monitor since storage formations are generally found at large depths (>500 m) hindering fluid and rock analysis through time. The alternative, although being very expensive, is time-lapse geophysics such as electrical tomography, magnetotelluric and seismic methods. Such limitations in these data acquisition methods makes predictive numerical models a very useful tool to estimate the processes taking place at the subsurface. In this work, the fate of injected gases in porous media will be analysed using multiphase and reactive transport numerical models.

The development of this thesis comprised the improvement of several computational tools. A solute transport in porous media module and various multiphase flow formulations have been implemented in COMSOL Multiphysics (Comsol, 2016). The solute transport module has been tailored to meet the necessities of the reactive transport code iCP (Nardi et al., 2014a). iCP integrates COMSOL and PHREEQC (Parkhurst and Appelo, 2013), allowing the simulation of complex thermo-hydro-mechanical-chemical (THMC) processes. These tools have been, then, used to better understand the migration and interaction of fluids in porous underground storages; providing recommendations to improve the efficiency, monitoring and safety of the storages.

The thesis has been divided into five chapters. Chapter 2 describes the numerical tools implemented during this thesis. The mathematical and numerical approaches applied are explained together with some verification examples. Chapter 3 deals with the dynamics of CO_2 in the subsurface in the context of CCS projects. It includes two sections: the first analyses the interactions of CO_2 gravity currents, capillarity, dissolution and convective mixing using a miscible multiphase model; the second evaluates the influence of reactions on convective mixing fingers and CO_2 dissolution using a fully coupled reactive transport model. Chapter 4 is focused on the storage of hydrogen produced from surplus energy in Castilla-León (north Spain). This chapter estimates the amount of H_2 that can be recovered from an aquifer applying an immiscible two-phase model. Finally, the major findings of the research, together with some general conclusions and future perspectives are presented in Chapter 5.

In addition to the numerical models of underground gas storage presented in chapters 3 and 4, other activities have been developed in the course of this thesis as an effort to better understand the challenges and risks of the options to mitigate the climate change. Special efforts have been made on the analysis of natural occurring CO_2 fluxes arriving to the surface. These systems give insights on the migration of CO_2 at the near surface and atmosphere and on its effects on the ecosystems. Three studies based on field sampling aiming to evaluate monitoring techniques for the early detection of CO_2 leakages and risk assessment methodologies are presented in Annex I.

1.1 Introduction en français

L'atténuation du changement climatique est l'un des défis majeurs de notre époque. Les émissions anthropiques de gaz à effet de serre ont augmenté de façon continue depuis la révolution industrielle (Stocker et al., 2013), provoquant le réchauffement climatique. Durant les dernières décennies, les températures de l'atmosphère et des océans ont augmenté, les quantités de neige et de glace ont diminué et le niveau des mers a monté, démontrant sans équivoque le réchauffement du système climatique (Figure 1-1) (Stocker et al., 2013). Des accords internationaux (European Commission, 2012, 2010; Kioto Protocol, 1997; Paris Agreement, 2015; Rio Summit, 1992) insistent sur la nécessité d'agir pour protéger le climat.

De nombreuses technologies très diverses doivent être mises en œuvre pour atténuer le réchauffement climatique global. L'augmentation de la production d'électricité à partir d'énergies renouvelables, la mise en place du captage et du stockage du CO_2, l'utilisation de l'énergie nucléaire et l'amélioration de l'efficacité énergétique sont les solutions les plus prometteuses pour la réduction des émissions de gaz à effet de serre (Edenhofer et al., 2014). La plupart d'entre elles utilisent des sites souterrains pour le stockage de diverses substances (comme les sites d'enfouissement des déchets nucléaires, les puits de carbone, etc.). Cette thèse traite plus particulièrement de la dynamique du stockage gazier souterrain pour le dioxyde de carbone (CO_2) et l'hydrogène (H_2).

Le captage et stockage du CO_2 (CCS) consiste à capter le dioxyde de carbone émis par de grandes sources (comme les centrales électriques à combustible fossile, les cimenteries, etc.), à le transporter et à le stocker dans des formations géologiques souterraines (Metz et al., 2005). Le CO_2 doit être confiné dans le sous-sol pendant une longue période (de l'ordre de 1000 ans), empêchant ainsi sa libération dans l'atmosphère. Le stockage souterrain de l'hydrogène (UHS) consiste également à injecter un fluide (H_2) dans le sous-sol, mais pour une période différente. Le but ici est de l'utiliser comme stockage d'énergie pour le réseau électrique. L'hydrogène convient comme vecteur énergétique parce qu'il peut être produit à partir des surplus d'électricité, elle-même produite à partir d'énergies renouvelables, lorsque la production dépasse les besoins immédiats du réseau. Il peut être stocké dans le sous-sol puis extrait pendant les périodes de pénurie.

Cela permet de pallier aux déséquilibres entre la demande et l'approvisionnement en électricité, dus aux fluctuations des énergies renouvelables.

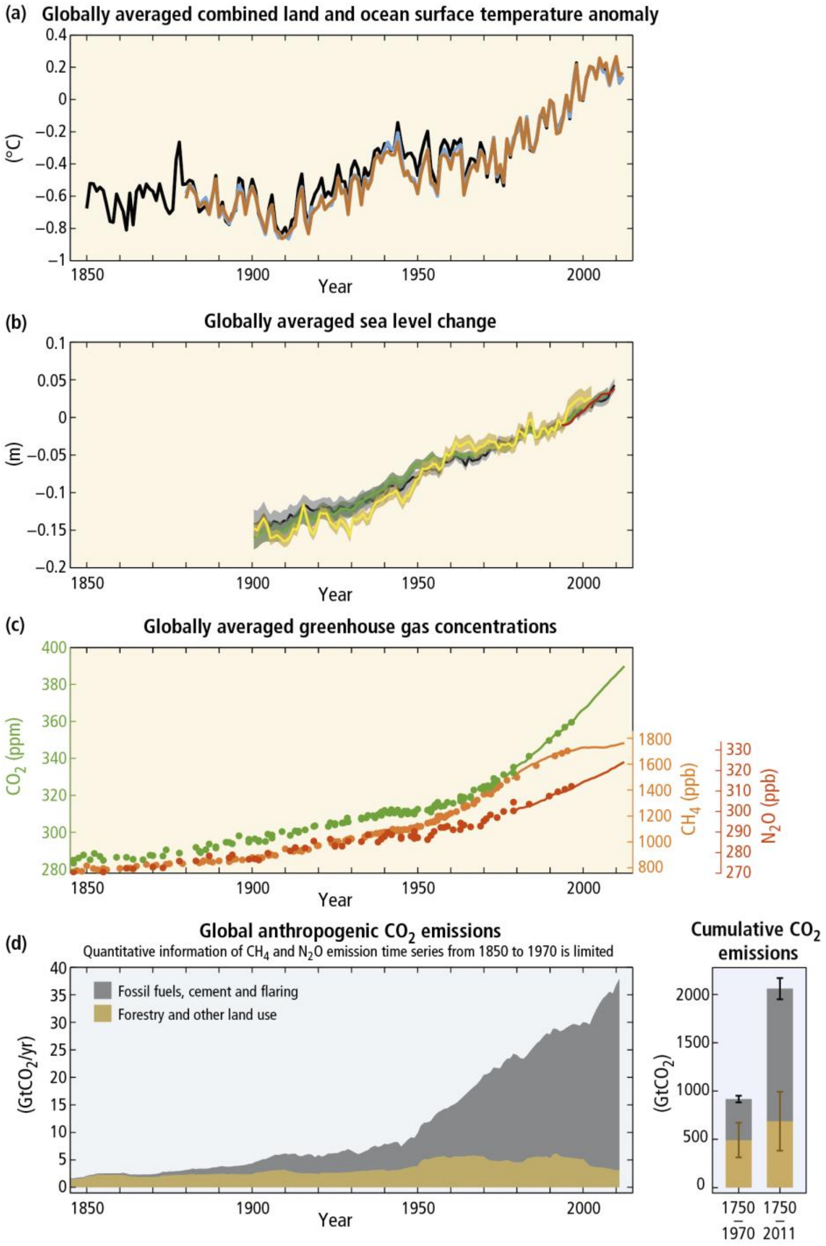

Figure 1-1 Réimpression de la Figure SPM.1 du 5e rapport de synthèse du IPCC (Pachauri et al., 2014) on examine le rapport complexe entre les observations (panneaux a, b et c sur fond jaune) et les émissions panneau d sur fond bleu clair). Observations et autres indicateurs d'un système climatique planétaire en évolution. Observations: a) Moyenne annuelle et mondiale des anomalies de la température de surface combinant les terres émergées et les océans par rapport à la moyenne établie pour la période 1986–2005. Les différents ensembles de données sont représentés par des courbes de couleurs différentes. b) Moyenne annuelle et mondiale de l'évolution du niveau des mers par rapport à la moyenne établie pour la période 1986–2005 pour l'ensemble de données le plus long. Les différents ensembles de données sont représentés par des courbes de couleurs différentes. Tous les ensembles de données sont alignés par rapport à 1993, à savoir la première année de données d'altimétrie par satellite (courbe rouge). Lorsqu'elles sont estimées, les incertitudes sont représentées par des parties ombrées. c) Concentrations atmosphériques des gaz à effet de serre que sont le dioxyde de carbone (CO_2, vert), le méthane (CH_4, orange) et l'oxyde nitreux (N_2O, rouge) déterminées à partir de l'analyse de carottes de glace (points) et obtenues par mesure directe dans l'atmosphère (courbes). Indicateurs: d) Émissions anthropiques mondiales de CO_2 provenant de la foresterie et d'autres utilisations des terres ainsi que de l'utilisation des combustibles fossiles, de la production de ciment et de la combustion en torchère. Les cumuls des émissions de CO_2 provenant des deux types de sources en question et les incertitudes qui y correspondent sont représentés par les boîtes à moustaches verticales sur la droite. Les effets globaux des cumuls des émissions de CH_4 et de N_2O sont représentés sur le panneau c.

Malgré les différences de finalités du stockage et les différences d'échelles de temps qu'elles supposent, ces deux types de stockage ont des aspects communs. Par exemple, l'injection souterraine de fluides, chacun avec des propriétés physiques et chimiques différentes de celles des fluides natifs, entraîne la création d'une interface entre les phases, présentant alors une pression capillaire. Certains facteurs, tels que la saturation ou la perméabilité effective des phases, doivent être pris en compte dans les conditions de flux multiphasique. De plus, les fluides injectés dans les opérations de CCS ou d'UHS sont moins denses et moins visqueux que les fluides natifs, ce qui entraîne leur migration ascendante. Il faut donc une couverture hermétique imperméable pour assurer le confinement du fluide au sein de la formation géologique. Il faut aussi que les structures souterraines de stockage présentent d'autres caractéristiques, comme une perméabilité élevée, une porosité suffisante et une grande capacité en volume, l'une des principales raisons pour considérer le stockage en sous-sol. Ces ressemblances permettent un transfert de connaissances du domaine très étudié du captage et du stockage du dioxyde de carbone à celui du stockage souterrain de l'hydrogène, nettement plus récent.

La dynamique des gaz après injection dans le sous-sol et son impact sur l'aquifère hôte sont très difficiles à surveiller car les formations aptes au stockage sont souvent à de grandes profondeurs (> 500 m), ce qui rend difficile l'analyse des fluides et des roches au cours du temps. Bien qu'elle soit très chère à mettre en œuvre, on peut avoir recours à la géophysique time-lapse, faisant appel, entre autres, à des méthodes de tomographie électrique, magnéto-telluriques et sismiques. Les limitations des méthodes d'acquisition de données sont telles qu'il est très utile de disposer de modèles numériques prédictifs pour évaluer les processus qui ont lieu dans le sous-sol. Le présent travail étudie ce qu'il advient des gaz injectés dans un milieu poreux, à l'aide de modèles numériques de transport réactif et multiphasiques.

L'élaboration de cette thèse suppose l'amélioration de plusieurs programmes de calcul. Un nouveau module pour le transport des solutés et autres formulations des flux multiphasiques ont été implémentées à COMSOL (Comsol, 2016). Le nouveau module pour le transport des solutés dans les eaux souterraines a été élaboré pour répondre aux nécessités du code de transport réactif iCP (Nardi et al., 2014a). iCP intègre COMSOL et PHREEQC (Parkhurst and Appelo, 2013), capables de simuler des processus thermo-hydro-mécaniques et chimiques (THMC) complexes. Ces outils ont permis de mieux comprendre la migration et les interactions des fluides dans des milieux poreux de stockage souterrain, de fournir des recommandations pour améliorer l'efficacité, la surveillance et la sécurité du stockage.

La thèse a été divisée en cinq chapitres. Le chapitre 2 décrit les outils numériques implémentés au cours de cette thèse. Les approches mathématiques et numériques appliquées sont expliquées avec quelques exemples de vérification. Le chapitre 3 traite de la dynamique du CO_2 dans le sous-sol, dans le contexte des projets CCS. Il comporte deux sections : la première, analyse les interactions entre courants gravitaires de CO2, la capillarité, la dissolution et le mélange convectif, à l'aide du modèle multiphasique de fluides miscibles, et la seconde évalue l'effet des réactions sur les digitations dans les mélanges convectifs et la dissolution du CO2, à l'aide de modèles de transport réactifs complètement couplés. Le Chapitre 4 traite plus spécifiquement du stockage de l'hydrogène produit à partir du surplus électrique en Castille-et-León, dans le nord de l'Espagne. Dans ce chapitre est estimée la quantité d'H2 qui peut être récupérée d'un aquifère en utilisant un modèle diphasique de fluides non miscibles. Les résultats les plus importants de cette étude ainsi que les conclusions générales et les perspectives sont présentées dans le chapitre 5.

En plus des modèles numériques de stockage souterrain de gaz présentés aux chapitres 3 et 4, d'autres activités ont été menées au cours de cette thèse, afin de mieux comprendre les défis posés par les solutions envisagées et les risques de leur application à l'atténuation du changement climatique. Des efforts particuliers ont été faits sur l'analyse des flux naturels de CO2 arrivant à la surface. Ces systèmes donnent une idée de la migration du CO2 à proximité de la surface et de l'atmosphère et sur ses effets sur les écosystèmes. Trois études basées sur l'échantillonnage sur le terrain visant à évaluer les techniques de surveillance pour la détection précoce des fuites de CO2 et des méthodologies d'évaluation des risques sont présentées à l'annexe I.

2 Numerical tools

In this section the numerical tools to deal with multiphase flow and solute transport in porous media implemented during the thesis are explained. The thesis focusses on the processes occurring at the aquifer scale (from 1x10^{-3} to 10 m). A continuum approach, where the microscale properties are averaged over a representative elementary volume (REV) is followed. The numerical tools are implemented in COMSOL (Comsol, 2016).

The main characteristics of the multiphase flow are described first, followed by the explanation of the groundwater solute transport. Both sections present the same structure: the mathematical models are presented first with a description of the main approaches reported in the literature; then, the numerical methods applied in their implementation are explained; and finally, some verification examples of the formulations are presented.

2.1 Multiphase flow

Multiphase flow occurs when two or more distinct fluids coexisting are separated by a sharp interface. Each fluid is considered, then, as a phase with its own physical and chemical properties. Taking into account the contact angle between the phases in the presence of a solid phase (θ), the phases can be divided into wetting ($\theta < 90^\circ$) and non-wetting ($\theta > 90^\circ$). Due to the surface tension, there is a pressure change between phases defined with the capillary pressure (P_c):

$$P_c = P_{non-wetting} - P_{wetting} \tag{2-1}$$

In the case where two fluids are miscible and no interface occurs between them, they are considered as part of the same phase and are called components. One phase can contain one or more components (e.g. a gas phase composed by CO_2 and CH_4) and each component can be present in one or more phases (i.e. CO_2 can be present in a system as a gas or dissolved in liquid).

2.1.1 Mathematical description

The number of phases and components to be described in the governing equations depends on the system. This thesis is focused on applications where the natural systems are composed by two phases and two components. Three-phase flow models are applied mainly for water, oil and gas systems in the hydrocarbon industry. A complete description of the three-phase flow can be found at Chen et al. (2006) and Peaceman (1977) among others.

The mathematical description of two-phase systems can be found in the literature (Bastian, 1999; Bear, 1972; Chen et al., 2006; Garcia, 2003; Hassanizadeh and Gray, 1979; Helmig, 1997); and it is comprehensively described in articles related to multiphase flow simulation codes: MUFTE (Assteerawatt et al., 2005), DUMU^x (Flemisch et al., 2011), OpenGeoSys (Goerke et al., 2011; O. Kolditz et al., 2012b), PFLOTRAN (Lu and Lichtner, 2005), TOUGH2 (Pruess et al., 1999; Pruess and Spycher, 2007), CodeBright (Vilarrasa, 2012), HYTEC (Sin et al., 2017), ECLIPSE (ECLIPSE, 2004), ELSA (Nordbotten et al., 2009, 2004b), FEHM (Pawar et al., 2005), GPRS (Cao, 2002; Jiang, 2008), IPARS (Wheeler and Wheeler, 2001), COORES (Le Gallo et al., 2006; Trenty et al., 2006), MoReS (Farajzadeh et al., 2012; Wei, 2012) and RTAFF (Sbai, 2007).

The mathematical model can vary widely in each application depending on the specific questions to be answered, the relevant processes, and the time scale and length associated to those processes. This thesis does not consider the geomechanical effects and the heat conservation in the multiphase flow. Simplifications of the multiphase flow such as vertical equilibrium models (Nordbotten and Celia, 2006) or macroscopic percolation models (Cavanagh and Haszeldine, 2014) are found to greatly reduce the computational complexity of the system. These simplified models are out of the scope of this thesis. A review of these methods can be found in Bandilla et al. (2015), Celia et al. (2015) and Celia and Nordbotten (2009).

This section starts with the description of the more general compositional model, where mass transfer between phases is taken into account. The component mass conservation system of equations and the constitutive and state relations needed to solve the system are explained. Then, some immiscible formulations are presented. In systems where the component behavior is not relevant, the multiphase flow can be represented by immiscible formulations with a much lower computational cost.

2.1.1.1 Compositional model

The mass conservation of each component (κ) in a system with α phases can be written as:

$$\sum_\alpha \partial_t(\phi S_\alpha \rho_\alpha m_\alpha^\kappa M^\kappa) = \sum_\alpha -\nabla \cdot \left(\boldsymbol{q_\alpha} \rho_\alpha m_\alpha^\kappa M^\kappa - \phi S_\alpha \rho_\alpha \boldsymbol{D_\alpha} \cdot \nabla(m_\alpha^\kappa M^\kappa)\right) + T_\alpha^\kappa + Q_\alpha^\kappa \tag{2-2}$$

where α denotes the fluid phase, ϕ is the porosity of the medium ($m^3 \cdot m^{-3}$), S_α is the phase saturation ($m^3 \cdot m^{-3}$), ρ_α is the phase density ($kg \cdot m^{-3}$), m_α^κ is the molality of the κ component in the α phase ($mol \cdot kg^{-1}$), M^κ is the component molar weight ($kg \cdot mol^{-1}$), $\boldsymbol{q_\alpha}$ corresponds to the phase Darcy's flow in its multiphase form ($m^3 \cdot m^{-2} \cdot s^{-1}$), $\boldsymbol{D_\alpha}$ is the phase diffusion/dispersion tensor ($m^2 \cdot s^{-1}$), Q_α^κ is the component mass source term in the α phase ($kg \cdot m^{-3} \cdot s^{-1}$) and T_α^κ is the component interphase mass transfer term ($kg \cdot m^{-3} \cdot s^{-1}$).

The last four terms can be extended as:

$$\boldsymbol{q_\alpha} = -\frac{k k_\alpha^r}{\mu_\alpha}(\nabla P_\alpha - \rho_\alpha \boldsymbol{g}) \tag{2-3}$$

$$\boldsymbol{D}_\alpha = D_m \boldsymbol{I} + |\boldsymbol{q_\alpha}|\left(\alpha_L \boldsymbol{E}(\boldsymbol{q_\alpha}) + \alpha_T \boldsymbol{E}^\perp(\boldsymbol{q_\alpha})\right) \tag{2-4}$$

$$Q_\alpha^\kappa = Q_\alpha M^\kappa m_\alpha^\kappa \tag{2-5}$$

$$T_\alpha^\kappa = \phi S_\alpha \rho_\alpha k_{kin}^\kappa (\overline{m}_\alpha^\kappa - m_\alpha^\kappa) M^\kappa \tag{2-6}$$

where k is the permeability tensor (m^2), k_α^r is the relative phase permeability ($-$), μ_α is the phase dynamic viscosity ($Pa \cdot s^{-1}$), P_α is the pressure (Pa) and $\boldsymbol{g}$ is the gravity vector ($m \cdot s^{-2}$), D_m is the species-independent molecular diffusion coefficient ($m^2 \cdot s^{-1}$), $\alpha_L$and α_T are, respectively, the longitudinal and transverse dispersivity (m), $|\boldsymbol{q_\alpha}|$ is the Euclidean norm of Darcy's flow, $\boldsymbol{E}(\boldsymbol{q_\alpha})$ is the orthogonal projection along velocity and $\boldsymbol{E}^\perp = \boldsymbol{I} - \boldsymbol{E}(\boldsymbol{q_\alpha})$, Q_α is the phase mass source term ($kg \cdot m^{-3} \cdot s^{-1}$), k_{kin}^κ (s^{-1}) is the interphase mass transfer of component κ and $\overline{m}_\alpha^\kappa$ ($mol \cdot kg^{-1}$) is the solubility limit of component κ in the α phase.

The system of equations in (2-2) has $2N_\alpha + N_\alpha N_\kappa$ dependent variables: $2N_\alpha$ from the phase pressures and saturations and $N_\alpha N_\kappa$ components molalities. The system is constrained by the phase saturation equation, the N_α phase mass fraction and $(N_\alpha - 1)N_\kappa$ phase equilibrium relations:

$$\sum_\alpha S_\alpha = 1 \qquad (2\text{-}7)$$

$$\sum_k M^k m_\alpha^k = 1 \qquad (2\text{-}8)$$

$$\sum_\alpha T_\alpha^k = 0 \qquad (2\text{-}9)$$

$$\sum_k Q_\alpha^k = Q_\alpha \qquad (2\text{-}10)$$

Constitutive relations

To close the system $(N_\alpha - 1)$ capillary pressure relations needs to be taken into account. Generally, the capillary pressure is described as function of the saturation of the higher wettability (Niessner and Helmig, 2007). The most common approaches of the capillary pressure are Brooks and Corey (1964) and van Genuchten (1980). Recently, a more complex model where capillary pressure is function of the specific interfacial area apart from the saturation has been developed (Niessner and Hassanizadeh, 2008); however, it has been rarely implemented in multiphase flow models (Tatomir et al., 2015). In the multiphase flow equations implemented in this thesis the user can define whether Brooks and Corey or Van Genuchten capillary approach is used.

Additional equations relate the phase density and viscosity with its pressure, temperature and composition. The influence of pressure and temperature in the liquid density and viscosity is limited, while gas phases present much more variability. Usually, experimental relationships are used to determine the density and viscosity of the components. In this thesis, apart from the relations already implemented in COMSOL (Comsol, 2016), the properties of the CO_2-brine system implemented by Pruess and Spycher (2007) in TOUGH2 are incorporated. The gas density can also be determined following the ideal gas law and the Peng-Robinson equation of state (Robinson and Peng, 1978). Other relationship could be easily added by the user to the system.

The partitioning of components between the phases is usually considered in equilibrium, which is a reasonable assumption when the time scale of mass transfer is large compared to the time scale of flow. Compositional multiphase formulations based on local equilibrium are extensively described in the literature (Firoozabadi, 1999; Lu and Lichtner, 2005; Michelsen et al., 2008; Pruess et al., 1999). In gas-liquid systems the Henry's law and the saturation vapor pressure are used to define the mole fraction in each phase.

If component partitioning is not described by equilibrium, a kinetic expression is used for the interphase mass transfer (equation 2-6). Several approaches are described in the literature. Van Antwerp et al. (2008) extended the dual domain approach for kinetic mass transfer during air sparing from the laboratory scale (Falta, 2003, 2000) to field scale. Niessner and Hassanizadeh (2009) developed a method where the interphase mass transfer was function of the mass balance of the specific interfacial area. Other authors use a lumped mass transfer rate calculated through the non-dimensional modified Sherwood number (Sh) to solve the equation (Agaoglu et al., 2015; Imhoff et al., 1994; Miller et al., 1990; Powers et al., 1994, 1992; Zhang and Schwartz, 2000):

$$k_{kin}^{k} = Sh\frac{D_m}{d_{50}^2} \tag{2-11}$$

$$Sh = \alpha Re^{\beta} S_{\beta}^{\gamma} \tag{2-12}$$

where k_{kin}^{k} is the kinetic mass transfer rate (s^{-1}), d_{50} is the mean size of the reservoir grains (m), Re is the Reynold's number (-), S_β is the saturation of the β phase and α, β, γ are dimensionless fitting parameters. This approach is followed in the compositional multiphase formulation implemented in this thesis.

Choice of primary variables and system of equations

Different linear combinations of equations and state variables can be used to diminish the stiffness of the compositional multiphase flow system (Binning and Celia, 1999; Chavent, 1981; Chen et al., 2000; Chen and Ewing, 1997a; Coats, 1980). The most classic approach is to sum over components and choose the so-called natural variables (pressure and saturation of the phases and molality of components) as dependent variables and apply a local variable switching depending on the phases present in each cell (Class et al., 2002; Coats, 1980; Lu and Lichtner, 2005; Pruess et al., 1999).

Phase disappearance is one of the major problems in multiphase flow simulation. It leads to the degeneration of the equation satisfied by the saturation, making natural variables inappropriate. Variable switching is able to cope with this process varying the dependent variables depending on the phases present in each cell. Nevertheless, this approach has some drawbacks as generates perturbations on the Newton iteration when phase changes occur and affect the structure of the Jacobian matrix (Lu et al., 2010).

Several alternative approaches are proposed in the literature where the dependent variables remain constant throughout the domain. Jaffré and Sboui (2010) use complementarity conditions. Abadpour and Panfilov (2009) allow the extension of saturation to negative values. Moreover, various combinations of dependent variables are described for two phase flow: liquid phase pressure and water mass concentration (Bourgeat et al., 2013); gas pressure and liquid pressure (Angelini et al., 2011); pressure, saturation and fugacities (Lauser et al., 2011); capillary pressure and gas pressure (Neumann et al., 2013);… Comparison between some of these methods can be found in literature (Gharbia et al., 2015; Lu et al., 2010; Masson et al., 2014; Neumann et al., 2013; Voskov and Tchelepi, 2012).

In this thesis, the compositional multiphase flow is implemented and applied to carbon capture and storage (section 3.2) using the natural variables as dependent variables. Water miscibility in the CO_2 rich phase is low, on the order of one per cent (Spycher and Pruess, 2005). Therefore, water dissolution in supercritical CO_2 is neglected, reducing the system of equations (2-2) to three. Thus, only one interphase mass transfer ($T_l^{CO_2}$) has to be defined through the Sherwood number approach. No variable switching is applied and it is considered that the liquid phase remains throughout the system, even in small amounts. A new linear combination of the system of equations (2-2) is used to describe the three equations of the system:

$$\partial_t\left(\phi S_l\rho_l + \phi S_g\rho_g\right) = -\nabla\cdot\left(\boldsymbol{q_l}\rho_l + \boldsymbol{q_g}\rho_g\right) + Q_g + Q_l \tag{2-13}$$

$$\begin{aligned}&\partial_t\left(\phi S_l\rho_l m_l^{CO_2}M^{CO_2} + \phi S_g\rho_g\right) =\\ &\qquad -\nabla\cdot\left(\boldsymbol{q_l}\rho_l m_l^{CO_2}M^{CO_2} + \boldsymbol{q_g}\rho_g - \phi S_l\rho_l\boldsymbol{D_l}\cdot\nabla\left(m_l^{CO_2}M^{CO_2}\right)\right) + Q_l^{CO_2} + Q_g\end{aligned} \tag{2-14}$$

$$\begin{aligned}&\phi S_l\rho_l\partial_t\left(m_l^{CO_2}M^{CO_2}\right) - m_l^{CO_2}M^{CO_2}\partial_t\left(\phi S_g\rho_g\right) =\\ &\qquad -\boldsymbol{q_l}\rho_l\cdot\nabla\left(m_l^{CO_2}M^{CO_2}\right) + m_l^{CO_2}M^{CO_2}\nabla\cdot\left(\boldsymbol{q_g}\rho_g\right) + \nabla\cdot\left(\phi S_l\rho_l\boldsymbol{D_l}\cdot\left(m_l^{CO_2}M^{CO_2}\right)\right)\\ &\qquad -Q_l\left(m_l^{CO_2} - m_l^{CO_2,*}\right)M^{CO_2} - Q_g m_l^{CO_2}M^{CO_2} + T_l^{CO_2}\end{aligned} \tag{2-15}$$

where $m_l^{CO_2,*}$ is the external CO_2 concentration. These equations are derived from:

1. the total mass conservation equation (2-13) obtained by summing over all equations of system of equations (2-2);
2. an equation for the CO_2 mass conservation (2-14) obtained by adding the equations for the CO_2 component ($\kappa = CO_2$) in both phases ($\alpha = l, g$);

3. equation (2-15), derived by subtracting equation (2-13) multiplied by $m_l^{CO_2} M^{CO_2}$ from the aqueous CO$_2$ mass conservation (equation (2-2) for $\alpha = l$ and $\kappa = CO_2$).

The dependent variables solved are liquid pressure (P_l) in equation (2-13), gas saturation (S_g) in equation (2-14) and dissolved CO$_2$ molality ($m_l^{CO_2}$) in equation (2-15).

The approaches followed to model the fluids density and viscosity, the relative permeability and capillary pressure are used-defined.

2.1.1.2 Immiscible formulations

In cases where no mass transfer between phases or when the behavior of the components is not relevant for the purpose of the model; the mass balance equations can be written for the bulk phase rather than for individual components. The phase mass conservation is achieved by summing equation (2-2) over components and assuming no internal component gradient (no diffusion-dispersion within the phases):

$$\partial_t(\phi \rho_\alpha S_\alpha) = -\nabla \cdot (\rho_\alpha \boldsymbol{q_\alpha}) + Q^\alpha \tag{2-16}$$

where Q^α is the phase mass source term ($kg \cdot m^{-3} \cdot s^{-1}$). The Darcy's flow is described in equation (2-3). The system of equations (2-16) has $2N_\alpha$ unknowns that can be solved taking into account the saturation constrain (equation2-7) and the $(N_\alpha - 1)$ capillary pressure relations (equation 2-1).

As for the compositional formulation, various dependent variables and linear combinations of equations can be selected (Aziz and Settari, 1979; Binning and Celia, 1999; Chavent, 1981; Chen et al., 2000; Hassanizadeh and Gray, 1979). Some of the formulations described in the literature and implemented during the thesis are summarized below for the two-phase flow systems.

Coupled Pressure-Saturation formulation

In this formulation, the general system of two equations (2-16) is solved without any linear combination. One equation takes the phase pressure as the dependent variable, while the other solves the phase saturation. Integrating the Darcy's velocity and taking wetting saturation (S_w) and non-wetting phase pressure (P_n) as unknowns the system is written as:

$$\partial_t(\phi\rho_w S_w) = \nabla\cdot\left(\rho_w k\lambda_w(\nabla P_n + \frac{dP_{cap}}{dS_w}\nabla S_w - \rho_w g\nabla z\right) + Q^w \tag{2-17}$$

$$-\partial_t(\phi\rho_n S_w) = \nabla\cdot(\rho_n k\lambda_n(\nabla P_n - \rho_n g\nabla z)) + Q^n \tag{2-18}$$

where subscript w and n denote the wetting phase and non-wetting phase respectively and λ is the phase mobility ($\lambda_\alpha = k_\alpha^r/\mu_\alpha$).

Similarly, the wetting pressure/non-wetting saturation ($P_w - S_n$) can be developed. This system of equations is strongly coupled and non-linear.

Decoupled Pressure-Saturation formulations

Dividing the equations in (2-16) by the density, the mass conservation equation is transformed into a volumetric equation. Summing, then, these equations over the two phases, the temporal derivative over saturation is removed, diminishing the coupling of the system:

$$\sum_\alpha\left(\frac{S_\alpha}{\rho_\alpha}\partial_t(\phi\rho_\alpha)\right) = -\sum_\alpha\left(\frac{1}{\rho_\alpha}\big(\nabla\cdot(\rho_\alpha\boldsymbol{q_\alpha})\big)\right) + \sum_\alpha\frac{Q^\alpha}{\rho_\alpha} \tag{2-19}$$

Equation (2-19) is called the pressure equation and it can be solved using different pressures as dependent variable (Chen et al., 2006; Hoteit and Firoozabadi, 2008; O. Kolditz et al., 2012b). If S_α is explicitly evaluated, the pressure can be first computed and, then, the saturation can be solved with one of the equations of system in (2-16). This is the implicit pressure-explicit saturation (IMPES) scheme that has been extensively used in two-phase flow simulations and was first introduced by Sheldon and Cardwell (1959) and Stone and Garder (1961).

This formulation with the wetting pressure/non-wetting saturation ($P_w - S_n$) as dependent variables is applied for the model in section 4. The multiphase flow for these unknowns has the following form:

$$\frac{S_n}{\rho_n}\partial_t(\phi\rho_n) + \frac{(1-S_n)}{\rho_w}\partial_t(\phi\rho_w) = \frac{1}{\rho_n}\nabla\cdot\left(\rho_n k\lambda_n\left(\nabla P_w + \frac{dP_{cap}}{dS_n}\nabla S_n - \rho_n g\nabla z\right)\right)$$

$$+\frac{1}{\rho_w}\nabla\big(\rho_w k\lambda_w(\nabla P_w - \rho_w g\nabla z)\big) + \frac{Q^n}{\rho_n} + \frac{Q^w}{\rho_w} \tag{2-20}$$

$$\partial_t(\phi\rho_n S_n) = \nabla\cdot\left(\rho_n k\lambda_n(\nabla P_w + \frac{dP_{cap}}{dS_n}\nabla S_n - \rho_n g\nabla z\right) + Q^n \tag{2-21}$$

Similar systems of equations can be developed for the $P_n - S_w$ unknowns or using the wetting phase equation instead of (2-21).

Global pressure formulation

The global pressure (P_{tot}) concept was first introduced by Antontsev (1972) and Chavent and Jaffré (1986) and it has been frequently used in the modelling of multiphase flow since (Bastian, 1999; Chen and Ewing, 1997b; Sin, 2015). Global pressure is defined as:

$$\nabla P_{tot} = \textstyle\sum_\alpha (f_\alpha \nabla P_\alpha) \tag{2-22}$$

where $f_\alpha$is the fractional flow ($f_\alpha = \lambda_\alpha / \lambda_{tot}$) and λ_{tot} is the summation of the phase mobilities ($\lambda_{tot} = \sum_\alpha \lambda_\alpha$).

A total velocity can also be defined as:

$$\boldsymbol{q_{tot}} = \textstyle\sum_\alpha \boldsymbol{q_\alpha} = -\, k\lambda_{tot}(\nabla P_{tot} - \sum_\alpha (f_\alpha \rho_\alpha g \nabla z)) \tag{2-23}$$

Instead of using one of the phase pressures as dependent variable as in the formulations presented before, this formulation solves the equation (2-19) using the global pressure as unknown. The system of equations is completed with the wetting phase equation (2-17) solved with for the wetting saturation written in terms of total velocity:

$$\textstyle\sum_\alpha \left(\frac{S_\alpha}{\rho_\alpha} \partial_t(\phi \rho_\alpha) \right) = -\nabla \cdot \boldsymbol{q_{tot}} + \sum_\alpha \frac{Q^\alpha}{\rho_\alpha} \tag{2-24}$$

$$\partial_t(\phi \rho_w S_w) = -\nabla \cdot \left(\rho_w \left(f_w \boldsymbol{q_{tot}} + f_w \lambda_n k \left(\tfrac{dP_{cap}}{dS_w} \nabla S_w + (\rho_w - \rho_n) g \nabla z \right) \right) \right) + Q^w \tag{2-25}$$

The global pressure and total mobility are always continuous, even in the absence of one phase, favoring the convergence of the models. Furthermore, the total velocity is smoother than the phase velocities. However, the global pressure variable is not an actual physical property and initial and boundary conditions do not have a direct physical meaning with this formulation.

Capillary pressure formulation

The formulation that uses capillary pressure and the non-wetting pressure as dependent variables is also relevant in the literature (O. Kolditz et al., 2012b; Neumann et al., 2013). The system of equations is formed by the wetting phase equation (2-17) and the non-wetting phase equation (2-18) solved with the non-wetting pressure (P_n) and the capillary pressure (P_{cap}) as unknowns respectively:

$$\phi\rho_w \frac{dS_w}{dP_{cap}} \partial_t\left(P_{cap}\right) + S_w \partial_t(\phi\rho_w) = \nabla \cdot \left(\rho_w k\lambda_w(\nabla P_n - \nabla P_{cap} - \rho_w g\nabla z\right) + Q^w \quad \text{(2-26)}$$

$$-\phi\rho_n \frac{dS_w}{dP_{cap}} \partial_t\left(P_{cap}\right) + (1 - S_w)\partial_t(\phi\rho_n) = \nabla \cdot (\rho_n k\lambda_n(\nabla P_n - \rho_n g\nabla z) + Q^n \quad \text{(2-27)}$$

Similar to the global pressure formulation, the use of the capillary pressure as dependent variable has the advantage that is continuous independently of the number of phases present in the cell. As a counterbalance, it is difficult to assign meaningful initial and boundary conditions with this formulation.

2.1.2 Numerical methods

The multiphase flow mathematical models are implemented in COMSOL Multiphysics (Comsol, 2016), a general-purpose finite element (FE) platform for the modelling and simulation of all kind of partial differential equations (PDE), ordinary differential equations (ODE) and algebraic differential equations (DAE) systems. It allows a flexible configuration of the shape functions, system properties, constitutive relations, solution schemes and solvers of the equations systems. COMSOL has a very intuitive and robust graphical user interface (GUI) with many options for geometry delineation, mesh generation and post-processing and visualization of the results. The multiphase flow PDE systems with their associated DAEs can be further combined with a set of physical interfaces for common physics applications areas available in COMSOL, accounting for coupled and multiphysics phenomena.

The main numerical characteristics (spatial discretization, solution scheme and linear equations system solvers) of the implemented multiphase flow equations are described in this section.

2.1.2.1 Spatial discretization

Many numerical methods have been developed for solving the convection-diffusion like equations through finite element methods (Chen et al., 2006; Helmig, 1997). A standard-Galerkin or Bubnov-Galerkin method based on linear continuous Lagrange shape or space functions is implemented in this thesis. The Galerkin method is based on the mean weighted residuals method where shape functions are equal to the weighting (also known as test) functions.

Alternative methods use two different finite element spaces, one for dependent scalar variables (e.g., pressure) and other for vector variables (e.g., fluid velocity). These methods are called mixed finite element (MFE) and should satisfy the Babuska–Brezzi (Brezzi et al., 1985) condition, which states that the shape functions for pressure must be of lower order than the shape functions for velocity. They were first introduced by (Nedelec, 1980; Raviart and Thomas, 1977) and many MFE were further developed in the literature. Two of the more common methods are the streamline upwind/Petrov-Galerkin (SUPG) method (Brooks and Hughes, 1982; Westerink and Shea, 1989; Zienkiewicz et al., 2005) and the Galerkin least-squares (GLS) method (Codina, 1998). The advantage of these methods is that they approximate both the scalar and vector variables simultaneously, giving a high order approximation. However, their implementation is more complex and rarely used (Hinkelmann, 2005). The discretization of PDEs with discontinuous shape functions across inter-element boundaries, i.e. discontinuous Galerkin (DG) method (Reed and Hill, 1973), are also an option for solving advective dominated problems from which continuous FEM lack robustness.

Sharp saturation fronts of the convection-diffusion equation can become unstable in Galerkin finite element methods (Carrayrou et al., 2003; De Windt et al., 2003; Helmig, 1997). The instabilities can be overcome with the help of stabilization methods. There are various stabilization techniques. Streamline diffusion and crosswind diffusion (based on the SUPG and GLS methods) are among the most common (Hauke, 2001; Hauke and Hughes, 1994; Hughes and Mallet, 1986). In the miscible model presented in this thesis, an isotropic diffusion stabilization method is used. The streamline diffusion and crosswind diffusion stabilizations are also implemented.

2.1.2.2 Solution scheme

The nonlinear equations system of the multiphase flow is solved through the Newton iterative method. Newton’s iterations in time can be solved with explicit and implicit methods.

Implicit schemes are unconditionally stable but computationally expensive as a nonlinear system of equations must be solved in each time step. Explicit schemes demand less computational resources; however, they come with stability time-stepping restrictions. In nonlinear systems as the multiphase flow equations, the time steps required may be too small to solve a problem explicitly within a reasonable computational time. The implicit schemes allow larger times but they can have severe damping effects (i.e., numerical dispersion) (Allen, 1984; Settari and Aziz, 1975).

An intermediate scheme, the implicit pressure-explicit saturation (IMPES), has been used in the literature to achieve better stability without having as much computational cost (Sheldon and Cardwell, 1959; Stone and Garder, 1961). They have been used widely for the solution of incompressible decoupled Pressure-Saturation formulations. However, this scheme is not efficient with systems with strong nonlinearities.

The solution of all the coupled nonlinear equations simultaneously and implicitly is known as the fully implicit method (FIM) or the simultaneous solution (Douglas et al., 1959). Variables are updated every Newton iteration, leading to a stable scheme that allows relatively large time steps. However, in systems with many chemical components, the Jacobian matrix may be large, requiring high computational resources.

Other relevant implicit methods are sequential (SM) (MacDonald and Coats, 1970), where the saturation dependent functions (e.g., relative permeability) have the values of the previous Newton iteration. These schemes are more stable than IMPES and more computationally efficient than FIM. When using these methods, it should be taken into account that the accuracy on the evaluation of the saturation dependent functions influences the accuracy and stability of the numerical methods (Aziz and Settari, 1979; Peaceman, 1977; Settari and Aziz, 1975).

Finally, an alternative solution scheme is the adaptive implicit method (AIM), which seeks an efficient middle point between the FIM and the IMPES scheme (Russell, 1989; Thomas and Thurnau, 1983). This time-stepping algorithm switches between the implicit and explicit depending on the problem and gradients of each grid block. Various comparative studies of these solution schemes are available in the literature (Bastian, 1999; Chen et al., 2006; Marcondes et al., 2009).

The solution scheme for the implemented multiphase flow equations is user-defined. The user can apply the solution schemes provided by COMSOL (all the previously explained except the IMPES). The models presented in this thesis are solved with the backward differentiation formulas (BDF) fully implicit scheme. The generalized-α method has been also successfully applied in FIM and implicit sequential schemes in applications not shown in this thesis.

The Explicit solution schemes integrated in COMSOL are the classical Runge-Kutta methods of order 1–4 and the third-order Adams-Bashforth multistep method. Two options are supported for implicit schemes: backward differentiation formulas (BDF) and generalized-α.

The BDF methods use backward differentiation formulas with order of accuracy varying from one (i.e., backward Euler) to five. They have been widely used due to its stability; however, they can have significant damping effects, especially in lower-orders methods. Generalized-α is similar to the second-order BDF with an α parameter to control de degree of damping (Brenan et al., 1995; Chung and Hulbert, 1993). It generates less damping, leading to more accurate results than second order BDF; however, it is less stable than BDF methods. Both implicit schemes have adaptive time steps algorithms. The settings of the schemes are really flexible: they can be applied with a fully implicit or segregated method; and the user controls how often the Jacobian is updated, the tolerances, the damping factor,…

An adaptive implicit method is also available for the implicit scheme with BDF methods. The IDA is variable-order variable-step-size backward differentiation method developed by Hindmarsh et al. (2005) as an evolution of the DASPK method (Brown et al., 1994).

2.1.2.3 Linear system solvers

Newton method solves a linear system each iteration. Generally, the Jacobian matrix arising from multiphase flow is non-symmetric, sparse and ill-conditioned. The solution of this linear system is, thus, the most time demanding task on multiphase flow simulation. Iterative and direct methods are available in the literature to solve such systems. Iterative solvers required less computational resources and are generally faster than direct solvers. However, they are less robust than direct solvers. The linear system solvers applied is, as for the solution scheme, selected by the user. Many solvers are provided at the COMSOL platform. The detailed description of the methods and preconditioners is out of the scope of this chapter; however, a brief summary is provided below. The models presented in this thesis are all developed with the robust PARDISO direct solver.

There are many iterative solvers proposed in the literature (Barrett et al., 1994; Benzi, 2002; Chen et al., 2006). Saad (2003) and Greenbaum (1997) summarized the most relevant, describing the methods and their preconditioners. Preconditioning is a needed step in these methods. It affects the number of iterations and, eventually, the solver's convergence; and may consume more time and memory than the actual solver. Many preconditioners are supported by COMSOL: SOR, Jacobi, Vanka, SCGS, SOR Line/Gauge/Vector, geometric multigrid (GMG), algebraic multigrid (AMG), Auxiliary Maxwell Space(AMS), Incomplete LU and Krylov. These preconditioners can be used in four iterative methods: conjugate gradients (Greenbaum, 1997; Hestenes and Stiefel, 1952; Lanczos, 1952), BiCGStab (van der Vorst, 1992), GMRES (Saad and Schultz, 1986) and FGMRES (Saad, 1993). As a general rule, the more memory is used by the method, the more computational time requires and the less robust the method is. The methods above are ordered from less to more computational resources.

Direct methods for sparse linear systems are becoming more popular with the increase in computer power and the use of shared memory and parallel algorithms (Davis, 2006). The direct methods provided by COMSOL are also parallelized: MUMPS ("MUMPS Credits," 2017), PARDISO (Cosmin et al., 2014; "PARDISO 5.0.0 Solver Project," 2017) and SPOOLES ("linalg/spooles," 2017). All of them use the LU factorization preconditioning of the matrix.

2.1.3 Verification

The multiphase flow formulations presented in this section are verified through three benchmarks. First the immiscible formulations are compared with semi-analytical solutions in the 1D Buckley-Leverett (Buckley and Leverett, 1942) and McWhorter (McWhorter and Sunada, 1990) problems. Then, the leakage of CO_2 through an abandoned well in a 3D model (Ebigbo et al., 2007) is compared with reference solutions for immiscible and miscible multiphase flow.

2.1.3.1 Buckley-Leverett problem

Buckley and Leverett (1942) developed a semi-analytical solution for the displacement of oil by water in a 1D homogeneous porous media (Figure 2-1). The model considers immiscible, constant fluid density and porosity and no source-sink terms. The effects of the capillarity and gravity are neglected in the derivation of the analytical solution. The problem is frequently used to test the functional relation between relative permeability and saturation in numerical codes (Helmig, 1997; Hoteit and Firoozabadi, 2008; O. Kolditz et al., 2012b).

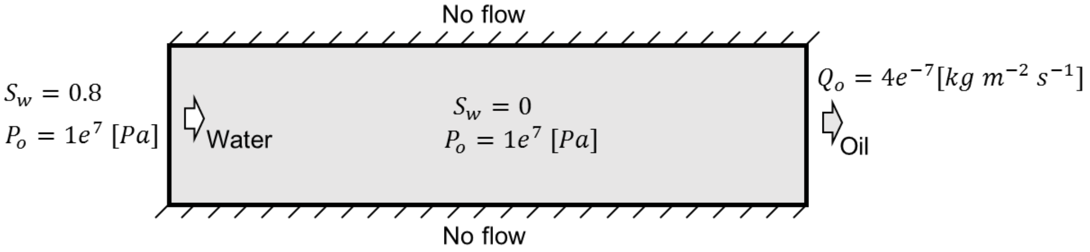

Figure 2-1. Conceptual model of the Buckley-Leverett problem.

A fluid with a water saturation of 0.8 is injected in a 300 m long porous media initially filled with a non-wetting fluid (oil). Oil pressure and water saturation are prescribed in the inflow boundary, while oil outflow is defined in the outlet boundary. The numerical solution is compared with the analytical solution for three fluid viscosity ratios (μ_w/μ_o). The relevant parameters of the model are described in Table 2-1.

$$0 = \nabla \cdot (k\lambda_{tot} \nabla P_o) \tag{2-28}$$

$$\phi\partial_t(S_w) = \nabla \cdot (k\lambda_w \nabla P_n) \tag{2-29}$$

The relation between the relative permeability and the saturation is estimated with the Brooks and Corey equations (Table 2-2). The spatial discretization has 300 elements and an adaptive time step is used.

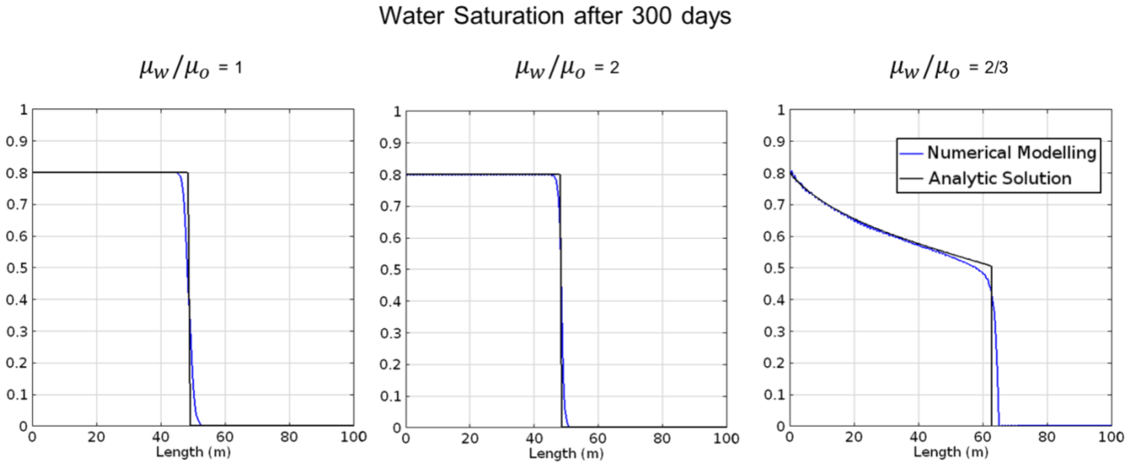

Figure 2-2. Water saturation profile after 300 days of the Buckley-Leverett problem. Viscosity ratios of 1, 2 and 2/3 are shown for the numerical and analytical solutions.

The location of the water saturation front after 300 days is shown for the three viscosity ratios in Figure 2-2. The numerical and analytical solutions are in good agreement for the three cases.

Table 2-1. Buckley-Leverett model parameters.

	Parameter	Symbol	Value	Unit
Aquifer	Porosity	ϕ	0.2	-
	Permeability	k	1x10^{-5}	m^2
Retention curve	Pore index	ω	2	-
	Residual water saturation	S_w^r	0	-
	Residual oil saturation	S_o^r	0.2	-
Fluid properties	Water density	ρ_w	1x10^{3}	$kg\cdot m^{-3}$
	Oil density	ρ_o	1x10^{3}	$kg\cdot m^{-3}$
	Viscosity ratio	μ_w/μ_o	1, 2, 2/3	-
Initial conditions	Oil pressure	P_o	1x10^{7}	Pa
	Water saturation	S_w	0	-
Boundary conditions	Oil pressure x=0	P_o	1x10^{7}	Pa
	Water saturation x=0	S_w	0.8	-
	Oil flux x=300	Q_0	3x10^{-4}	$kg\cdot m^{-2}\cdot \mathrm{s}^{-1}$
	Water saturation x=300	S_w	0	-

Table 2-2. Brooks-Corey equations related to the retention curve.

Name	Expression
Effective saturation	$S_e = \dfrac{S_w - S_w^r}{1 - S_w^r - S_n^r}$
Capillary pressure	$P_c = P_t {S_e}^{-1/\omega}$
Relative liquid permeability	$k_w^r = {S_e}^{\frac{2+3\omega}{\omega}}$
Relative gas permeability	$k_n^r = (1 - S_e)^2 \left(1 - {S_e}^{\frac{2+\omega}{\omega}}\right)$

2.1.3.2 McWhorter problem

McWhorter and Sunada (1990) developed a semi-analytical solution for the displacement of a non-wetting phase (oil) by a wetting phase (water) in a 1D homogeneous porous media (Figure 2-3). The model considers immiscible flow and constant density and porosity but, contrary to Buckley-Leverett problem, the flow is governed by capillarity. The problem has been analyzed extensively in the literature (Bastian, 1999; Chen et al., 1992; O. Kolditz et al., 2012b; McWhorter and Sunada, 1992). Recently, Fučik et al. (2007, 2008) improved the original semi-analytical solution. To aid the comparison with other codes, however, the original solution is used in this thesis (Fučik, 2007).

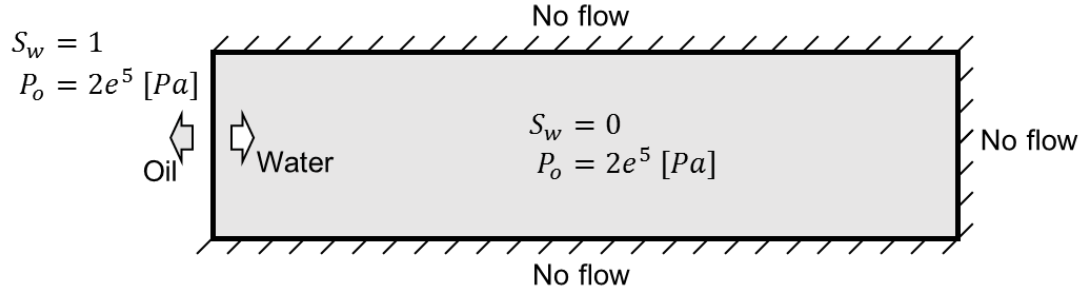

Figure 2-3. Conceptual model of the McWhorter problem.

The 1D domain is 2.6 m long. The gravity force is neglected and no sink-source occur. The water saturation and pressure at the left boundary are fixed, while no flow is allowed at the right boundary. This configuration leads to a counter current of oil where the flow is driven by capillary forces. Table 2-3 presents the relevant parameters of the model.

The McWhorter problem is solved for various of the immiscible formulations presented in this chapter. All the implementations use the Brooks and Corey (1964) capillarity and relative permeability equations (Table 2-2). The grid elements have a length of 0.05 m and an adaptive temporal discretization is used.

As explained before, the definition of initial and Dirichlet conditions are not straightforward for the capillary and global pressure variables. To allow the presence of both phases, the capillary pressure at the boundary is assumed equal to the entry pressure. The wetting phase pressure is estimated considering this P_{cap}. The global pressure at the initial state and at the boundary has the same value than the P_w at the boundary. To help the convergence of the models an initial water saturation of 1x10^{-10} has been considered in all the models. The high initial P_{cap} value results from the Brooks and Corey relation for this low water saturation. The initial and boundary conditions for all the formulations are presented in Table 2-3. Note that the initial value is used only as initial guess for the Newton method.

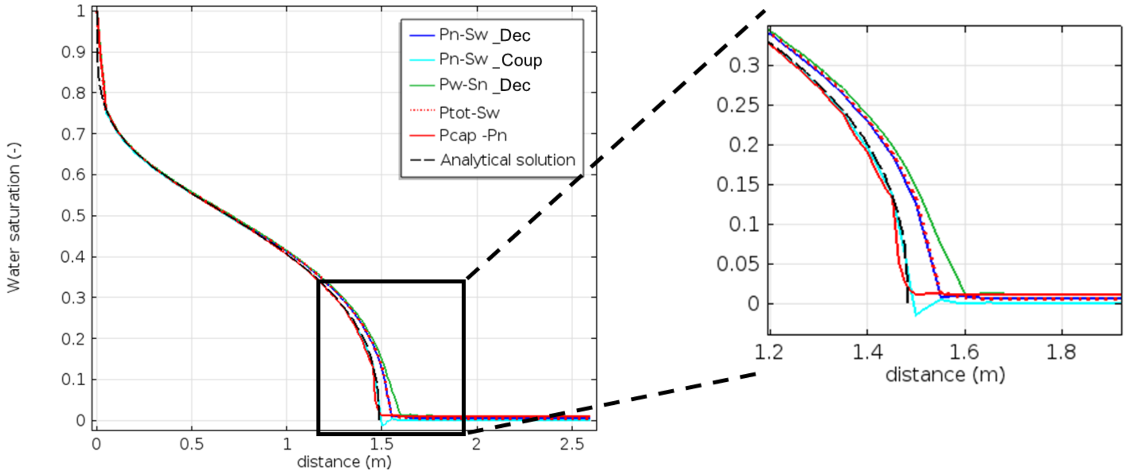

Figure 2-4. Water saturation profile after 2.78 hours of the McWhorter problem. The analytical and various numerical results are presented. The formulations are denoted by their dependent variables: non-wetting pressure (Pn), wetting pressure (Pw), non-wetting saturation (Sn), wetting saturation (Sw), global pressure (Ptot) and capillary pressure (Pcap). The suffix “Coup” and “Dec” denotes the coupled and decoupled pressure-saturation formulation respectively.

The location of the water saturation front after 2.78 hours is shown in

Figure 2-4. The numerical and analytical solutions are generally in good agreement for all the models. However, there are some differences at the saturation front. The coupled Pressure-Saturation formulation (Pn-Sw_Coup) is the most nonlinear. Despite it matches closely the analytical solution, a numerical instability appears at the water saturation front, with a clear undershooting. The capillary pressure (Pcap-Pn) formulation is the closest to the analytical solution. The global pressure (Ptot-Sw) and the decoupled non-wetting pressure/wetting saturation (Pn-Sw_Dec) formulations are also good approximations. Despite its similarities with the Pn-Sw_Dec the decoupled wetting pressure/non-wetting saturation (Pw-Sn_Dec) presents the poorest match with the analytical solution.

The performance of the formulations depends on the physical processes represented. The Pw-Sn_Dec formulation could be a better if the opposite process (i.e. the displacement of a wetting phase by a non-wetting phase) is modelled. The continuously defined variables (Pcap and Ptot) facilitate the convergence of the models, being appropriate for a larger range of applications. However, the complexity to assign initial and boundary conditions to these continuous variables hinders their application. In the cases presented in the next chapters of this thesis, decoupled pressure-saturation formulations are used.

Table 2-3. McWhorter model parameters.

	Parameter	Symbol	Value	Unit
Aquifer	Porosity	ϕ	0.3	-
	Permeability	k	1x10^{-10}	m^2
Retention curve	Entry pressure	p_t	5x10^{4}	Pa
	Pore index	ω	2	-
	Residual water saturation	S_w^r	0	-
	Residual oil saturation	S_o^r	0	-
Fluid properties	Water density	ρ_w	1x10^{3}	$kg\cdot m^{-3}$
	Oil density	ρ_o	1x10^{3}	$kg\cdot m^{-3}$
	Water viscosity	μ_w	1x10^{-3}	$Pa\cdot s^{-1}$
	Oil viscosity	μ_o	1x10^{-3}	$Pa\cdot s^{-1}$
Initial conditions	Oil saturation	S_o	1	-
	Water saturation	S_w	1x10^{-10}	-
	Oil pressure	P_o	2x10^{5}	Pa
	Water pressure	P_w	0	Pa
	Capillary pressure	P_{cap}	5x10^{8}	Pa
	Global pressure	P_{tot}	1.95x10^{5}	Pa
Boundary conditions	Oil saturation x=0	S_o	1	-
	Water saturation x=0	S_w	1	-
	Oil pressure x=0	P_o	2x10^{5}	Pa
	Water pressure x=0	P_w	1.95x10^{5}	Pa
	Capillary pressure x=0	P_{cap}	5x10^{4}	Pa
	Global pressure x=0	P_{tot}	1.95x10^{5}	Pa

2.1.3.3 Well leakage problem

Based on the studies on semi-analytical solutions of Nordbotten for investigating the migration of CO_2 plumes and the leakage through abandoned wells (Nordbotten et al., 2005, 2004a, 2004b); Ebigbo et al. (2007) developed a problem for code comparison. The model simulates the migration of CO_2 through a horizontal aquifer until it reaches a leaky well, where CO_2 rises towards a shallower aquifer (Figure 2-5).

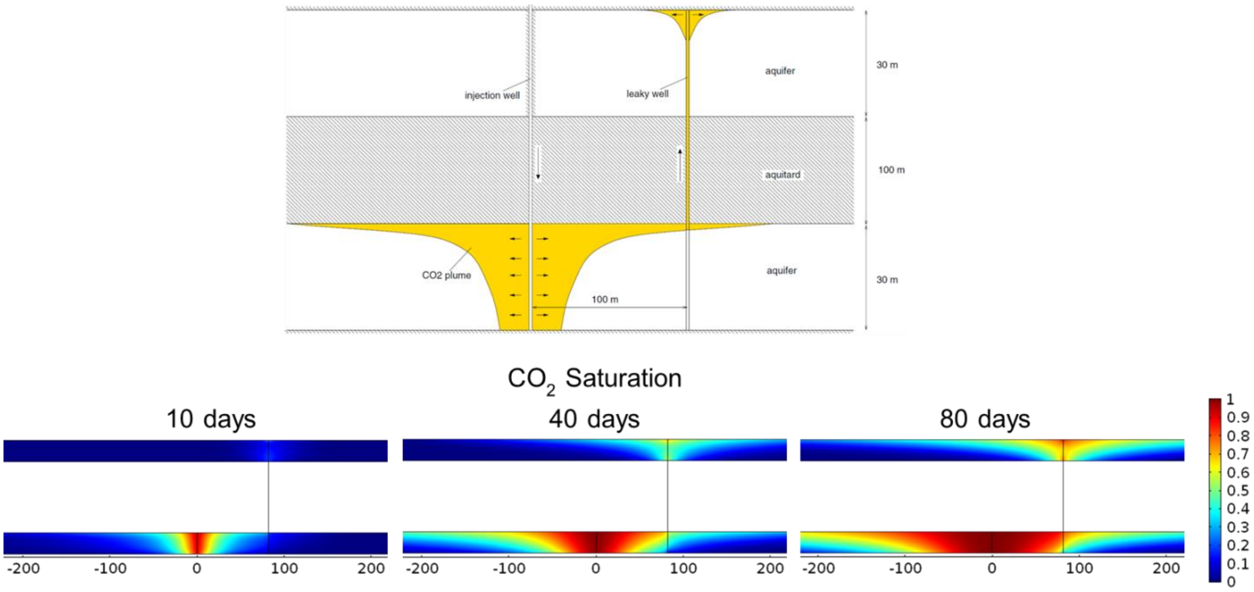

Figure 2-5. Conceptual model from Class et al. (2009) and modelling results of the CO_2 plume for the problem A at 10, 40 and 80 days.

Two problems, A and B, are proposed. In problem A, the system is solved assuming immiscible fluids without considering capillary pressure. The density and viscosity of the fluids is constant and the aquifer bottom is 3000 m depth. In problem B, the fluids are assumed miscible. The capillary pressure is taken into account and relative permeabilities are estimated using the Brooks and Corey (1964) relations (Table 2-2). The aquifer is much shallower than in case A with a maximum depth of 800 m and fluid properties are function of the aquifer conditions (Table 2-5). Problem B is supposed to solve the balance equation for thermal energy; however, most of the codes simulating this problem do not consider the thermal problem (Class et al., 2009).Thus, a constant geothermal gradient have been considered in this simulation.

The 3D domain is composed by two aquifers of 30 m width separated by an aquitard of 100m (Figure 2-5). A highly permeable leaking well located at the center of the domain connects both aquifers. The injection well is located 100 m from the leaking well. The aquifers are initially filled with brine and hydrostatic pressure conditions are considered. Dirichlet boundary conditions equal to the initial condition are imposed in the lateral boundaries, while no flow is allowed at the boundaries in contact with the aquitard. The CO_2 injection rate is in both cases of 8.87 $kg \cdot s^{-1}$. The total simulation time is 1000 days in problem A and 2000 days in problem B. The parameters of the model are described in Table 2-5. Problem A is solved with the equation 2-28 and 2-29 while compositional model described in equation 2-13 to 2-15 is used in problem B.

The CO_2 mass flux leaking through the leaky well is used for code comparison. The flux is calculated in the midway between the top and bottom aquifers. The CO_2 mass evolution on this point is show divided by the injection rate in percent. The problem solution is compared in Class et al. (2009) for various multiphase codes: MUFTE (Assteerawatt et al., 2005), DUMU^x (Flemisch et al., 2011), TOUGH2 (Pruess et al., 1999; Pruess and Spycher, 2007), ECLIPSE (ECLIPSE, 2004), ELSA (Nordbotten et al., 2009, 2004b), FEHM (Pawar et al., 2005), IPARS (Wheeler and Wheeler, 2001), COORES (Le Gallo et al., 2006; Trenty et al., 2006), VESA (Gasda et al., 2006), Rockflow (Fillion and Noyer, 1996) and RTAFF (Sbai, 2007).

The results of the multiphase flow formulations implemented for problem A (Figure 2-6) and B (Figure 2-7) are compared with the maximum and minimum CO_2 leaking fluxes calculated in Class et al. (2009). Furthermore, Table 2-4 shows the time of arrival of the CO_2 to the leaky well, the time and value of the maximum leakage and the CO2 leakage at the end of the simulation (1000 days in problem A and 2000 days in problem B). The results are comparable with the values obtained by the codes on Class et al. (2009). The differences between code results increase with the complexity of the problem. Problem A shows a better agreement between the codes than problem B. The divergence between results can be due to different physical parameters (e.g. density and viscosity relations, miscibility) and due to spatial discretization. The grid size in the vicinity of the wells can have a significant influence on the results. In our simulations, the smallest grid size in the well is of 0.1 m.

Table 2-4. Characteristic values of the simulations of problems A and B. The table fields are the same than tables 8 and 9 in Class et al. (2009).

	Problem A	**Problem B**	**Unit**
Maximum leakage	0.222	0.08	(%)
Time at maximum leakage	60	300	days
Leakage at simulation end	0.1291	0.05	(%)
Arrival time	4	50	days

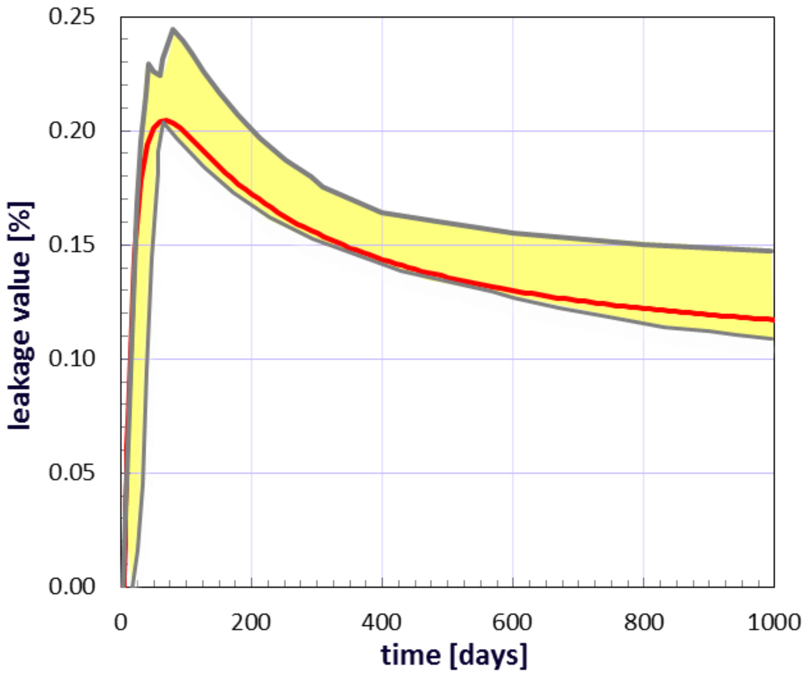

Figure 2-6. Leakage rates through leakage well for problem A. Model result (red) is compared with the values obtained by various models in Class et al. (2009) (yellow area).

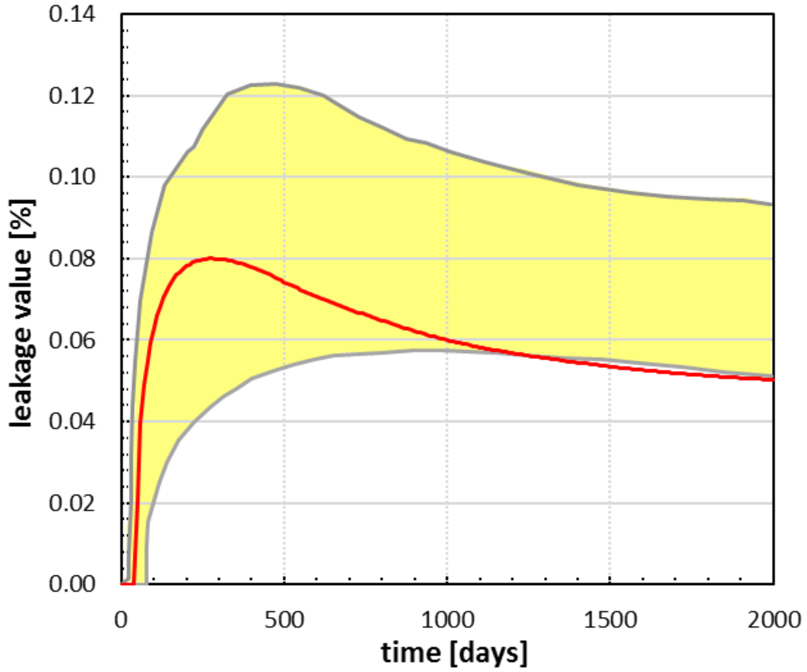

Figure 2-7. Leakage rates through leakage well for problem B. Model result (red) is compared with the values obtained by various models in Class et al. (2009) (yellow area).

Table 2-5. Well leakage model parameters.

	Parameter	**Symbol**	**Problem A**	**Problem B**	**Unit**
Domain geometry	Aquifer depth		2840-3000	640-800	m
	Aquifer thickness		30		m
	Aquitard thickness		100		m
	Domain dimensions		1000x1000x160		m
	Distance between wells		100		m
	Well radius		0.15		m
Aquifer	Porosity	ϕ	0.3		-
	Aquifer permeability	k_{aq}	2x10^{-14}		m^2
	Leaky well permeability	k_{well}	1x10^{-12}		m^2
	Temperature at bottom	T_0	-	34	C
	Geothermal gradient	k_T	-	0.03	$C \cdot m^{-1}$
Retention curve	Entry pressure	p_t	-	1x10^4	Pa
	Pore index	ω	-	2	-
	Residual brine saturation	S_w^r	0	0.2	-
	Residual oil saturation	S_o^r	0	0.05	-
Fluid properties	Brine density	ρ_w	1045	$f(T, p, S, X_w^{Co_2})$	$kg\cdot m^{-3}$
	CO$_2$ density	ρ_o	479	$f(T, p)$	$kg\cdot m^{-3}$
	Brine viscosity	μ_w	2.535x10^{-4}	$f(T, p)$	$Pa\cdot s^{-1}$
	CO$_2$ viscosity	μ_o	3.95x10^{-5}	$f(T, p)$	$Pa\cdot s^{-1}$
	Mutual solubilities		Neglected	$f(T, p, S)$	$kg \cdot m^{-3} \cdot s^{-1}$
Initial conditions	Oil saturation	S_o	0		-
	Brine saturation	S_w	1		-
	Brine pressure	P_w	Hydrostatic pressure		Pa
	Brine pressure at bottom	P_w	3.086x10^7	8.499x10^6	Pa
Boundary conditions	Latera brine saturation	S_w	1		-
	Lateral brine pressure	P_w	Hydrostatic pressure		Pa
	Other boundaries	P_{tot}	No flow		Pa
	Injection rate	Q_{in}	8.87		$kg \cdot s^{-1}$

2.2 Solute transport

Many natural phenomena in the subsurface environment involve coupled systems where multiple physical processes interact; such phenomena can include groundwater flow, solute transport, chemical reactions, heat exchange and mechanical deformation. Traditionally, these processes have been represented by tailored numerical codes that solve a specific set of physics. Flow and reactive transport, for instance, can be solved by a series of codes in 1D: PHREEQC (Parkhurst and Appelo, 2013), ORCHESTRA (Meeussen, 2003) and HYDRUS-1D (Šimůnek et al., 2009); and with more complex geometries: PHAST (Parkhurst et al., 2010), HYTEC (Sin et al., 2017; Van der Lee et al., 2003), MIN3P (Mayer and MacQuarrie, 2010), eSTOMP (White and Oostrom, 2006) and MoReS (Farajzadeh et al., 2012; Wei, 2012).

The computational capabilities, both in terms of hardware and in numerical methods, have increased exponentially over the past two decades; allowing the solution of complex coupled thermo-hydro-chemical-mechanical (THMC) systems. At present, a set of multidimensional codes is able to cope with those phenomena: RETRASO-Codebright (Saaltink et al., 2004), CORE (Samper et al., 2003), TOUGHREACT (T. Xu et al., 2006), OpenGeoSys (O. Kolditz et al., 2012a), PFLOTRAN (Lu and Lichtner, 2005; Mills et al., 2007), CRUNCHFLOW (Steefel, 2009), HYDROGEOCHEM (Tsai et al., 2013) and DUMU^{X} (Ahusborde et al., 2015; Flemisch et al., 2011; Vostrikov, 2014). The description of these codes is out of the scope of this thesis. A good review and comparison of some of these codes can be found in Steefel et al. (2015).

Two approaches exist to solve the coupled reactive transport equations: the global implicit (GI) and the operation splitting (OS) approach (Fahs et al., 2008; Molins et al., 2004; Saaltink et al., 2001, 2000; Steefel and MacQuarrie, 1996; Strang, 1968; Yeh and Tripathi, 1989). GI introduces the chemical equations in the transport equation, solving simultaneously the system of equations. It is based on the Newton-Raphson method. If the system is solved directly for the total concentrations and, then, the distribution of each species calculated; the method is known as the global implicit approach (GIA). Another option is the direct substitution approach (DSA), where the complexation is also solved simultaneously and the primary species are the system unknowns. In contrast, OS solves the chemical and transport equations sequentially based on the Picard method. If the sequential solver is repeated until a convergence is achieved, the method is called sequential iterative approach (SIA); while in the sequential non-iterative approach (SNIA) no convergence criteria is imposed.

Various studies comparing these approaches are available in the literature (Barry et al., 1996; Carrayrou et al., 2004; Jacques et al., 2006). The GI approach has the advantage that is unconditionally stable and its time step is not restricted by the Courant condition. However, is computationally expensive especially in multicomponent-multispecies systems. The SNIA is the most efficient method and does not pose global convergence problems; although it could generate splitting errors and a tight control on the time step is necessary. The SIA is an intermediate solution. The computational time required is larger than for the SNIA, however, the splitting error decreases by the iterations in each time step.

The OS approaches have a modular framework that facilitates the integration of independent codes or modules. This flexible structure allows the extension of the code with new modules and capabilities. In last years, the coupling of independent codes to simulate reactive transport processes has extended: HYDRUS and PHREEQC (Jacques and Šimůnek, 2005; Šimůnek et al., 2009; Šimůnek and Genuchten, 2006); Modflow with RT3D (Bailey et al., 2013) and MT3DMS (Morway et al., 2012); FEFLOW and PHREEQC (Sousa, 2012); COMSOL and PHREEQC (Nardi et al., 2014b; Nasir et al., 2014; Wissmeier and Barry, 2011); COMSOL and GEMS (Azad et al., 2016); OpenGeoSys with GEMs (Kosakowski and Watanabe, 2014; Shao et al., 2009) and PHREEQC (De Lucia et al., 2012; He et al., 2015).

iCP code (Nardi et al., 2014a) is used for the modelling of reactive transport in this thesis. iCP couples two independent programs: COMSOL (Comsol, 2016) and the geochemical simulator PHREEQC (Parkhurst and Appelo, 2013) through a SNIA approach (Figure 2-8). The coupling with PHREEQC is done through the iPhreeqc library (Charlton and Parkhurst, 2011). Conservative solute transport is computed in a first step with COMSOL, potentially coupled with other physical processes; while geochemistry is solved in a second step with PHREEQC. Various couplings can be introduced between COMSOL and PHREEQC. In the OS approach the variables evaluated in COMSOL and used to solve the geochemical system (i.e. liquid pressure, gas volume, temperature, or mass of water) are solved in a first step and, therefore, are updated before the second step. The coupling variables solved in PHREEQC and later used in COMSOL (i.e., porosity, water consumption, mass water fraction, or gas consumption) are evaluated in lagged time.

iCP maximizes the synergies between both codes. Its flexibility and wide range of applicability make iCP suitable for many modelling challenges in various fields of Earth Sciences. It has been successfully applied to model complex natural and engineered environments (Karimzadeh et al., 2017; Sainz-Garcia et al., 2017).

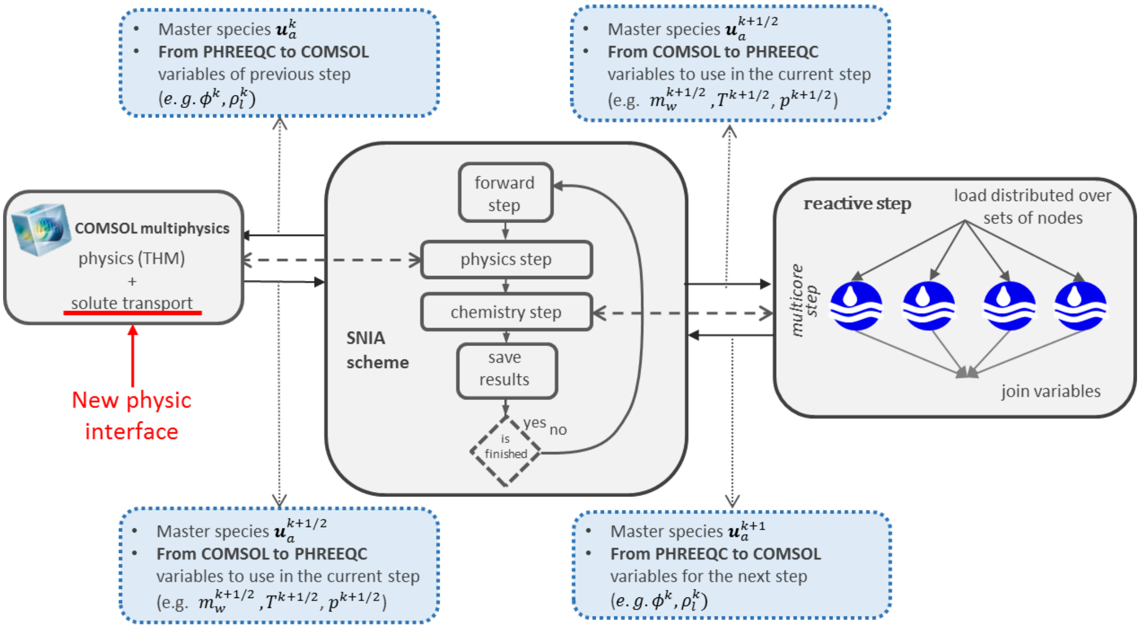

Figure 2-8. One step SNIA structure of iCP. The transport, potentially coupled with other physical processes, is solved in the first step by COMSOL and the chemical reactions are solved in a second step by PHREEQC. The PHREEQC calculations are parallelized by iCP. The main variables transferred in each step are pointed. The implemented conservative solute transport module is highlighted.

During this thesis, a new solute transport module that simplifies the integration of COMSOL and PHREEQC has been implemented (Figure 2-8). The module is consistent with the units and the reactive transport formulation used in iCP. In this section the main characteristics of this module are explained.

2.2.1 Mathematical model

The mass balance of water in a variably saturated porous media can be expressed by:

$$\frac{\partial(\phi S_l \rho_l \omega_l^w)}{\partial t} = -\nabla\cdot(\rho_l \boldsymbol{q}_l \omega_l^w) + \nabla\cdot(\mathbf{D}_l \rho_l \nabla \omega_l^w) + f_{ext}^w + f_s^w \qquad (2\text{-}30)$$

where ω_l^w is the water mass fraction in the liquid ($kg_w \cdot kg_l^{-1}$), f_{ext}^w is an external source of water ($kg_w \cdot m^{-3} \cdot s^{-1}$) and f_s^w is the source term accounting for phase changes ($kg_w \cdot m^{-3} \cdot s^{-1}$). The liquid diffusion/dispersion tensor ($\boldsymbol{D}_l$) is evaluated like in equation (2-4) and the liquid Darcy's flow for a single phase ($\boldsymbol{q}_l$) is defined as:

$$\boldsymbol{q_l} = -\tfrac{\kappa}{\mu}(\nabla p - \rho \boldsymbol{g}) \tag{2-31}$$

kg_w denotes kilograms of pure water.

The mass balance of a chemical species is defined as:

$$\begin{aligned}\frac{\partial(\omega \boldsymbol{c})}{\partial t} &= \boldsymbol{c}\frac{\partial(\omega)}{\partial t} + \omega\frac{\partial(\boldsymbol{c})}{\partial t} \\ &= -\nabla \cdot (\psi \boldsymbol{q_l} \boldsymbol{c}_a) + \nabla \cdot (\psi \boldsymbol{D_l} \nabla \boldsymbol{c}_a) + f_{ext}^{w} c_a^{*} + \omega \boldsymbol{r}_{eq} + \omega \boldsymbol{r}_{kin}\end{aligned} \tag{2-32}$$

where $\boldsymbol{c}$ is the concentration vector of all species ($mol \cdot kg_w^{-1}$), $\boldsymbol{c}_a$ is the concentration vector of aqueous species ($mol \cdot kg_w^{-1}$), $\boldsymbol{c}_a^{*}$ is the concentration vector of the aqueous species in an external boundary water ($mol \cdot kg_w^{-1}$), $\boldsymbol{r}_{eq}$ is the reactive rate vector related to equilibrium reactions ($mol \cdot kg_w^{-1} \cdot s^{-1}$), and $\boldsymbol{r}_{kin}$ is the reactive rate vector due to kinetic reactions ($mol \cdot kg_w^{-1} \cdot s^{-1}$). The auxiliary variables ω and ψ are defined as:

$$\omega = \phi S_l \rho_l \omega_l^{w} \tag{2-33}$$

$$\psi = \rho_l \omega_l^{w} \tag{2-34}$$

Equation (2-32) is the divergence form of the solute transport equation. An alternative (convective) form can be archived by subtracting water mass balance multiplied by solute concentration (Galeati and Gambolati, 1989; Goode, 1992; M. W. Saaltink et al., 2004):

$$\begin{aligned}\omega\frac{\partial(\boldsymbol{c})}{\partial t} = &-\psi \boldsymbol{q_l} \nabla \boldsymbol{c}_a + \nabla \cdot (\psi \boldsymbol{D_l} \nabla \boldsymbol{c}_a) - \boldsymbol{c}_a \nabla \cdot \mathrm{\rho_l} \boldsymbol{D_l} \nabla \omega_l^{w} - f_{ch}^{w} \boldsymbol{c}_a \\ &+ f_{ext}^{w}(\boldsymbol{c_a^{*}} - \boldsymbol{c}_a) + \omega \boldsymbol{r}_{eq} + \omega \boldsymbol{r}_{kin}\end{aligned} \tag{2-35}$$

The convective form is more stable when using the Galerkin finite element methods (Galeati and Gambolati, 1989; Huyakorn et al., 1985) and is implemented in iCP. Note that equation (2-35) does not depend on variations of water mass.

If the system of equations (2-35) is written over chemical component instead of chemical species, the system can be reduced. A chemical component is defined as a linear combination of species which mass is not affected by equilibrium reactions (Lichtner, 1985; Saaltink et al., 1998; Smith and Missen, 1982; Steefel and MacQuarrie, 1996). There is, then, a component matrix ($\boldsymbol{U}$) that fulfils:

$$
\begin{aligned}
\boldsymbol{Ur_{eq}} &= 0 \\
\boldsymbol{u} &= \boldsymbol{Uc}
\end{aligned}
\tag{2-36}
$$

where $\boldsymbol{u}$ is the vector of components $(mol \cdot kg_w^{-1})$ (Saaltink et al., 1998). The system in (35) has to solved, thus, the total number of components (N_c). N_c is always less than the total number of species (N_s):

$$
N_c = N_s - N_{eq} \tag{2-37}
$$

where N_{eq} is the number of equilibrium reactions in the system. The reduced system is expressed as:

$$
\begin{aligned}
\omega \frac{\partial(\boldsymbol{c})}{\partial t} = &-\psi \boldsymbol{q_l} \nabla \boldsymbol{u}_a + \nabla \cdot (\psi \boldsymbol{D_l} \nabla \boldsymbol{u_a}) - \boldsymbol{u_a} \nabla \cdot \rho_l \boldsymbol{D_l} \nabla \omega_l^w - f_{ch}^w \boldsymbol{u_a} \\
&+ f_{ext}^w (\boldsymbol{u_a^*} - \boldsymbol{u}_a) + \omega \boldsymbol{Ur}_{kin}
\end{aligned}
\tag{2-38}
$$

In the SNIA scheme of iCP, the transport of conservative solutes is evaluated in the first step and the geochemical reactions solved in the second step by PHREEQC. In PHREEQC the vector of chemical components $(\boldsymbol{u}_a)$ corresponds to the so-called "master species". The conservative transport of components in variable saturated porous media implemented in COMSOL has the following form:

$$
\omega \frac{\partial(\boldsymbol{u}_a)}{\partial t} = -\psi \boldsymbol{q_l} \nabla \boldsymbol{u}_a + \nabla \cdot (\psi \boldsymbol{D_l} \nabla \boldsymbol{u_a}) - \boldsymbol{u_a} \nabla \cdot \rho_l \boldsymbol{D_l} \nabla \omega_l^w - f_{ch}^w \boldsymbol{u_a} + f_{ext}^w (\boldsymbol{u_a^*} - \boldsymbol{u_a})
\tag{2-39}
$$

The solute transport equation is tailored to meet the necessities of iCP (i.e., the unit of the unknowns is $(mol \cdot kg_w^{-1})$, the diffusion coefficient is equal for all components,…). The problem can be solved in stationary or time-dependent analysis. As boundary conditions the solute transport can have:

- No mass flow:

$$
0 = -\boldsymbol{n} \cdot (\boldsymbol{q_l} \cdot \nabla \boldsymbol{u}_a + \psi \boldsymbol{D_l} \cdot \nabla \boldsymbol{u}_a - \boldsymbol{u}_a \mathrm{P_L} \boldsymbol{D_l} \cdot \nabla \omega_l^w) \tag{2-40}
$$

- Prescribed concentration:

$$
\boldsymbol{u}_a = \boldsymbol{u_a^*} \tag{2-41}
$$

- Outflow. Note that this condition assumes that the mass flux due to dispersion/diffusion across the boundary is zero, being advection the only process for mass flow through the boundary:

$$
0 = -\boldsymbol{n} \cdot (\psi \boldsymbol{D_l} \cdot \nabla \boldsymbol{u}_a - \boldsymbol{u}_a (\rho_l \boldsymbol{D_l} \cdot \nabla \omega_l^w)) \tag{2-42}
$$

- Open Boundary, where both inflow and outflow across boundaries are allowed. The mass transfer is due to advection, considering that dispersion/diffusion effects are negligible. In the case of a fluid leaving the domain, the condition is equivalent to the “Outflow” condition.

$$\begin{gathered} Inflow\ condition: 0 = (\boldsymbol{q_l} \cdot \boldsymbol{n})\psi(\boldsymbol{u}_a - \boldsymbol{u}_a^*) \\ Outflow\ condition: 0 = -\boldsymbol{n} \cdot (\psi \boldsymbol{D_l} \cdot \nabla \boldsymbol{u}_a - \boldsymbol{u}_a(\mathrm{P_L} \boldsymbol{D_l} \cdot \nabla \omega_l^w)) \end{gathered} \tag{2-43}$$

2.2.2 Numerical method

The conservative solute transport module is implemented in the finite element method framework COMSOL Multiphysics. A standard-Galerkin method with continuous Lagrange shape functions is used. The order of the shape functions is user-defined and can vary between linear to quintic. As both share the same platform the solution scheme and the linear system solvers are the same as the ones explained for the multiphase flow (section 2.1.2). Implicit and explicit schemes can be applied and the system of equations can be solved by iterative as well as direct methods.

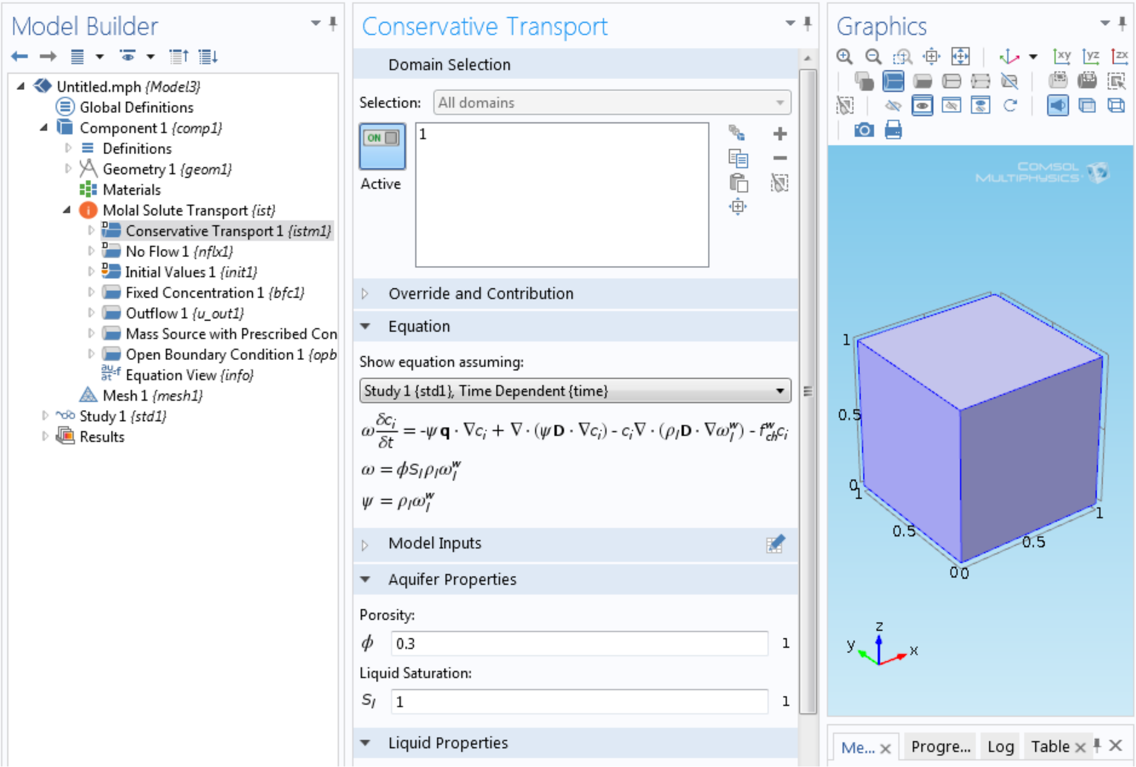

Untitled.mph {Model3}
Global Definitions
Component 1 {comp1}
Definitions
Geometry 1 {geom1}
Materials
Molal Solute Transport {ist}
Conservative Transport 1 {istm1}
No Flow 1 {nflx1}
Initial Values 1 {init1}
Fixed Concentration 1 {bfc1}
Outflow 1 {u_out1}
Mass Source with Prescribed Con
Open Boundary Condition 1 {opb
Equation View {info}
Mesh 1 {mesh1}
Study 1 {std1}
Results

Selection: All domains

1

Show equation assuming:

Study 1 {std1}, Time Dependent {time}

$$\omega\frac{\delta c_i}{\delta t} = -\psi\,\mathbf{q}\cdot\nabla c_i + \nabla\cdot(\psi\mathbf{D}\cdot\nabla c_i) - c_i\nabla\cdot(\rho_l\mathbf{D}\cdot\nabla\omega_l^w) - f_{ch}^w c_i$$

$$\omega = \phi S_l \rho_l \omega_l^w$$

$$\psi = \rho_l \omega_l^w$$

Porosity:

ϕ 0.3 1

Liquid Saturation:

S_l 1 1

Figure 2-9. GUI of the component solute transport module implemented in COMSOL. The panel at the left show the solute transport module with the boundary and initial conditions available. The panel at the middle shows the equation solved and allow the user to assign the parameters and variables. The right panel shows the geometry of the model. The parts of the geometry where a physical process or boundary should be taken into account can be interactively selected.

A java package of the solute transport module has been created, allowing the integration of the module as plug-in in any COMSOL model. The module has a graphical user interface (GUI) that facilitates the user interaction (Figure 2-9).

2.2.1 *Verification:*

iCP with the solute transport module presented in this section has been verified through a series of benchmarks (Nardi et al., 2014b). The cation exchange benchmark is presented below. Three other benchmarks developed by other iCP users and are presented in Annex II.

2.2.1.1 *Cation exchange problem*

The Example 11 of the PHREEQC User's Guide (Parkhurst and Appelo, 2013) has been widely used as benchmark problem (O. Kolditz et al., 2012b). It simulates the transport of solutes in a 1D saturated column that is flushed by a calcium-chloride solution (Figure 2-10). Initially the column is filled by a sodium-potassium-nitrate solution in equilibrium with the exchanger. iCP results are compared with PHREEQC, PHAST (Parkhurst et al., 2010) and CRUNCHFLOW (Steefel, 2009).

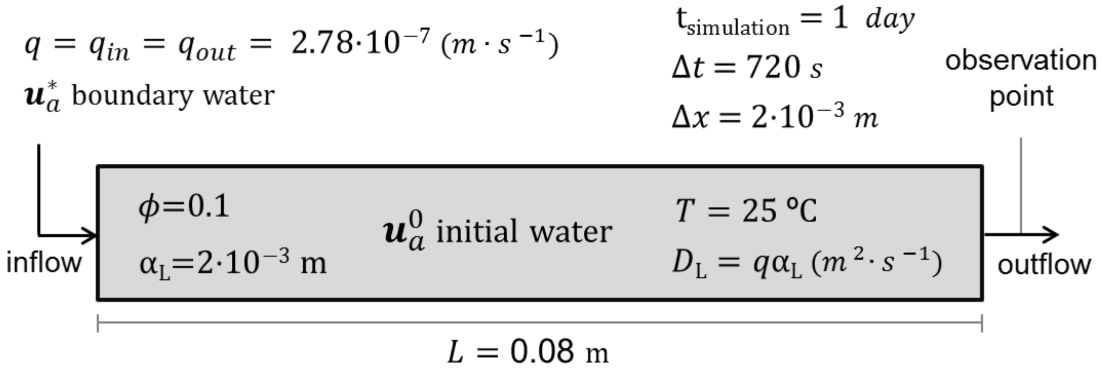

Figure 2-10. Physics and parameters of the Benckmark Problem 3: Cation Exchange.

The 1D domain is 0.08 m long. The transport accounts for advection and dispersion with a prescribed water flux and outflow boundary conditions. When the calcium-rich solution enters the column, the sorbed Na and K are replaced by Ca (Figure 2-11). Na is weakly exchanged (has lower equilibrium constant than K) and is first released from the exchanger and flushed out of the column. When the Na is exhausted, potassium is released from the exchanger. Dissolved K increases above the initial concertation to balance the incoming Cl. When K is the only cation in solution is also the only cation on the exchanger; leading to higher sorbed potassium concentrations. Finally, the K in the exchanger is depleted and all the K is flushed from the column. Chloride and nitrate are conservative solutes and Cl replace N without any effect of the exchanger. Table 2-6 presents the relevant parameters of the model. The thermodynamic data is taken from the PHREEQC.dat database.

Table 2-6. Cation exchange model parameters.

	Parameter	**Symbol**	**Value**	**Unit**
Aquifer	Porosity	ϕ	0.1	-
	Temperature	T	25	°C
Transport properties	Longitudinal dispersivity	α_L	2 x10^{-3}	-
	Darcy flow	q	2.78 x10^{-7}	$m \cdot s^{-1}$
Fluid properties	Water density	ρ_w	1x10^3	$kg \cdot m^{-3}$
Initial water composition	pH		7	-
	pe		12.5	
	Na		1.0	$mmol\cdot kgw^{-1}$
	K		0.2	$mmol\cdot kgw^{-1}$
	N(5)		1.2	$mmol\cdot kgw^{-1}$
	Ion exchanger		0.0011	$mmol\cdot kgw^{-1}$
Boundary water composition	pH	P_o	7.0	-
	pe	S_w	12.5	-
	Ca	Q_0	0.6	$mmol\cdot kgw^{-1}$
	Cl	S_w	1.2	$mmol\cdot kgw^{-1}$

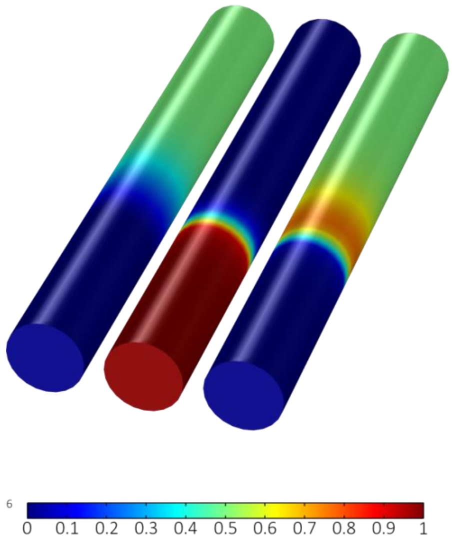

Figure 2-11. From left to right: NaX, CaX2 and KX exchanger fractions after 4h. Despite the problem is 1D a 3D column is modelled for demonstation purposes.

The dissolved concentrations at the end of the column serve as comparison between the codes (Figure 2-12). Results from PHREEQC, PHAST, CRUNCHFLOW and ICP are in good agreement.

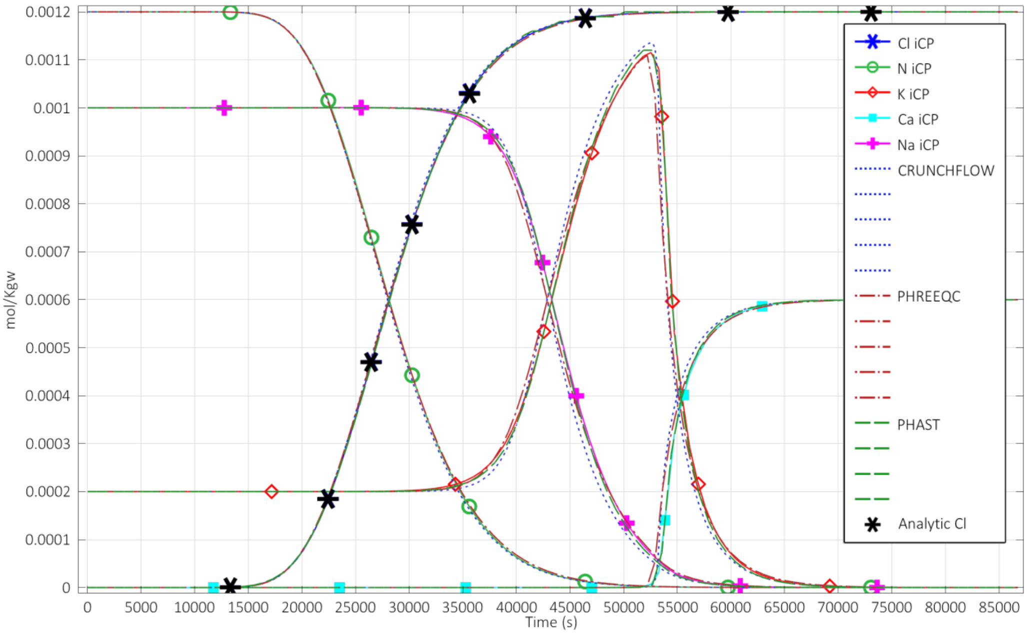

Figure 2-12: Comparison of the breacktrough curves of Cl, N, Na, K and Ca at the end of the column. The results of PHREEQC, PHAST, CRUNCHFLOW and ICP are plotted.

2.3 Comments on the numerical tools

Various multiphase flow formulations and a solute transport module in porous media have been developed and implemented in COMSOL. The numerical tools have been verified through various benchmarks and are applied to model the dynamics of underground gas storage in chapters 3 and 4.

The highly flexible numerical framework of COMSOL provides a large number of options for the solution algorithm and scheme of the PDE systems. The platform is continuously updated ensuring the availability of state of the art numerical methods and solvers. It has a powerful pre and post-processing interface with strong meshing capabilities that helps the user to save time in setup and visualization; focusing in the analysis of results and implementation details. It has also a certified quality assurance process that promotes its industrial application. When modelling convection-diffusion processes the Galerkin FEM spatial discretization used in COMSOL could lead to an oscillatory behavior that can be balanced by numerical stabilization methods. Nevertheless, a tight control on the spatial discretization is recommended to avoid oscillations.

The multiphase flow formulations implemented has been proven to properly reproduce the migration of two fluid phases in the subsurface. A series of immiscible formulations are available and the one selected may depend on the processes reproduced in each application. The compositional formulation proposed maintains the same dependent variables throughout the model domain. Switching variables can be efficient to face phase disappearing; however, it affects the structure of the Jacobian matrix. Using the same dependent variables facilitates the integration of this formulation in modular reactive transport codes as iCP.

The component partitioning between the gas and liquid phase is expressed by a kinetic rate. The equilibrium can be simulated by imposing a high kinetic rate; however, other mass transfers can be accounted. This approach broads the possibilities of the code. Nevertheless, few experimental data on kinetic mass transfer between phases are available on literature.

A fully implicit scheme and direct solvers have been used in the application models presented in this thesis. This method is robust and unconditionally stable and no time step restriction controls the temporal discretization; however, the method is computationally expensive. To date only one phase one component systems have been simulated.

The component solute transport module in porous media is developed using the convective form of the equation, which is more stable in Galerkin FEM. The module facilitates the transfer of information between COMSOL and iCP and it has been successfully applied in dozens of models.

iCP maximizes the synergies between COMSOL and PHREEQC, inheriting the capabilities of both codes. It combines the flexibility and wide range of applications and couplings from COMSOL with the most widely used code for geochemical processes. The SNIA approach does not pose global convergence problems although a tight control on the time step is required. At every step COMSOL has to reconstruct the matrix system, leading to a computational time penalty. It is, then, a reactive transport code appropriate for coupled systems (e.g. THMC problems) with complicated geometries or complex physical processes, rather than models with simple geometries without process coupling. A summary of the capabilities of the code is given in Table 2-7. The table has the same fields than tables 1, 2 and 3 in Steefel et al. (2015) to allow the comparison with other reactive transport codes.

The coupling of the multiphase formulations with reactive transport through iCP would generate a useful tool for multiphase flow challenges in porous media. There are already some codes that can deal with such processes: HYTEC (Sin et al., 2017; Van der Lee et al., 2003), MIN3P (Mayer and MacQuarrie, 2010), eSTOMP (White and Oostrom, 2006), MoReS (Farajzadeh et al., 2012; Wei, 2012), TOUGHREACT (T. Xu et al., 2006), PFLOTRAN (Mills et al., 2007), HYDROGEOCHEM (Tsai et al., 2013), RETRASO-CodeBright (Saaltink et al., 2004), DUMUX (Ahusborde et al., 2015; Vostrikov, 2014) and COORES (Tillier et al., 2007). The flexibility of iCP would allow the representation of a large range of multiphase physical processes (e.g. thermal and mechanical processes could be account).

Other interesting field for future expansion of the numerical tools is the integration of surface water with groundwater phenomena. This tool could improve our understanding of the processes affection the surface and near-surface and the interaction of the hydrosphere with the biosphere (plants and microbial activity).

Table 2-7. Key features of iCP. Same fields as Tables 1 to 3 from Steefel et al. (2015) are detailed.

	Capabilities/Features	iCP
	Dimensions	1,2,3D, Axisymmetric
Flow	Saturated flow	Yes
	Richards equation	Yes
	Multiphase-multicomponent flow	No
	Variable density flow	Yes
	Non-isothermal flow	Yes
Transport	Advection	Yes
	Molecular diffusion	Yes
	Electrochemical migration	No
	Dispersion tensor	Full, Diagonal
	Gas phase advection	Yes
	Gas phase diffusion	Yes
	Colloids	Yes
	Multiple continua	Yes
Numerical scheme	Operation splitting	Yes
	Global implicit	No
	High Peclet number transport	Yes
	Spatial discretization	FEM
	Time discretization	Implicit, Explicit, IAM
Computational	Parallelization	Yes
	Inverse estimation	No
	Graphical user interface	Yes
	Open source	No
Geochemistry	Extended Debye-Hückel	Yes
	Davies activity model	Yes
	Pitzer activity model	Yes
	Non-isothermal	Yes
	Surface complexation	DDL, Non-edl
	Ion exchange	Yes
	Aqueous-gas exchange	Yes
	Kinetic mineral precipitation-dissolution	Yes
	Mineral nucleation	Yes
	Mineral solid-solutions	Yes
	Equilibrium isotope fractionation	Yes
	Aqueous kinetics	Yes
	Radioactive decay chains	Yes
Microbial	Monod kinetics	Yes
	Thermodynamic	Yes
	Biomass growth	Yes
Coupling	Reaction induced porosity - permeability	Yes
	Coupled heat of reaction	Yes
	Coupled deformation/compaction	Yes
	Reaction consumption of phase	Yes
	Electrical double layer transport	Yes

In respect to the multiphase flow, the definition of a specific interfacial area between phases, as proposed by Niessner and Hassanizadeh (2009, 2008) and Niessner and Helmig (2007); could capture additional processes. Hysteresis as well as a more accurate description of the mass transfer between phases could be reproduced.

3 Carbon capture and storage

3.1 Carbon dioxide storage in porous media

One of the most promising technologies to mitigate anthropogenic greenhouse gas emissions is carbon capture and storage (CCS) (Boot-Handford et al., 2014; Chu, 2009; Edenhofer et al., 2014; Haszeldine, 2009; Lackner, 2003; Metz et al., 2005; Oelkers and Cole, 2008). Deep saline aquifers in sedimentary basins are widely distributed and have a large potential storage capacity able to sequester much of the emitted CO_2 from point sources (Bachu, 2003; Bradshaw et al., 2007; Firoozabadi and Cheng, 2010; Metz et al., 2005; Michael et al., 2010; Orr Jr, 2009; Szulczewski et al., 2012).

Most saline aquifers intend to maintain CO_2 under supercritical state for an efficient use of the underground storage space. Under this condition, CO_2 is less dense and viscous than the formation fluid and migrates upwards driven by buoyancy forces forming a gravity current. A well-sealed caprock is, therefore, needed to prevent the CO_2 leakage from the storage formation to overlying formations. This storing mechanism is known as structural or stratigraphic trapping (Metz et al., 2005). Once at the aquifer top, free-phase CO_2 will continuously extend following the caprock slope unless confined in a dome-shaped structure or retained by other physical and geochemical trapping mechanisms (Figure 3-1). During this migration, there is a risk of leakage through open faults or abandoned wells.

Capillary or residual trapping immobilize CO_2 in the pore space in disconnected ganglia due to interphase surface tension. During the migration of the gravity current, aquifer native fluid imbibes back areas previously occupied by CO_2 isolating and fixing small CO_2 blobs. Furthermore, due to differences in density and capillary pressure between the free-phase and the underlying fluid phase, a so-called capillary fringe or transition zone is formed (Golding et al., 2013, 2011; Nordbotten and Dahle, 2011). Capillarity reduces the risk of leakage, immobilizing the CO_2 over a large area, shrinking and reducing the propagation speed of the free-phase plume and enhancing the CO_2 dissolution (Doster et al., 2013; Hesse et al., 2008; Juanes et al., 2010, 2006; Kumar et al., 2005; Zhao et al., 2013).

Both residual and mobile CO_2 gradually dissolve into aquifer native fluid. The resulting CO_2-rich fluid is approximately 1% denser than ambient fluid (Ennis-King and Paterson, 2003; Garcia, 2001), preventing the buoyancy driven escape of CO_2 to upper layers or to the atmosphere. CO_2 dissolution is a key process for carbon storage. It increases storage safety by decreasing the CO_2 fugacity, lowering the pressure of the supercritical CO_2 and, thus, limiting the gas migration and pressure build up. Furthermore, dissolved CO_2 promotes water-rock interaction that could mineralize the carbon (Audigane et al., 2007; Xu et al., 2005), further increasing the stability of the storage.

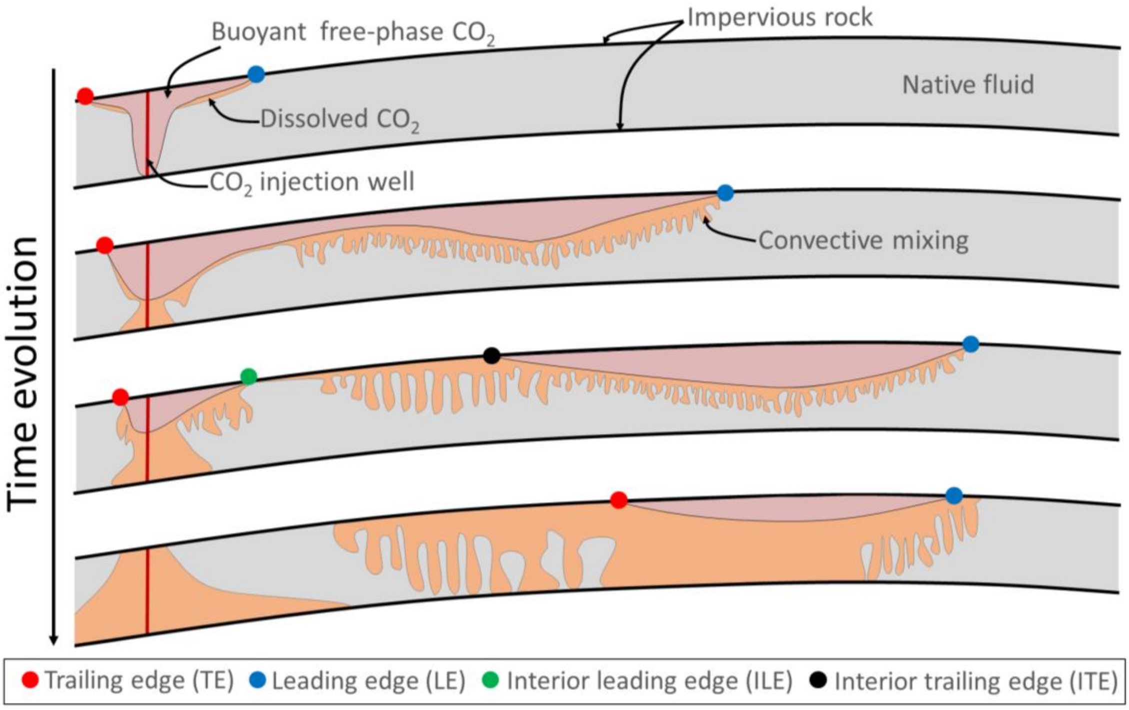

Figure 3-1. Schematic illustration of the CO_2 evolution in a saline dome-shape aquifer. Time increases downwards. The migration of free-phase CO_2 as well as its dissolution in the native fluid and the consequent convective mixing are depicted. Dots represent the edges of free-phase plume: the trailing edge (TE, red) and leading edge (LE, blue). When the plume splits, an interior trailing edge (ITE, green) and interior leading edge (ILE, black) are defined.

The presence of denser CO_2-rich fluid above the less dense native fluid lead to gravitational instabilities. This instability promotes convection that carries the CO_2-rich aqueous fluid downwards generating finger shape CO_2-concentration profiles (Ennis-King and Paterson, 2003; Hidalgo et al., 2013; Kneafsey and Pruess, 2010; Riaz et al., 2006). As thermodynamic equilibrium is rapidly attained between supercritical CO_2 and the native formation fluid, its dissolution is controlled by the fluid renewal rate. Fluid convection, therefore, can increase dramatically the CO_2 dissolution rate. Recently, field evidence of these processes have been observed (Sathaye et al., 2014). Emami-Meybodi et al. (2015) reviewed recent advances in CO_2 convective dissolution in saline aquifers through experiments, and theoretical and numerical models.

This chapter is divided into two sections. The first, focuses on the interaction between different CO_2 trapping mechanisms in the subsurface. It evaluates the fate of CO_2 in a syncline-anticline system with a large scale multiphase model. The second part of the chapter deals with the effects of chemical reaction in convective mixing, a critical process in carbon storage. It analyzes a short portion of a reservoir with a fully coupled reactive transport model.

3.2 Interactions of CO_2 gravity currents, capillarity, dissolution and convective mixing in a syncline-anticline system[1].

3.2.1 Introduction

Despite the relevant role of convective dissolution in carbon underground storage, the interplay between free-phase plume migration and this process is not completely understood. The wide range of temporal and spatial scales involved in the problem (the long gravity plume and the detailed convective mixing), poses challenges in its simulation. Numerical models showing convective mixing have been typically conducted on small-scale (Emami-Meybodi et al., 2015), being rare the models able to reproduce this process in a large scale. Despite the coarse spatial resolution Audigane et al. (2007) were able to capture in an approximate way the effects of convective mixing with a reactive transport model of the Sleipner site. Upscaled dissolution by convective mixing have been incorporated into reservoir scale theoretical models (Gasda et al., 2011; MacMinn et al., 2011) and laboratory experiments (MacMinn et al., 2012; MacMinn and Juanes, 2013). Recently, Hidalgo et al. (2013) analyzed the impact of convective mixing on CO_2 gravity plumes without taking into account capillary trapping. Elenius et al. (2015) performed a similar study on a tilted aquifer. These previous studies illustrate that convective dissolution may limit the extent and speed of the gravitational current. Sin (2015) compared analytical studies of plume migration and convection with a large scale model showing chromatographic effects due to differences in gas solubility.

Dissolved CO_2 can precipitate as carbonate minerals in the aquifer, the most stable and safest state of carbon in the subsurface. Although experiences in basaltic rocks show a fast carbon mineralization (Gislason et al., 2014), in saline aquifers this may occur in a much larger time scale (Audigane et al., 2007; Xu et al., 2005) and will not be taken into account in this study.

---

[1] This chapter is based on the scientific article "*Interactions of CO_2 gravity currents, capillarity, dissolution and convective mixing in a syncline-anticline system*", currently under revision in *Water Resources Research* journal.
Sáinz-García, A., Nardi, A., Abarca, E., Grandia, F., 2016.

The efficiency and safety of CO_2 storage in saline aquifers depend on understanding not only each trapping mechanism but the interaction between them. The fate of injected CO_2 in underground storage depends on aquifer characteristics, having the slope of the top aquifer surface and the permeability the strongest influence in a homogeneous aquifer (Gammer et al., 2011). A number of studies has been conducted in dipping open aquifers (Gammer et al., 2011; Gasda et al., 2006; Goater et al., 2013; Hesse et al., 2006; Hidalgo et al., 2013; Ide et al., 2007; MacMinn et al., 2011, 2010). However, only analytical models have analyzed anticline structures in relatively thin aquifers (Espie and Woods, 2014; Woods and Espie, 2012). A complete review of mathematical models of CO_2 storage in deep saline aquifers is provided by Celia et al. (2015).

In this article, a two-phase dynamic numerical model able to capture the effects of processes of a large range of temporal and spatial scales, like capillarity, dissolution and convective mixing, is applied to a syncline-anticline aquifer structure. The interplay between these processes and the aquifer slope is analyzed through different injection locations, with special consideration to the free-phase plume migration and the evolution of trapping mechanism affecting CO_2. The aim is to assess the more suitable injection location for CCS projects in anticline aquifers.

3.2.2 Model Description

The mathematical formulation of two-phase CO_2-brine systems is described in section 2.1 and can be found extensively in the literature (Bear, 1972; Chen et al., 2006; Garcia, 2003; Helmig, 1997). In this study the compositional model of section 2.1.1.1 implemented in the FEM framework COMSOL Multiphysics (Comsol, 2016) with a fully implicit approach has been used to represent such a system.

3.2.2.1 Mathematical model

The compositional model is exhaustively described in section 2.1.1.1. The exact equations solved in this study are presented below for clearness. The mass conservation of a chemical component in a fluid is described in equation (3-1). CO_2-brine systems entail two phases (α): liquid (l) and gas (g); and two components (κ): carbon dioxide (CO_2) and water (w); leading to a 4 equations system.

$$\partial_t(\phi S_\alpha \rho_\alpha m_\alpha^\kappa M^\kappa) = -\nabla \cdot \left(\boldsymbol{q_\alpha} \rho_\alpha m_\alpha^\kappa M^\kappa - \phi S_\alpha \rho_\alpha \boldsymbol{D_\alpha} \cdot \nabla(m_\alpha^\kappa M^\kappa)\right)$$

$$+T_\alpha^\kappa + Q_\alpha^\kappa, \quad \alpha = l, g\,;\, \kappa = CO_2, w \qquad (3\text{-}1)$$

where ϕ is the porosity of the medium $(m^3 \cdot m^{-3})$, S_α is the phase saturation $(m^3 \cdot m^{-3})$, ρ_α is the phase density $(kg \cdot m^{-3})$, m_α^κ is the molality of the κ component in the α phase $(mol \cdot kg^{-1})$, M^κ is the component molar weight $(kg \cdot mol^{-1})$, $\boldsymbol{q_\alpha}$ corresponds to the phase Darcy's flow in its multiphase form $(m^3 \cdot m^{-2} \cdot s^{-1})$, $\boldsymbol{D_\alpha}$ is the phase diffusion/dispersion tensor $(m^2 \cdot s^{-1})$, Q_α^κ is the component mass source term in the α phase $(kg \cdot m^{-3} \cdot s^{-1})$ and T_α^κ is the component interphase mass transfer term $(kg \cdot m^{-3} \cdot s^{-1})$. The last four terms can be extended as:

$$\boldsymbol{q_\alpha} = -\frac{k k_\alpha^r}{\mu_\alpha}(\nabla P_\alpha - \rho_\alpha \boldsymbol{g}) \qquad (3\text{-}2)$$

$$\boldsymbol{D}_\alpha = D_m \boldsymbol{I} + |\boldsymbol{q_\alpha}|\left(\alpha_L \boldsymbol{E}(\boldsymbol{q_\alpha}) + \alpha_T \boldsymbol{E}^\perp(\boldsymbol{q_\alpha})\right) \qquad (3\text{-}3)$$

$$Q_\alpha^\kappa = Q_\alpha M^\kappa m_\alpha^\kappa \qquad (3\text{-}4)$$

$$T_\alpha^\kappa = \phi S_\alpha \rho_\alpha k_{kin}^\kappa (\overline{m}_\alpha^\kappa - m_\alpha^\kappa) M^\kappa \qquad (3\text{-}5)$$

where k is the permeability tensor (m^2), k_α^r is the relative phase permeability $(-)$, μ_α is the phase dynamic viscosity $(Pa \cdot s^{-1})$, P_α is the pressure (Pa) and $\boldsymbol{g}$ is the gravity vector $(m \cdot s^{-2})$, D_m is the molecular diffusion coefficient $(m^2 \cdot s^{-1})$, $\alpha_L$and α_T are, respectively, the longitudinal and transverse dispersivity (m), $|\boldsymbol{q_\alpha}|$ is the Euclidean norm of Darcy's flow, $\boldsymbol{E}(\boldsymbol{q_\alpha})$ is the orthogonal projection along velocity and $\boldsymbol{E}^\perp = \boldsymbol{I} - \boldsymbol{E}(\boldsymbol{q_\alpha})$, Q_α is the phase mass source term $(kg \cdot m^{-3} \cdot s^{-1})$, k_{kin}^κ (s^{-1}) is the interphase mass transfer of component κ and $\overline{m}_\alpha^\kappa$ $(mol \cdot kg^{-1})$ is the solubility limit of component κ in the α phase.

Different linear combinations of equations and state variables can be used to diminish the stiffness of the system (Binning and Celia, 1999; Chavent, 1981; Chen et al., 2000; Chen and Ewing, 1997a). For such operations, the following relations are considered:

$$\textstyle\sum_{\alpha=l,g} S_\alpha = 1 \qquad (3\text{-}6)$$

$$\textstyle\sum_{k=CO_2,w} M^k m_\alpha^k = 1 \qquad (3\text{-}7)$$

$$\textstyle\sum_{\alpha=l,g} T_\alpha^k = 0 \qquad (3\text{-}8)$$

$$\textstyle\sum_{k=CO_2,w} Q_\alpha^k = Q_\alpha \qquad (3\text{-}9)$$

Water miscibility in the gas phase is low, in the order of one per cent (Spycher and Pruess, 2005). Therefore, water dissolution in supercritical CO_2 is negligible, reducing the system of equations (3-1) to three. Instead of the classic approach of summing over components, in which the thermodynamic equilibrium is ensured and the interphase mass transfer term (T_α^κ) cancelled (Lu and Lichtner, 2005; Pruess et al., 1999), a different linear combination of the system of equations (3-1) has been implemented.

The system is formed by three equations:

$$\partial_t\left(\phi S_l \rho_l + \phi S_g \rho_g\right) = -\nabla \cdot \left(\boldsymbol{q_l} \rho_l + \boldsymbol{q_g} \rho_g\right) + Q_g + Q_l \tag{3-10}$$

$$\begin{aligned}&\partial_t\left(\phi S_l \rho_l m_l^{CO_2} M^{CO_2} + \phi S_g \rho_g\right) = \\ &-\nabla \cdot \left(\boldsymbol{q_l} \rho_l m_l^{CO_2} M^{CO_2} + \boldsymbol{q_g} \rho_g - \phi S_l \rho_l \boldsymbol{D_l} \cdot \nabla\left(m_l^{CO_2} M^{CO_2}\right)\right) + Q_l^{CO_2} + Q_g\end{aligned} \tag{3-11}$$

$$\begin{aligned}&\phi S_l \rho_l \partial_t\left(m_l^{CO_2} M^{CO_2}\right) - m_l^{CO_2} M^{CO_2} \partial_t\left(\phi S_g \rho_g\right) = \\ &\qquad -\boldsymbol{q_l} \rho_l \cdot \nabla\left(m_l^{CO_2} M^{CO_2}\right) + m_l^{CO_2} M^{CO_2} \nabla \cdot \left(\boldsymbol{q_g} \rho_g\right) + \nabla \\ &\qquad\qquad \cdot \left(\phi S_l \rho_l \boldsymbol{D_l} \cdot \nabla\left(m_l^{CO_2} M^{CO_2}\right)\right) \\ &\qquad -Q_l\left(m_l^{CO_2} - m_l^{CO_2,*}\right) M^{CO_2} - Q_g m_l^{CO_2} M^{CO_2} + T_l^{CO_2}\end{aligned} \tag{3-12}$$

where $m_l^{CO_2,*}$ is the external CO$_2$ concentration. These equations are derived from:

4. the total mass conservation equation (10) obtained by summing over all equations of system of equations (3-1);
5. an equation for the CO$_2$ mass conservation (3-11) obtained by adding the equations for the CO$_2$ component ($\kappa = CO_2$) in both phases ($\alpha = l, g$);
6. equation (3-12), derived by subtracting equation (3-10) multiplied by $m_l^{CO_2} M^{CO_2}$ from the aqueous CO$_2$ mass conservation (equation (3-1) for $\alpha = l$ and $\kappa = CO_2$).

The independent variables solved are liquid pressure (P_l) in equation (3-10), gas saturation (S_g) in equation (3-11) and dissolved CO$_2$ molality ($m_l^{CO_2}$) in equation (3-12).

The interphase mass transfer ($T_l^{CO_2}$) is estimated as a first order a kinetic rate (equation (13-3)). Lumped mass transfer rates can be calculated through the non-dimensional modified Sherwood number (Sh) without independently estimating the interfacial area (Agaoglu et al., 2015; Imhoff et al., 1994; Miller et al., 1990; Powers et al., 1994, 1992; Zhang and Schwartz, 2000).

$$T_l^{CO_2} = \phi S_l \rho_l k_{kin}^{CO_2}\left(\bar{m}_l^{CO_2} - m_l^{CO_2}\right) M^{CO_2} \quad (3\text{-}13)$$

$$k_{kin}^{CO_2} = Sh \frac{D_m}{d_{50}^2} \quad (3\text{-}14)$$

$$Sh = \alpha Re^{\beta} S_g^{\gamma} \quad (3\text{-}15)$$

where $\bar{m}_l^{CO_2}(p_l, T)$ is the CO$_2$ saturation limit in liquid ($mol \cdot kg^{-1}$) calculated through a solubility model, $k_{kin}^{CO_2}$ is the kinetic mass transfer rate (s^{-1}), d_{50} is the mean size of the reservoir grains (m), Re is the Reynold's number (-) and α, β, γ are dimensionless fitting parameters. This approach allows the consideration of both regasification of dissolved CO$_2$ and dissolution of residual free-phase CO$_2$.

To close the system of equations (3-10) to (3-12), algebraic relations as the retention curve and the hydrodynamic properties of the fluids are defined. Capillary pressure (P_c) (equation 2-1) and relative permeabilities are described following the Brooks and Corey (1964) relations (Table 2-2); where S_α^r is the residual phase saturation (-), S_e the effective liquid saturation (-), P_t is the entry capillary pressure (Pa) and ω is pore size distribution index (-). CO$_2$ is assumed to be trapped by capillarity where saturation is lower than residual saturation.

Fluid properties are calculated following the system implemented by Pruess and Spycher (2007) in TOUGH2. The different thermodynamic relations are described in the given references (Table 3-1). Note that salt molality (m_s^{NaCl}), considered constant in our model, is taken into account in various relations.

Dynamic thermal effects are not included, although a constant thermal gradient has been assumed through the aquifer:

$$T = T_0 + k_T z \quad (3\text{-}16)$$

where T is the temperature, T_0 the temperature at earth surface (K), k_T is the geothermal gradient *($K \cdot m^{-1}$)* and z is the depth respect to surface (m).

Sharp fronts of saturation produce numerical instabilities specially in finite elements (Helmig, 1997). A method based on introducing artificial diffusion in the saturation front has been used to stabilize the system.

Table 3-1. Thermodynamic relations

	Name	Expression	Reference
Gas phase	volume	$V_g = V_g\left(p_g, T, m_l^{CO_2}, m_s^{NaCl}\right)$	(Redlich and Kwong, 1949) with parameters from (Spycher and Pruess, 2005)
	solubility	$\overline{m}_l^{CO_2} = \overline{m}_l^{CO_2}\left(p_g, T, V_g, m_s^{NaCl}\right)$	(Spycher and Pruess, 2005)
	density	$\rho_g = \dfrac{M^{CO_2}}{V_g}$	(Nickalls, 1993)
	viscosity	$\mu_g = \mu_g\left(p_g, T, m_l^{CO_2}, m_s^{NaCl}\right)$	(Altunin and Sakhabetdinov, 1972) referred by (Sovova and Prochazka, 1993)
Liquid phase	density	$\rho_l = \rho_l\left(\rho_b, \rho_{CO_2}\right)$	(Garcia, 2001)
		$\rho_b = \rho_b\left(p_l, T, m_l^{CO_2}, m_s^{NaCl}\right)$	(Haas Jr, 1976)
		$\rho_{CO_2} = \rho_{CO_2}\left(p_l, T, m_l^{CO_2}, m_s^{NaCl}\right)$	(Garcia, 2001)
	viscosity	$\mu_l = \mu_l\left(p_l, T, m_l^{CO_2}, m_s^{NaCl}\right)$	(Phillips et al., 1981)

3.2.2.2 Dome-shaped structure study case

The model consists of a homogeneous two dimensional dome-shaped aquifer where supercritical CO_2 is injected (Figure 3-2). The domain is composed by a syncline attached to an anticline of equal slope and dimensions (200 m wide and 4000 m long). The depth at the bottom of the lateral boundaries is 2.5 km and temperature in the aquifer ranges between 338 and 347 K.

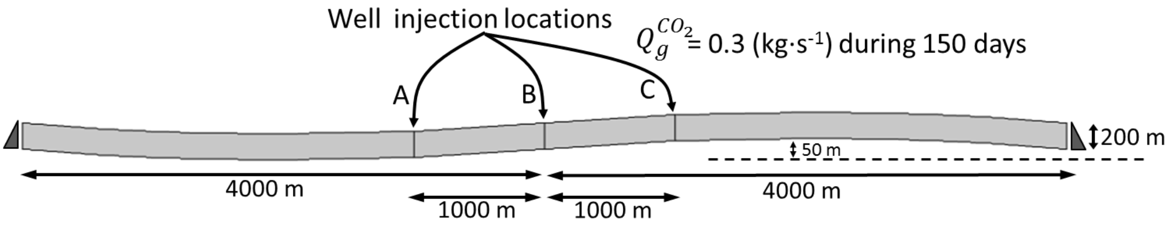

Figure 3-2. Model geometry and boundary conditions. Hydrostatic pressure is assumed at the lateral boundaries, while top and bottom of the aquifer are considered impervious. Three well locations (A, B and C) are considered in the simulations.

Initially the domain is filled by a CO_2-free native brine under hydrostatic pressure conditions. Aquifer top and bottom are assumed to be impervious. No gas flow is allowed in lateral boundaries, which maintains hydrostatic pressure without CO_2 concentration restriction. Supercritical CO_2 is injected in a pulse of 150 days and a rate of 0.3 $kg \cdot s^{-1}$ through a fully penetrating well, leading to a total CO_2 injection of approximately 4.4 tons (slight variations due to different pressure conditions in each well location occur). Different well locations: at the middle of the domain (well B), 1 km to the left (well A) and 1km to the right (well C), are considered to evaluate the influence of the injection location in the trapping mechanisms. Cases injecting each time in a single well has been analysed. The evolution of the CO_2 is simulated for 100 years.

Table 3-2. Model parameters

	Symbol	**Name**	**Value**	**Units**
Aquifer	ϕ	Porosity	0.15	–
	d_{50}	Mean grain size	0.01	m
	T_0	Earth surface temperature	283	K
	k_T	Thermal gradient	$2.5\text{x}10^{-3}$	$\mathrm{K}\cdot\mathrm{m}^{-1}$
	k	Permeability	$1\text{x}10^{-11}$	m^2
	D_m	Molecular diffusivity	$1\text{x}10^{-9}$	$\mathrm{m}^2\cdot\mathrm{s}^{-1}$
	α_L	Longitudinal dispersivity	40	m
	α_T	Transversal dispersivity	8	m
Retention curve	p_t	Entry pressure	$1\text{x}10^{5}$	Pa
	ω	Omega parameter	2	–
	s_l^r	Liquid residual saturation	0.05	–
	s_g^r	Gas residual saturation	0.1	–
Sherwood number	α	Coefficient	1	–
	β	Coefficient	1	–
	γ	Coefficient	2	–
Reynolds number	Re	Reynolds coefficient	$1\text{x}10^{-2}$	–
	ρ_l^{Re}	Characteristic liquid density	1020	kg$\cdot\mathrm{m}^{-3}$
	μ_l^{Re}	Characteristic liquid viscosity	5e-4	$\mathrm{Pa}\ \cdot\mathrm{s}^{-1}$
	v_l^{Re}	Characteristic liquid velocity	5e-7	$\mathrm{m}\ \cdot\mathrm{s}^{-1}$
Fluid	m_s^{NaCl}	Salinity	1	$\mathrm{mol}\cdot\mathrm{kg}^{-1}$

The model has a triangular grid of 267,605 elements with refined areas around the injection well. Different grids were tested to ensure convergence and an estimation of the maximum grid size to capture convective mixing was also considered (Riaz et al., 2006; X. Xu et al., 2006). A homogeneous and isotropic highly permeable aquifer is chosen (Initially the domain is filled by a CO2-free native brine under hydrostatic pressure conditions. Aquifer top and bottom are assumed to be impervious. No gas flow is allowed in lateral boundaries, which maintains hydrostatic pressure without CO2 concentration restriction. Supercritical CO2 is injected in a pulse of 150 days and a rate of 0.3 kg·s-1 through a fully penetrating well, leading to a total CO2 injection of approximately 4.4 tons (slight variations due to different pressure conditions in each well location occur). Different well locations: at the middle of the domain (well B), 1 km to the left (well A) and 1km to the right (well C), are considered to evaluate the influence of the injection location in the trapping mechanisms. Cases injecting each time in a single well has been analysed. The evolution of the CO2 is simulated for 100 years.

Table 3-2). Porosity and retention curve parameters are assumed constant. The characteristic Reynolds number ($Re = v_l^{Re} \rho_l^{Re} d_{50} / \mu_l^{Re}$) was calculated using characteristic values around the CO_2 plume.

3.2.3 Results and Discussion

The model predicts the fate of injected CO_2 along the aquifer. Figure 3-3 illustrates the evolution of both, free-phase (a) and dissolved CO_2 (b) for injection in well B, located in coordinate 4000 m. The pressure increment due to injection promotes the expansion of gas plume towards both sides of the well. After injection stops (0.5 year), bouyancy drives supercritical CO_2 upwards. The free-phase plume (red and yellow in Figure 3-3a) takes 2 years to arrive to the aquifer tip (x = 6000 m). There, the migration stops and CO_2 accumulates below the anticline. As the gravitational current migrates towards the anticline crest some CO_2 remains trapped in the pores by capillarity, leaving a footprint where the supercritical plume has passed through (Figure 3-3a). After 28 years, the free-phase plume has been immobilized and only capillary trapped free-phase CO_2 is present in the aquifer. The variations on the capillary trapped CO_2 after 28 years are due to dissolution. The slight extension of free-phase plume in later times is due to the artificial diffusion and is magnified by the log scale.

Dissolution also contributes to the fixation of CO_2 (Figure 3-3b). Dissolution occurs at the interphase between supercritical CO_2 and the native fluid, around both the mobile free-phase plume and residual CO_2. The fluid density increase due to CO_2 dissolution promotes the onset of convective fingering 5 years after injection. Beside the major accumulation of dissolved CO_2 around the injection well, convection emerges before in the static CO_2 plume below the anticline top than in the mobile plume. The delay of the onset of convection due to gravity current migration was also described by Elenius et al., (2015). Finger-shaped instability leads to convective mixing accelerating dissolution rate and enhancing solute homogenization. At later times, convection shuts down under the anticline crest and dissolved CO_2 sinks following the aquifer bottom. Dissolved CO_2 moves slower than free-phase plume towards the lowest point of the structure, occupying a larger portion of the aquifer than supercritical CO_2. After 100 years, dissolved CO_2 is still advancing.

The displacement of the CO_2 gravity current and the spatial distribution of convective mixing are illustrated by the temporal evolution of the vertical average of non-capillary trapped free-phase and dissolved CO_2 concentrations for the injection in well B (Figure 3-4). The amount of free-phase CO_2 diminishes as it dissolves in the native fluid or is trapped by capillarity. In early times, most of the free phase is located around the injection well (4000 m), but rapidly CO_2 migrates by buoyancy towards the anticline crest where it accumulates. At the end of injection (0.5 years), most of the CO_2 is located between the well and the aquifer tip. During migration, capillarity and solubility trap the CO_2 and splits the free-phase plume into two: most of the free phase accumulates under the anticline crest while a small plume continues existing at the well location. The free phase plume persists around injection location due to the high amount of mobile CO_2 accumulated in the area. At later times, the free phase plume rests at the anticline crest until it disappears completely.

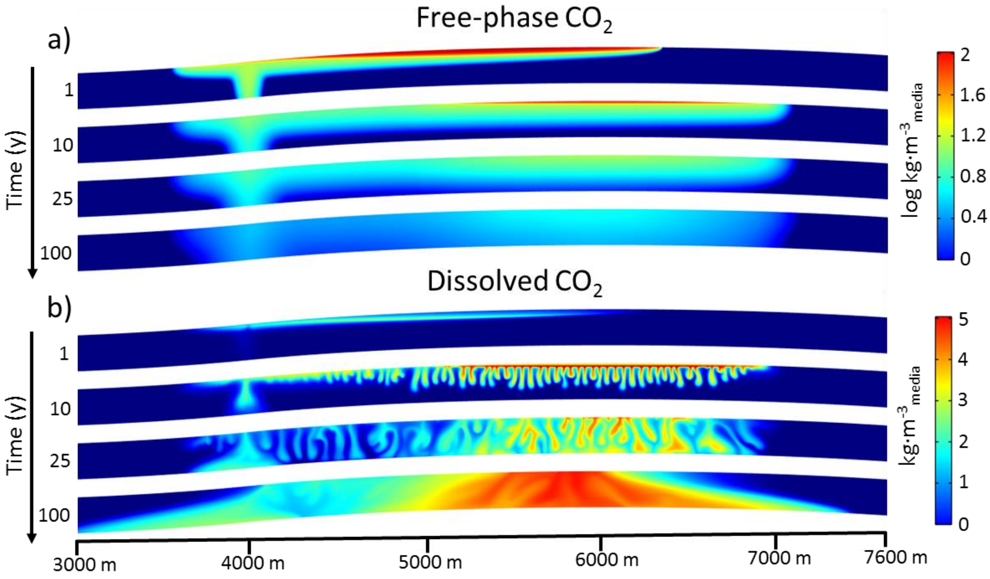

Figure 3-3. Evolution of the CO_2 mass in free-phase (a) and dissolved (b) after 1, 10, 25 and 100 years in a section of the model for injection in well B (located at coordinate 4000). The green colours in (a) correspond to capillary trapped CO_2, while red and yellow are actual mobile free-phase. Note different scales and the log units on (a).

Dissolution takes place beneath the free-phase plume (Figure 3-4b). The effect of convective dissolution is evidenced by the heterogeneous distribution of dissolved CO_2.

At later times gravity fingers become thicker and diminish in number. The delay on the onset of convection due to the plume displacement explains the absence of fingers while the free-phase plume migrates. Capillary trapping retains part of the injected CO_2, explaining the lower scale of dissolved CO_2.

The larger the footprint of the free-phase CO_2 plume, the less safe the injection is. The probability that CO_2 finds a permeable path through the caprock, like faults or abandoned wells, increases with plume migration. Tracking the edges of the free-phase plume over time (Figure 3-1 displays the plume edges), the extension and movement of the plume footprint for the different injection cases can be analyzed (Figure 3-5). The edges delimit the free-phase plume with a vertically averaged CO_2 concentration larger than 2 $kg \cdot m^{-3}$ (see Figure 3-4 for reference). The distance between the leading and trailing edge marks the extension of the plume. Total trapping of mobile CO_2 occurs when the trailing and leading edges coalesce (MacMinn et al., 2010).

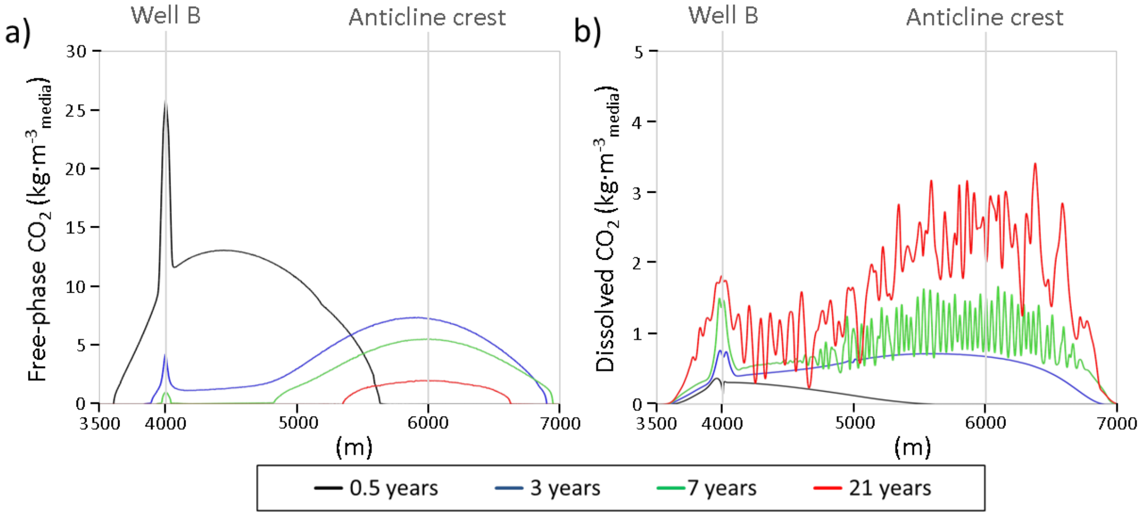

Figure 3-4. Vertically averaged concentration ($\frac{1}{H}\int_0^H C_{CO_2} dz$) of free-phase (a) and dissolved (b) CO_2 for the injection in well B at four simulation times. H is the thickness of the aquifer and C_{CO_2} is the concentration of mobile (not trapped by capillarity) free-phase CO_2 (a) and dissolved CO_2 (b). Injection is located at 4000 m and anticline crest at 6000 m. Note that the vertical scale differs between the two plots.

Plume migration follows similar stages for all cases (Figure 3-5). The CO_2 plume expands towards both sides of the well during injection. After injection stops, the plume halts its downdip spreading and both edges migrate towards the aquifer crest (coordinate 6000); where mobile gas accumulates until it is dissolved or trapped by capillarity. The plume velocity and footprint varies with the aquifer slope. Well B, located in a steeper slope, produces a shorter downdip plume (CO_2 migrates 340 m downdip in comparison with the 590 m of the well C and the 780 of the well A cases). On the contrary, the updip plume spreads more rapidly in the well B injection (7.1 m·d^{-1}, until the plume reach aquifer top) than in well C (6.8 m·d^{-1}) and well A (5.1 m·d^{-1}) (Figure 3-5).

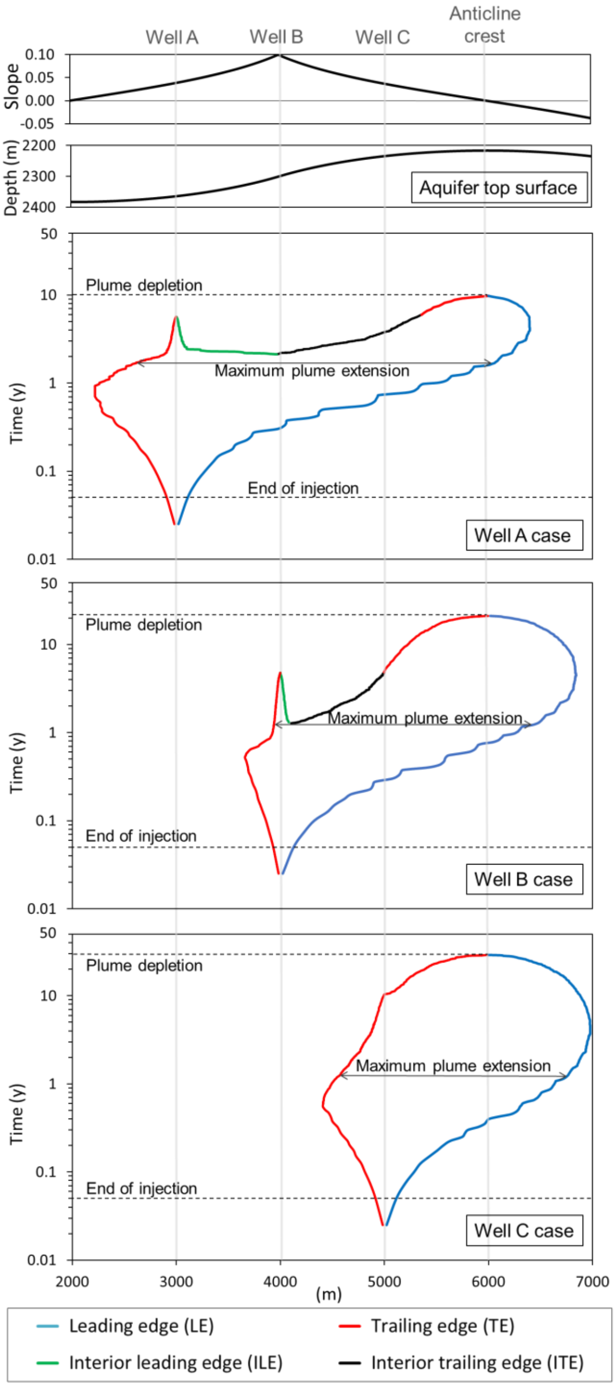

Figure 3-5. Temporal and spatial evolution of the free-phase plume footprint for injection in wells A, B and C. The extension of the gravity current is illustrated with the evolution of the plume edges (see Figure 3-1 for comprehensive meaning). The edges delimit the free-phase plume with vertical CO_2 concentration larger than 2 kg·m^{-3} (Figure 3-4). The slope and depth of the aquifer top surface are illustrated on the top graphs for reference. From the injection point the mobile free-phase plume migrates updip towards the anticline crest. In the cases with injection in well A or B, the plume splits into two. Those cases have two more edges apart from the leading (LE, blue) and trailing (TE, red): the interior leading (ILE, green) and interior trailing (ITE, black) edge. The light oscillations on the LE are numerically generated during concentration integration.

Trailing edges decelerate at injection location (Figure 3-5). The rise of CO_2 accumulated around the well provides CO_2 to maintain the trailing edge at well location. Meanwhile the leading edge keeps advancing increasing the plume extension. In well A and B injection the plume splits (ILE and ITE in Figure 3-5) as a result of the variability on the buoyant CO_2 plume velocity. In those two cases, the maximum plume extension occurs shortly before plume splitting. The plume needs to be fed with a sufficient amount of CO_2 to maintain its thickness. In the area of maximum slope of the aquifer top (i.e., well B location) the plume migrates at its highest speed towards the anticline crest. The amount of free-phase CO_2 arriving to this area is lower than the amount of CO_2 carried updip by the gravity current, thinning the plume and, eventually, causing the plume separation (Figure 3-5 well A and B cases). The CO_2 plume of the well C case migrates in an area with a lower slope and, thus, no plume splitting occurs.

In dome-shaped aquifers, contrary to constant slope injection sites (MacMinn et al., 2011), the maximum migration of CO_2 plumes is not driven by dissolution but by top surface aquifer topography. The free-phase plume stops in the same position for all cases, below the anticline crest (Figure 3-5). The arrival time depends on both the distance between injection and anticline crest and on the gravity current velocity. The closer the injection location to the anticline crest, the earlier the plume arrives. In the well C case, the leading edge of the plume arrives to the coordinate 6000 after 0.4 years, whereas injection in well B, needs 0.77 years and in well A 1.6 years.

Free-phase plume extension below aquifer tip and time of plume depletion depend on the amount of CO2 arriving to the anticline crest and, thus, on the trapping mechanisms affecting the gravitational current. Capillary trapping dominates during plume migration, while solubility is more relevant once the plume stopped on the anticline tip. These two mechanisms continually reduce the fraction of mobile CO2 until its exhaustion. The closer the injection well to the top, the less mass of CO2 is trapped by capillarity and, consequently, the longer the time needed for total immobilization (Figure 3-5).

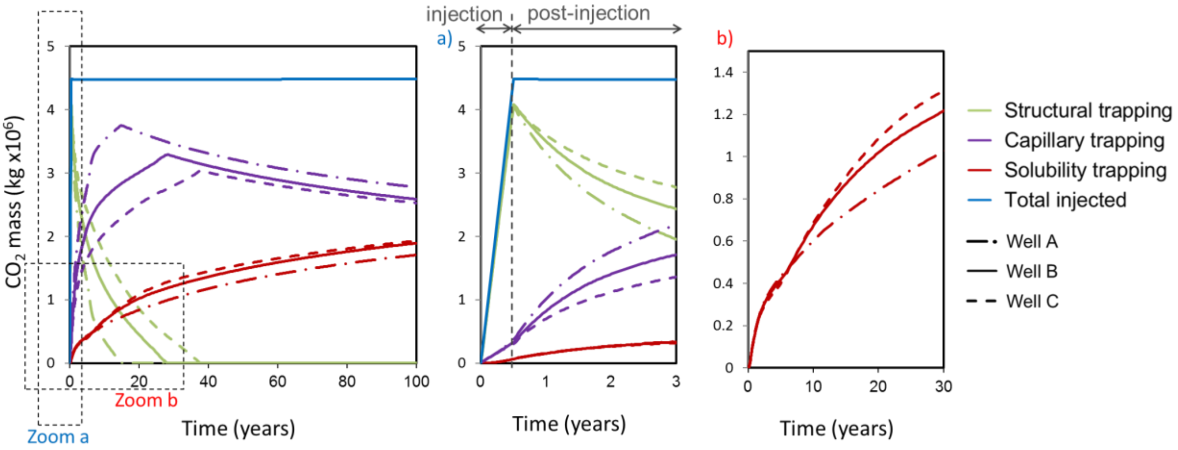

Figure 3-6. Evolution of the CO$_2$ injected with the contributions of different trapping mechanisms: structural, capillary and solubility for injection in wells A, B and C during 100 years. Two zooms of the figure are presented in a) first 3 years and b) 40 years with a smaller vertical scale.

The variations between the three injections on the trapping mechanisms affecting the CO$_2$ are displayed in Figure 3-6. Total amount of injected CO$_2$ is similar and it is preserved in each case. Slight variations in the injected CO$_2$ are due to viscosity and density differences depending on well depth. Initially, the share of solubility and capillarity trapping is minor and their relevance increase with time when replacing structural trapping (Figure 3-6a). During injection, the evolution of the different cases is similar with high free-phase mobile CO$_2$ content. Structurally- trapped CO$_2$ reaches its maximum (more than 90% of the injected CO$_2$) at injection shut-down (Figure 3-6b). After injection, the gravity current migrates towards the anticline crest, enhancing drastically the capillary trapping.

Free-phase depletion time depends mainly on CO$_2$ immobilization by capillarity, being dissolution more relevant at larger times. Capillary trapping is closely linked to the extension and velocity of the free-phase plume. In the well A case, the gravitational current travels a larger distance leading to a faster carbon fixation. Total immobilization takes 15 years in well A case, 28 in well B and 38 in well C (Figure 3-6c). Capillary trapping is strongly influenced by the plume migration velocity. This is evidenced by the acceleration of CO$_2$ fixation after injection stops (Figure 3-6b) and in the deceleration when the free phase plume approximates the anticline crest (Figure 3-6a). The maximum CO$_2$ trapped by capillarity occurs when structural CO$_2$ is exhausted (Figure 3-6a). Thereafter, dissolution of capillary trapped CO$_2$ is the only process taking place. The residual CO$_2$ present in the pore space is physically trapped but not necessarily in thermochemical equilibrium with the surrounding water and may be dissolved.

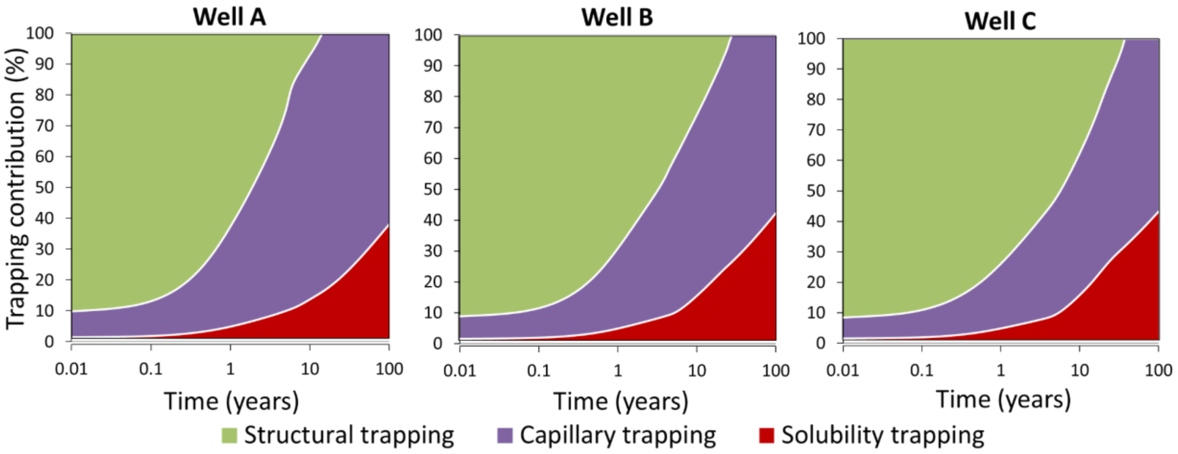

Figure 3-7. Evolution of the share (%) between the trapping mechanisms: structural, capillary and solubility during 100 years for injection in wells A, B and C. Note the log scale in the time axis.

The amount of dissolved CO_2 after 100 years is similar for the three cases, around 1700 tons (Figure 3-6a), but the evolution of the solubility trapping differs. The rate of CO_2 dissolution increases after 5 years due to convective mixing in well A and B cases (Figure 3-6c). The dissolution rate rise is milder and occurs 2 years later in well C case. This delay is explained by the retardation in the onset of convection due to the gravity current migration. Differences in the dissolution rate are due to the length between the injection well and the anticline crest. The longer the path to the anticline crest, the larger the spreading of the CO_2 plume, the smoother the dissolution rate increment and the longer the onset of convection.

Emulating the qualitatively assessment of the storage security depending on the CO_2 trapping from Metz et al. (2005, p., 208, figure 5.9); Figure 3-7 shows quantitatively the time-evolution of the trapping mechanisms share in CO_2 fixation for the analyzed cases. After 100 years, there is no structural trapping and the share between capillary and solubility trapping is comparable; ranging from 62% in well A case, to 58% and 57% in well B and C cases, respectively (Figure 3-7). However, the time evolution of the trapping mechanisms varies depending on the well location. The time of structural trapping exhaustion varies significantly between injection locations as well as the contribution of capillarity and solubility at that moment: well A, B and C cases present 84, 73 and 68% of capillary trapping, respectively.

3.2.4 Concluding remarks

The fate of supercritical CO_2 in an underground anticline-syncline structure is predicted by capturing processes of a wide range of temporal and spatial scales: the migration of the gravity current, the capillary forces, the CO_2 dissolution and the onset and development of convective mixing currents. The numerical model precisely estimates the interaction between different trapping mechanisms involved in carbon storage, providing a valuable tool to assess aquifer storage capacity, efficiency and safety and to aid monitoring during operation.

In dome-shaped aquifers, contrary to open dip aquifers, the extend of CO_2 plumes is not driven by CO_2 dissolution and capillarity (MacMinn et al., 2011) but by the injection well location. The anticline structure halts the gravity current and promotes free-phase CO_2 accumulation beneath the anticline crest, stimulating the onset of convection and, thus, accelerating CO_2 dissolution. In cases with a much larger injection of CO_2 this enhancement may be hindered if free-phase plume thickness become large compared with aquifer width (Espie and Woods, 2014).

The slope of the aquifer and the distance of injection to anticline crest determine the gravity current migration and, thus, the trapping mechanisms affecting the CO_2. Variations on the gravity current velocity due to the anticline slope can lead to plume splitting; while different free-phase plume depletion time is observed depending on the injection location. Injection at large distances from anticline crest presents a longer CO_2 plume footprint and a higher leakage risk than injection close to aquifer tip; however, capillary trapping is greatly enhanced, leading to faster free-phase CO_2 immobilization.

Depending on aquifer characteristics and operation strategy, the selected injection location may vary. If aquifer geochemistry favors a fast mineralization of CO_2, more CO_2 dissolution would be desirable and, therefore, a close to anticline tip would be preferred. In contrast, a distant injection would be more effective within an aquifer with a reliable and well-characterized seal.

3.3 Convective mixing fingers and chemistry interaction in carbon storage[2]

3.3.1 Introduction

Numerous studies have focused on the physical aspects of convection mixing in carbon storage; including the onset of instability and convection, effects of permeability variability, capillarity or aquifers natural flow (Emami-Meybodi et al., 2015; Hassanzadeh et al., 2007; Hidalgo et al., 2012; Hidalgo and Carrera, 2009; MacMinn et al., 2012; Meybodi and Hassanzadeh, 2013; Neufeld et al., 2010; Pau et al., 2010; Rapaka et al., 2008; Riaz et al., 2006; Slim and Ramakrishnan, 2010; Slim, 2014; Szulczewski and Juanes, 2013). However, much less is known about the interaction between convective mixing and geochemical reactions.

Although slow mineral-fluid reactions have little impact on gravitational instability, significant impacts could be expected for fast reactions (Ennis-King and Paterson, 2007). A number of numerical analysis have assessed the effect of second order (Ghesmat et al., 2011) and first order (Andres and Cardoso, 2012, 2011) mineral carbonation reactions on convection in aquifers. Such reactions typically stabilize the system; Andres and Cardoso, (2012, 2011) determined a Damköhler-Rayleigh ratio above which convective mixing is not possible. Such behaviour has been studied in a steady-state regime (Ward et al., 2014), and extended to 1) anisotropic media (Hill and Morad, 2014), 2) a transient nonlinear case (Kim and Choi, 2014) and 3) using a Darcy–Brinkman formulation (Kim and Kim, 2015).

In a previous study, Cardoso and Andres (2014) showed theoretically and experimentally that natural convection can be retarded, or even inhibited, by chemical reactions in silicate-rich aquifers. In contrast, Loodts et al. (2014) found theoretically that the impact of chemical reactions on convection depends on the monotonicity of the density-

---

[2] This chapter is based on the scientific article ”Convective mixing fingers and chemistry interaction in carbon storage”, published in 2017 at the *International Journal of Greenhouse Gas Control 58, 52–61.*
Sáinz-García, A., Abarca, E., Nardi, A., Grandia, F., Oelkers, E., doi:10.1016/j.ijggc.2016.12.005 - Annex III

concentration profile in the system and showed experimentally that convective mixing is enhanced by reaction of dissolved CO_2 with NaOH. These conflicting results emphasize the need to introduce realistic geochemical kinetics to accurately model the temporal evolution of carbon injection sites.

Alteration of the solid matrix due to mineral precipitation and dissolution may vary porosity, thereby altering the flow within an aquifer (Hewitt et al., 2013; Hidalgo et al., 2012). Fu et al. (2015) and Hidalgo et al. (2015) studied such interactions based on a mixing-limited reaction, assuming chemical equilibrium, and found that dissolution occurs in areas of high fluid mixing. Such effects are especially significant at flow stagnation points where the mixing layer is compressed and the transition between fluids with distinct compositions is shorter (Hidalgo et al., 2015).

This study explores numerically the interplay between geochemistry and convective mixing and its effect on CO_2 solubility trapping in a potential industrial CCS project in northern Spain. A pilot CO_2 geological storage project in deep saline aquifer is being coordinated by CIUDEN (CIUDad de la ENergía Foundation). The injection site is located in Hontomín (Burgos, Spain) within a carbonate-hosted aquifer, initially equilibrated with calcite, dolomite and gypsum. Calcite dissolution is assumed to follow a kinetic rate equation, whereas gypsum is assumed to react at local equilibrium. These reactions will alter fluid density, porosity, and permeability, and therefore the fluid flow patterns. This study builds upon similar efforts by Fu et al. (2015) and Hidalgo et al. (2015) by adding a more complex chemical system and showing the degree to which convective mixing can be enhanced by chemical reactions. Most notably, this study illuminates the effect of non-carbonate mineral reactions on CO_2 dissolution in carbon storage. It demonstrates the need for a site specific geochemical assessment of potential CCS sites and the need to take specific account of all potential mineral-fluid reactions that may occur within the subsurface carbon storage system. The influence of Damköhler and Rayleigh numbers is illustrated, allowing the application of computed results to numerous other geologic storage sites.

3.3.2 Model description

3.3.2.1 Physical governing equations

The equations governing the hydrodynamic system are the conservative solute transport and the continuity equation of groundwater flow. The computational model uses the convective form of the solute transport equation (see section 2.2.1 for details), derived from the divergence form of the transport equation by subtracting fluid mass balance multiplied by solute concentration (Galeati and Gambolati, 1989; Goode, 1992; M. W. Saaltink et al., 2004) such that:

$$\omega \frac{\partial \boldsymbol{c}}{\partial t} = -\psi \boldsymbol{q} \nabla \boldsymbol{c} + \nabla \cdot (\psi \boldsymbol{D} \nabla \boldsymbol{c}) - \boldsymbol{c} \nabla \cdot \rho \boldsymbol{D} \nabla \omega^w, \tag{3-17}$$

$$-\nabla \cdot (\rho \boldsymbol{q}) = \rho S_s \frac{\partial p}{\partial t}, \tag{3-18}$$

where $\omega = \phi \rho \omega^w$ and $\psi = \rho \omega^w$, $\boldsymbol{c}$ refers to the concentration vector of all species, ϕ denotes the porosity, ρ represents the liquid density, ω^w stands for the mass fraction of pure water in the liquid, $\boldsymbol{q}$ signifies the Darcy flow vector, $\boldsymbol{D}$ corresponds to the effective diffusion/dispersion tensor, which is assumed to be identical for all aqueous species, and S_s designates the specific pressure storativity. Note that as ***D*** is assumed identical for all aqueous species, charge balance is preserved in the system.

Darcy flow is defined as:

$$\boldsymbol{q} = -\frac{\kappa}{\mu} (\nabla p - \rho \boldsymbol{g}), \tag{3-19}$$

where κ stands for the intrinsic permeability of the medium, μ denotes the dynamic viscosity, p refers to the liquid pressure and $\boldsymbol{g}$ is the gravity acceleration.

The model is coupled in two-ways: chemistry affects fluid flow and hydrodynamics influence chemical reactions. In our system the effect of non-carbon species on fluid density is negligible compared to that of dissolved inorganic carbon (C^T) (Yang and Gu, 2006). Density can be assumed, therefore, to be a linear function of local dissolved carbon concentration (considering considering all of the carbon aqueous species: $CO_2^{(aq)}, HCO_3^- \ and \ CO_3^{-2}$) with an initial density (ρ_0) and a compressibility factor (β) in accord with

$$\rho = \rho_0 + \beta C^T, \tag{3-20}$$

The compressibility factor is based on that reported by Yang and Gu (2006) (Table 3-4) and results in a density difference between a CO_2-free and a CO_2-saturated fluid of 1% in accordance with previous studies (Garcia, 2001). Porosity depends on the mineral volumes of the media in accordance with

$$\phi = 1 - \phi_{inert} - \sum_{i}^{N_m} V_{m,i}\, c_{m,i}\ , \tag{3-21}$$

where ϕ_{inert} stands for the volume fraction of non-reactive minerals, V_m refers to the molar volume of reactive mineral, and c_m denotes the mineral concentration, expressed as moles of mineral per volume of porous medium, of each reactive mineral present in the aquifer. The permeability variation due to carbonate dissolution can be described using a power-law function of the porosity (Civan, 2001). Carroll et al. (2013) showed experimentally that the exponent for homogeneous carbonate rocks is 3 such that

$$\kappa = \kappa_0 (\phi/\phi_0)^3, \tag{3-22}$$

In media were diffusion dominates over dispersion and with relative low tortuosity, effective diffusion can be described using the molecular diffusion coefficient (D_m) times the porosity in accordance with

$$\boldsymbol{D} = D_m \phi, \tag{3-23}$$

3.3.2.2 The chemical system

The chemical composition of the solid matrix and the fluid in the model are based on that of the pilot CCS injection site in Hontomín, Spain. The aquifer is composed of carbonate rocks hosted with a sulfate-rich fluid, in equilibrium with calcite ($CaCO_3$), dolomite ($CaMg(CO_3)_2$) and gypsum ($CaSO_4 \cdot H_2O$), at a temperature of 80 °C (Garcia-Rios et al., 2014). Dolomite is assumed to be unreactive in this model due to its slow dissolution rates kinetics compared to calcite (Pokrovsky et al., 2009). Gypsum rather than anhydrite precipitated in experiments performed with similar fluid composition and temperature (Garcia-Rios et al., 2014) so it has been included in the model.

Table 3-3. Chemistry of the two end-member fluids at 80ºC. Concentration in mmol·kg$_w^{-1}$. Density is given in kg·m^{-3}.

	Density	pH	C	B	Br	Ca	Cl	F	K	Mg	Na	S
Native fluid	1024.5	6.98	0.263	1.465	1.036	53.51	547.1	0.19	14.34	2.623	470.7	24.31
CO_2-rich fluid	1035.9	3.35	652.3	1.465	1.036	53.51	547.1	0.19	14.34	2.623	470.7	24.31

Two end member fluids are considered to mix in the model calculation (Table 3-3): 1) the native formation fluid corresponding to that currently present in the Hontomín formation, CIUDEN *pers. comm., 2011*, and 2) a CO_2-rich fluid obtained by equilibrating this native formation fluid with CO_2 gas at a partial pressure of 50 atm. Thus, the concentrations of all species in these two fluids are identical except for is carbon content and pH. The CO₂-rich fluid has a higher density and lower pH than the native formation fluid. While the native formation fluid is in equilibrium with the rock, the acidic CO₂-rich water will promote carbonate dissolution, increasing the rock permeability and potentially leading to the formation of wormhole-like flow structures (Fredd and Fogler, 1998; Hoefner and Fogler, 1988). Calcite dissolution will increase the aqueous calcium concentration, which will promote gypsum precipitation. These aqueous phase reactions and mineral-fluid reactions are summarized below, together with their equilibrium constant (k for aqueous species) or solubility constant (k_{sp} for the mineral reactions).

$$CO_2^{(aq)} + H_2O \leftrightarrow HCO_3^- + H^+, \qquad \log k = -6.3 \qquad (3\text{-}24)$$

$$HCO_3^- \leftrightarrow CO_3^{-2} + H^+, \qquad \log k = -10.3 \qquad (3\text{-}25)$$

$$CaCO_3 + H^+ \leftrightarrow HCO_3^- + Ca^{2+}, \qquad \log k_{sp} = 1.85 \qquad (3\text{-}26)$$

$$CaSO_4 \cdot 2H_2O \leftrightarrow SO_4^{2-} + Ca^{2+} + 2H_2O, \quad \log k_{sp} = -4.48 \qquad (3\text{-}27)$$

$$H_2O \leftrightarrow OH^- + H^+, \qquad \log k_w = -14 \qquad (3\text{-}28)$$

Thermodynamic data for the phases in reactions (3-24) to (3-28) were taken from the llnl.dat database (Delany and Lundeen, 1990). The activity coefficients are calculated following the B-dot equation (Helgeson, 1969) for all species except for aqueous carbon dioxide which activity is evaluated as a function of ionic strength based on the parameterization of Drummond, (1981).

Gypsum precipitation is relatively fast and is assumed to occur at local equilibrium. In contrast, calcite dissolution has been modelled using the kinetic rate (R) expression provided by Plummer et al. (1978):

$$R = k_r a({}^{m}/_{m_0})^{\omega}(1 - 10^{SI_{calcite}{}^{2/3}}), \qquad (3\text{-}29)$$

where k_r designates a rate constant, a refers to the constant reactive surface area per mol of mineral, $SI_{calcite}$ stands for the saturation index of calcite, ω represents an exponential factor and m and m_0 signify the mass of calcite per cubic meter of media currently and initially. Note that provision for calcite precipitation is not included in the modelled system. Although the Plummer et al. (1978) kinetic rate expression was developed for temperatures between 0-60 ºC and CO_2 pressures of 0-1 atm, more recent calcite dissolution studies (Talman et al., 1990; Zhang et al., 2007) demonstrated its applicability at temperatures to at least 210 ºC. In addition, Pokrovsky et al. (2009) showed that pH is the main driver of calcite dissolution reaction rate in acidic fluids.

3.3.2.3 Dimensionless parameters

To generalize the results of this study, allowing its comparison and application to different scales and conditions, the computational results have been recast as functions of dimensionless parameters. Classically, convection due to gravity instabilities have been characterized using the Rayleigh number (*Ra*), which is the ratio between buoyancy and diffusion forces and given by

$$Ra = \frac{\kappa \Delta\rho \boldsymbol{g} L_z}{\mu D_m \phi}, \tag{3-30}$$

where $\Delta\rho$ refers to the maximum density contrast between the end-member fluids and L_z the characteristic length of the system, in this case the vertical extent of the domain. Systems with a high advective flow compared to diffusion have a high Rayleigh numbers. This will be the case for high permeable aquifers like the Utsira formation in the Sleipner CCS project (Bickle et al., 2007) that would have, for the same conditions as this model, a Rayleigh number of approximately 3700. In contrast, the less permeable layers of the Mount Simon sandstone (Zuo et al., 2012) would have a Rayleigh number of around 70.

The Damköhler number (*Da*) expresses the ratio between reaction and diffusion rates and will be used to characterise the reactivity in the model:

$$Da = \frac{k_r a L_z^2}{D_m \phi}, \tag{3-31}$$

A high Damköhler number indicates a system with high reactivity. Such a system can occur due to fast reactions (e.g., a limestone mostly composed by calcite will have higher *Da* than a dolostone) or to the presence of minerals having a high reactive surface area.

3.3.2.4 Numerical modelling

The numerical model consists of a homogeneous two dimensional domain initially filled with the native formation fluid overlaid by the CO_2-rich fluid (Figure 3-8). The system initially has hydrostatic pressure conditions and no flow is allowed through its boundaries. The presence of a constant, fixed carbon concentration in the top of the domain is assumed, neglecting potential effects of crossflow between the native brine and supercritical CO_2 and resulting volume changes (Emami-Meybodi and Hassanzadeh, 2015; Hidalgo and Carrera, 2009). This assumption can increase the onset of convection time and reduce the rate of CO_2 dissolution. In this study the dissolution rate of supercritical CO_2 into the native formation fluid is assumed sufficiently fast to ensure the presence of a constantly saturated fluid at the native formation fluid/supercritical CO_2 interface. A small fluctuation (standard deviation of 0.003) on the fixed carbon concentration in this top boundary layer was introduced to trigger instability. This small perturbation favours development of convective flow without significantly influencing the computed results (Pau et al., 2010).

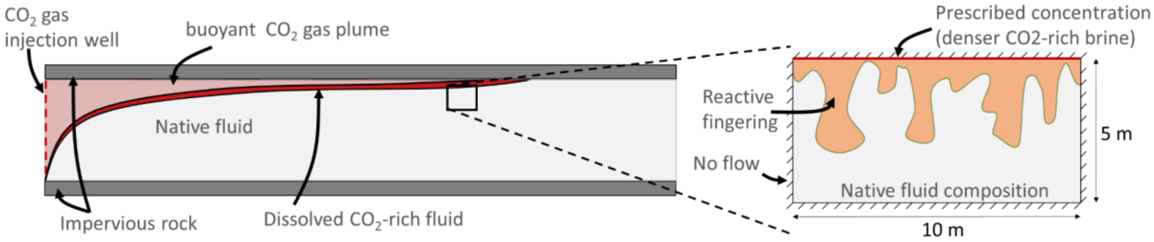

Figure 3-8**.** Schematic illustration of the domain and boundary conditions considered in this study. The migration of supercritical CO_2 as well as its dissolution in the native brine promotes the convective mixing of the fluids.

The physico-chemical parameters of the model correspond closely to that of the Hontomín formation (Garcia-Rios et al., 2014); CIUDEN *pers. comm., 2011* (Table 3-4). The Hontomín aquifer is composed of carbonate rocks. It is assumed that only 5% of the total aquifer volume consists of reactive calcite. Low values of the specific surface area were chosen to evaluate the far from equilibrium evolution of the system and may be consistent with industrial CCS applications due to the discrepancy between theoretical kinetic rates and the rates measured on field sites (Garcia-Rios et al., 2014; Kampman et al., 2014). A set of hydrodynamic and geochemical conditions was simulated for various Rayleigh and Damköhler values as summarized in Table 3-5.

A model domain 10 m length by 5 m depth (see Figure 3-8) was chosen to be large enough to avoid boundary effects in both vertical and horizontal dimensions. A quadratic grid of 32,500 elements with a refinement in the upper layers was used in all simulations, while the total simulation time and the time steps were adapted depending on the velocity of the developed convective fingers. The total simulation time varies from 1 to 6 years and the time step varied from 1×10^5 to 5×10^5 seconds. The spatial and temporal discretization was chosen following stability and accuracy criteria such Peclet and Courant numbers. Furthermore, sensitivity analysis on both time and spatial discretization were performed.

Table 3-4. Model parameters. The calcite dissolution rate equation is taken from Plummer et al. (1978), where $k_1, k_2$and $k_3$are detailed. This equation is already implemented in the llnl database (Delany and Lundeen, 1990). a_{H^+}, $a_{CO_2}$and a_{H_2O} correspond to the activity of protons, aqueous CO_2 and water respectively.

Parameter	Symbol	Value	Units
Dynamic viscosity	μ	$5\text{x}10^{-4}$	Pa·s
Specific storativity	S_s	$1.02\text{x}10^{-8}$	Pa^{-1}
Temperature	T	80	°C
Molecular diffusion coefficient	D_m	$1\text{x}10^{-9}$	$\text{m}^2\cdot\text{s}^{-1}$
Initial porosity	ϕ_0	0.1	-
Initial fluid density	ρ_0	1024.5	$\text{kg}\cdot\text{m}^{-3}$
Compressibility factor	β	17	$\text{kg}\cdot\text{mol}^{-1}$
Volume ratio of inert minerals	ϕ_{inert}	0.85	-
Initial permeability	κ	$8.32\text{x}10^{-14}$ - $1.66\text{x}10^{-13}$ - $3.33\text{x}10^{-13}$	m^2
Specific surface area	a	$7.38\text{x}10^{-3}$ - $3.69\text{x}10^{-5}$ - $7.38\text{x}10^{-8}$	$\text{cm}^2\cdot\text{gr}^{-1}$
Initial amount of calcite	m_0	1.354	$\text{mol}\cdot\text{m}^{-3}{}_{\text{media}}$
Exponent factor	ω	0.6	-
Calcite kinetic constant rate	k_r	$k_1 a_{H^+} + k_2 a_{CO_2} + k_3 a_{H_2O}$	$\text{mol}\cdot\text{cm}^{-2}\cdot\text{s}^{-1}$
	k_1	$8.73\ \text{x}10^{-2}$	-
	k_2	$4.74\ \text{x}10^{-4}$	-
	k_3	$9.58\ \text{x}10^{-7}$	-

The coupling between fluid flow and geochemistry was performed using iCP (interface COMSOL-PHREEQC), a platform for the simulation of complex THCM (Thermo-Hydro-Chemical-Mechanical) problems (Nardi et al., 2014a). It articulates two codes, the geochemical software PHREEQC (Parkhurst and Appelo, 2013) and the multiphysics software COMSOL (Comsol, 2016). The reactive transport equations are solved with a sequential non-iterative approach (SNIA) (Saaltink et al., 2001, 2000; Yeh and Tripathi, 1989). The conservative solute transport is computed in the first step with COMSOL while geochemistry is solved in a second step in PHREEQC. Compared with an iterative scheme, the SNIA does not pose global convergence problems although a tight control on the time step is required to minimize operator-splitting errors (Barry et al., 1996; Carrayrou et al., 2004; Jacques et al., 2006).

Table 3-5. Description of Rayleigh and Damköhler numbers of various model simulations. H= High, M= Medium and L= low.

		Ra		
		3600	1800	900
Da	$1.84x10^{9}$	RaH-DaH	RaM-DaH	RaL-DaH
	$9.21x10^{6}$	RaH-DaM	RaM-DaM	RaL-DaM
	$1.85x10^{4}$	RaH-DaL	RaM-DaL	RaL-DaL

3.3.3 Results

3.3.3.1 Convective mixing

The modelled hydrodynamics is consistent with previous models of subsurface carbon injections (Hidalgo and Carrera, 2009; Kneafsey and Pruess, 2010; Riaz et al., 2006; Slim, 2014). Initially CO_2 penetrates the native formation fluid by diffusion, creating a diffusive boundary layer (Figure 3-9a). With time, the density at this boundary layer increases generating instabilities, triggering convection, and creating fingers (Figure 3-9b,c). These fingers merge to form larger fingers creating a more complex convective flow pattern with denser fingers migrating downwards, while the less dense native formation fluid migrates upwards. When the native formation fluid reaches the upper boundary, the upward flow turns and progresses horizontally, generating new fingers. The horizontal stream of less dense native formation fluid pushes the newly formed fingers until they coalesce with more developed fingers. A narrowing of the well-developed fingers is also observed (Figure 3-9d). Well-developed fingers move rapidly downwards, creating highly concentrated areas that may, eventually, separate from the main body of the finger (Figure 3-9e).

Convective mixing significantly affects the dissolution of supercritical CO_2 into the native fluid. The amount of supercritical CO_2 dissolved can be quantified through the averaged mass flux of dissolved carbon dioxide (CO_2^T) per meter of aquifer lateral extent (Q_{CO_2}) such that

$$Q_{CO_2} = \frac{1}{L} \iint \frac{\partial (CO_2^T \rho \phi \omega^w)}{\partial t} dx\, dy, \tag{3-32}$$

The carbon dioxide dissolution flux curves show the regimes of convection described previously (Figure 3-10). The dissolution of CO_2 initially occurs only by molecular diffusion into the fluid phase (the pure diffusive flux curve is drawn in black in Figure 3-10). When instabilities appear, convective mixing is triggered and the CO_2 dissolution flux increases abruptly. This flux reaches its maximum followed by a minor drop, with same slope as the diffusive flux, due to the merging of small fingers into larger fingers. Finally, the dissolution flux stabilizes at a much higher value than for the pure diffusive process.

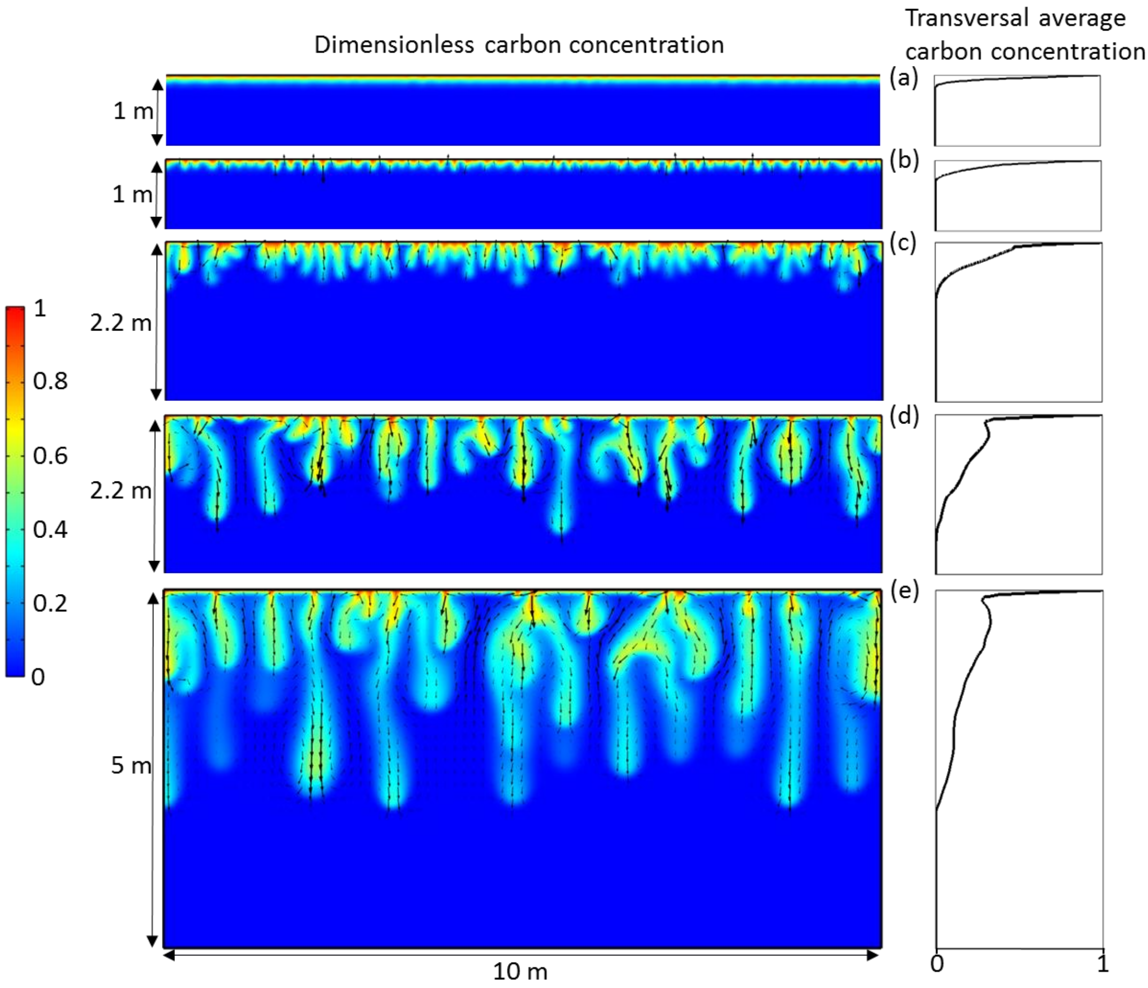

Figure 3-9. Dimensionless carbon concentration (left) and horizontal average carbon concentration profiles (right) for times 0.05(a), 0.1(b), 0.25(c), 0.5(d) and 1(e) years of simulation with Rayleigh = 3600 and Damköhler = 9.21x10^6 (RaH-DaM). Note the arrows illustrate the fluid velocity field. Dimensionless carbon concentration is defined as: $C' = (C^T - C^T_{max})/(C^T_{min} - C^T_{max})$; where C^T_{min} and C^T_{max} represent the minimum and maximum carbon concentration in the simulation

Onset time of convection (t_C) is a term used to quantify the transition point between diffusive to convective flux regime. Different definitions have been used in the literature (Pau et al., 2010; Pruess, 2008). In this study t_C will be defined as the minimum in the CO_2 dissolution flux curve (Hidalgo and Carrera, 2009). The time of convection onset and the CO_2 dissolution fluxes of the simulated cases are grouped by their Rayleigh number (Figure 3-10), showing that dissolution is convection dominated. The higher the *Ra*, the faster the onset time of convection and the higher CO_2 dissolution rate. For simulations having equal *Da* number, the maximum dissolution flux increases linearly with the Rayleigh number. There is also an influence of geochemistry. The higher the reactivity of the system, the higher the CO_2 flux into the fluid phase for same *Ra* number.

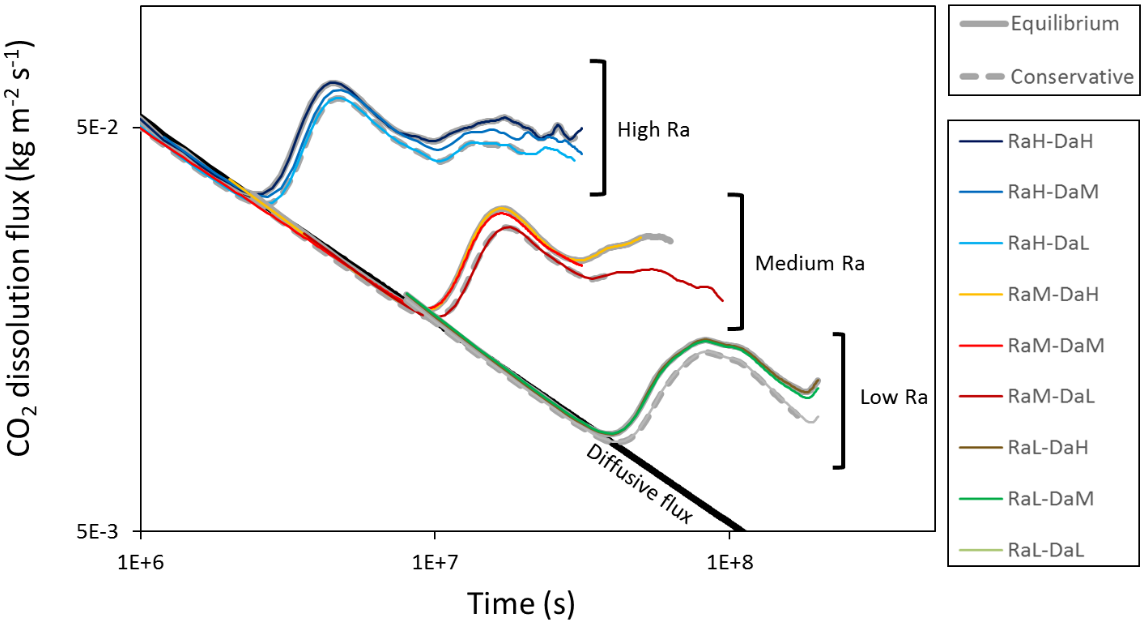

Figure 3-10. Comparison of averaged CO_2 flux per meter of aquifer lateral extent for all simulations and compared to the pure diffusion flux. RaH, RaM and RaL refer to high, medium and low Rayleigh number; DaH, DaM and DaL mean high, medium and low Damköhler number– see Table 3. Conservative refers to simulations without chemical reactions and equilibrium refers to simulations assuming calcite is in equilibrium with the fluid phase. The results of DaH and DaL are similar to the equilibrium and conservative simulations, respectively and in some cases their curves overlap. Both axis are in logarithmic scale.

3.3.3.2 Effects of Chemical Reactions

The acidic CO_2-rich fluid dissolves calcite, triggering chemical processes that alter the distribution of chemical species in the system. Carbon release due to calcite dissolution, leads to a higher concentration of dissolved carbon. In cases where the carbon concentration is close to its saturation limit this could diminish CO_2 dissolution. In contrast, a higher dissolved carbon content generates a higher density gradient between the fluids, promoting enhanced convective mixing. In addition, calcite dissolution releases Ca^{2+} to the fluid leading to the supersaturation and gypsum precipitation, that acts as a Ca^{2+} sink leading to faster calcite dissolution that, in turn, increases porosity and permeability of the aquifer, further enhancing the CO_2 dissolution flux. Gypsum precipitation consumes SO_4^{2-} and water, which modifies the concentration of otherwise conservative species.

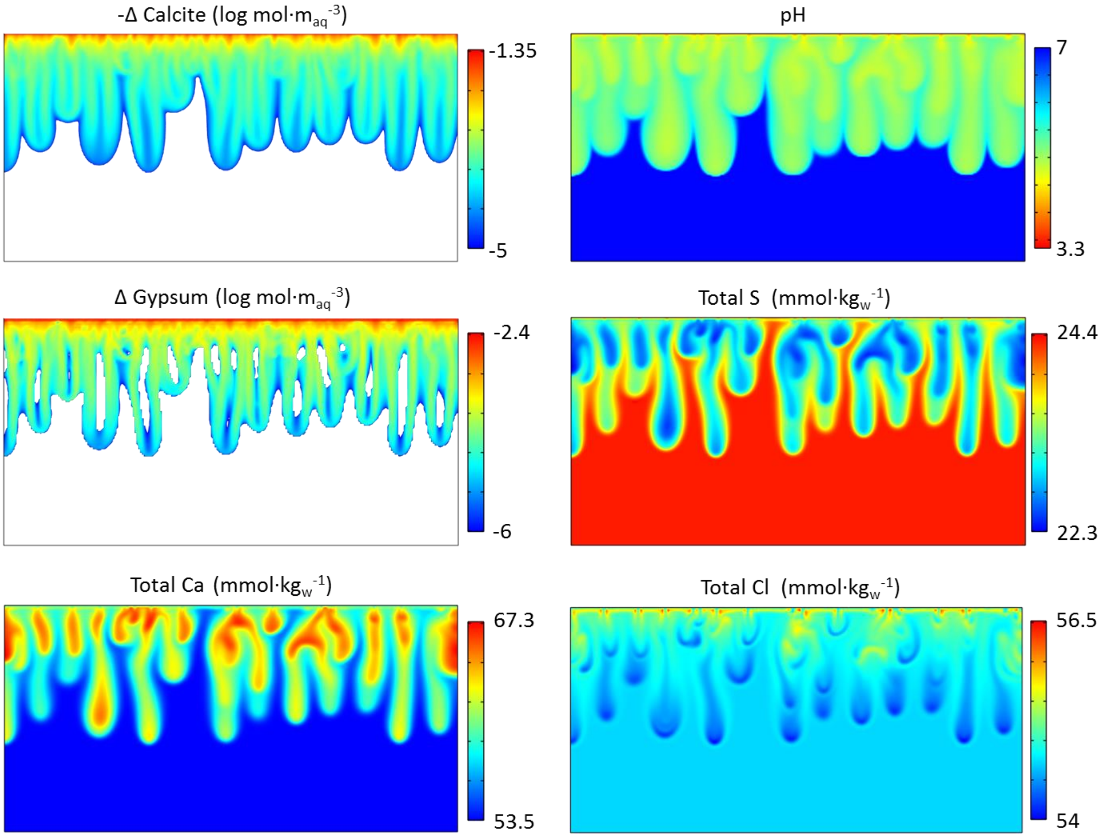

Figure 3-11. Distribution of change in calcite content, change in gypsum content, pH, calcium, sulphur and chlorine for the simulation with Rayleigh = 3600 and Damköhler = 9.21x10^6 (RaH-DaM) after one year. Note the different scales and units. The changes in mineral content is illustrated in log scale, areas with no change in mineral content are shown in white.

Convective mixing affects all reactions producing non-uniform patterns of calcite dissolution and gypsum precipitation, and a heterogeneous distribution of reactive solutes (e.g. Ca and S) and slight variations of non-reactive solute concentrations (e.g., Cl) (Figure 3-11). Calcite dissolution, driven by the pH, occurs mostly in the upper part of the domain. While dissolving, calcite buffers the acidic fingers, limiting the advance of the reactive low pH front. As can be seen in Figure 3-11 and Figure 3-13c, the area where pH is at or below 5 is limited to the upper meter of the domain. The availability of calcite controls the pH of the fingers and, therefore, the calcite content is critical for the development of heterogeneous porosity and persistent flow patterns. The less calcite, the larger the porosity channels will be. In our model, calcite was not exhausted in any point and simulation and only the first stages of porosity channelling pattern are observed (Figure 3-12).

Although porosity increase is most pronounced in the upper layer of the domain, finger shaped dissolution patterns are evident in the lower parts of the aquifer as well (Figure 3-12). Dissolution is concentrated at the finger margins and not at the tip or in the interior, as illustrated by the tip splitting of porosity development in Figure 3-12. This result illustrates the role of fluid mixing in the reactions and is consistent with previous studies (Fu et al., 2015; Hidalgo et al., 2015). Most dissolution occurs where the concentration gradient is perpendicular to the flow direction and not where the flow and the concentration gradient are parallel.

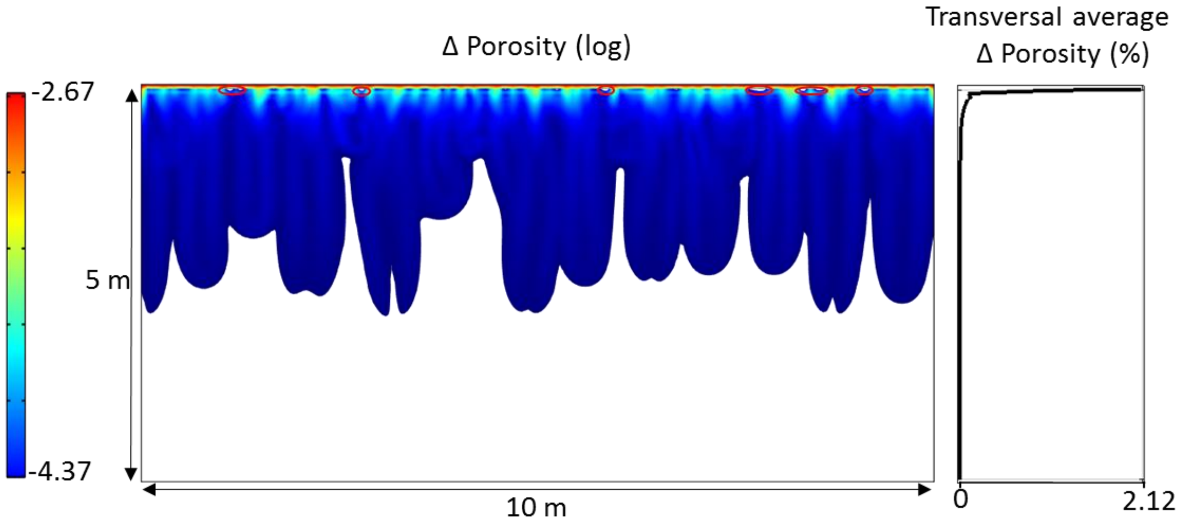

Figure 3-12. Logarithm of porosity increase (left) and horizontal average percentage of porosity variation (right) for the RaH-DaM simulation after one year. Areas with no increase are shown in white. The red circles close to the top indicate areas of porosity loss due to gypsum precipitation.

Porosity development or reduction is driven by aquifer geochemistry. The patterns of porosity changes depend on the aqueous fluid composition, the amount and distribution of reactive minerals, and their reaction rates. The locations of the maximum chemical reaction rates are, however, dominated by fluid mixing and, thus, porosity variations are expected to be observed at similar locations for different geochemical systems.

Note that in this study porosity development is moderated by gypsum precipitation. As the molar volume of gypsum (0.07431 $l \cdot mol^{-1}$) is double that of calcite (0.03693 $l \cdot mol^{-1}$), gypsum precipitation has a significant effect on the porosity and permeability, causing porosity reduction in some parts of the aquifer (Figure 3-12). Similar to calcite dissolution, gypsum precipitation occurs in the areas of higher fluid mixing.

To gain insight into the interaction between geochemistry and convective mixing, the vertical profiles of density variation, porosity, pH and aqueous sulphur after one year of simulation are shown for cases performed using equal high Rayleigh numbers but different calcite reactivities (Figure 3-13). The conservative case (no chemical reactions considered, RaH-Cons) and the case with low Damköhler number (RaH-DaL) yield almost identical results. Likewise, the case with high *Da* (RaH-DaH) has a similar behaviour as that obtained assuming local fluid-calcite equilibrium (RaH-Eq). While the vertical profiles of the medium Damköhler case (RaH-DaM) are located between these two extremes. This trend is evident in the inset of Figure 3-13a, where cases with higher *Da* show a larger finger penetration into the aquifer.

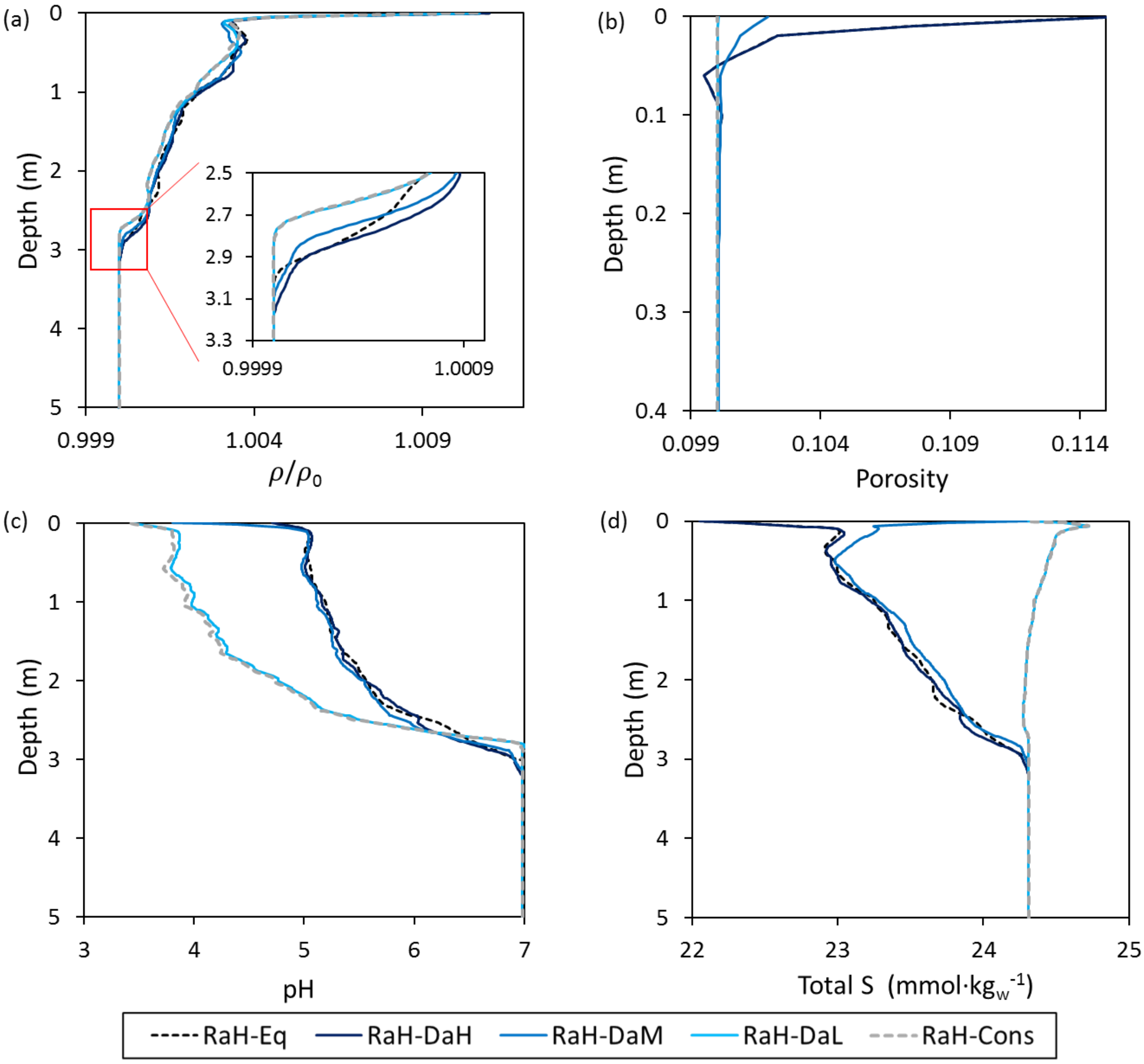

Figure 3-13. Vertical profile of spatially averaged density (a), porosity (b), pH (d) and aqueous sulphur (d) for simulations with equal Rayleigh (3600) and different reactivity: high, medium and low Damköhler numbers (RaH-DaH, RaH-DaM and RaH-DaL), calcite in equilibrium (RaH-Eq) and conservative case (RaH-Cons); after one year of simulation. An inset in a shows a detail of the vertical profiles. Note the different units and vertical scales in b.

To further characterize mineral phase evolution, the average calcite dissolution and gypsum precipitation rates were evaluated over the whole domain. The influence of the Damköhler number on calcite dissolution rates can be seen in Figure 3-14a. Simulations with low *Da* number show almost no dissolution, while simulations performed using a medium *Da* generated rates below 1.8 x10^{-8} (mol·m^{-2}·s^{-1}). High *Da* numbers result in calcite dissolution rates that are twice that of the medium *Da* simulations, except in the case of low Rayleigh number (RaL-DaH) due to the longer times required for the onset of convection in the simulation. Dissolution rates tend to increase with time in all the simulations, although some fluctuations occur after the onset of convective flow (Figure 3-14a). Simulations with high *Da* show an initial drop in the dissolution rate, indicating that calcite dissolution is limited by carbon dioxide diffusion into the aquifer for the cases with higher chemical potential. The influence of convective flow is evidenced by the quantity of calcite dissolution when increasing *Ra* number for an equal chemical potential.

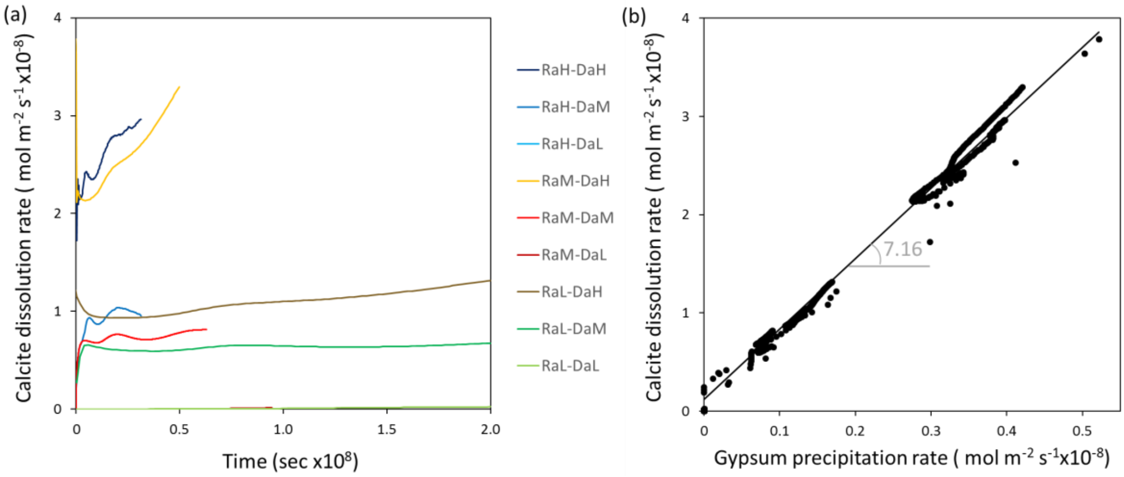

Figure 3-14. Time evolution of calcite dissolution rates (a) and calcite dissolution rates versus gypsum precipitation rates (b) for all simulations. RaH, RaM and RaL refer to high, medium and low Rayleigh numbers; DaH, DaM and DaL stand for high, medium and low Damköhler numbers – see Table 3. Simulations with low *Da* (around 1.85x10^{4}) are difficult to distinguish in (a) due to their small dissolution flux. The slope of the linear regression between calcite dissolution and gypsum precipitation is plotted in (b).

The driving force for gypsum precipitation is the increased Ca^{2+} concentration stemming from calcite dissolution. Gypsum precipitation is, consequently, linearly related to calcite dissolution (Figure 3-14b). Gypsum is in local equilibrium, but the gypsum precipitation rate is one order of magnitude lower than the calcite dissolution rate. Therefore, a net porosity increase is observed.

3.3.3.3 Controlling parameters

Onset time of convection (t_C) shows a clear relation with ~1/*Ra*^{2} (Figure 3-15c). Riaz et al. (2006) demonstrated that t_C scales with $\phi\mu^2 D_m/(\kappa\Delta\rho\boldsymbol{g})^2$. This term can be rewritten in terms of the Rayleigh number (*Ra*) as: $t_C \sim L_z^2/Ra^2 D_m \phi$. Time of convection onset depends, thus, not only on 1/*Ra*^{2}; but also on the characteristic length, porosity and diffusion. This relation is not obvious in Figure 3-15c because in this model *Ra* has been varied without modifying L_z, D_m and ϕ.

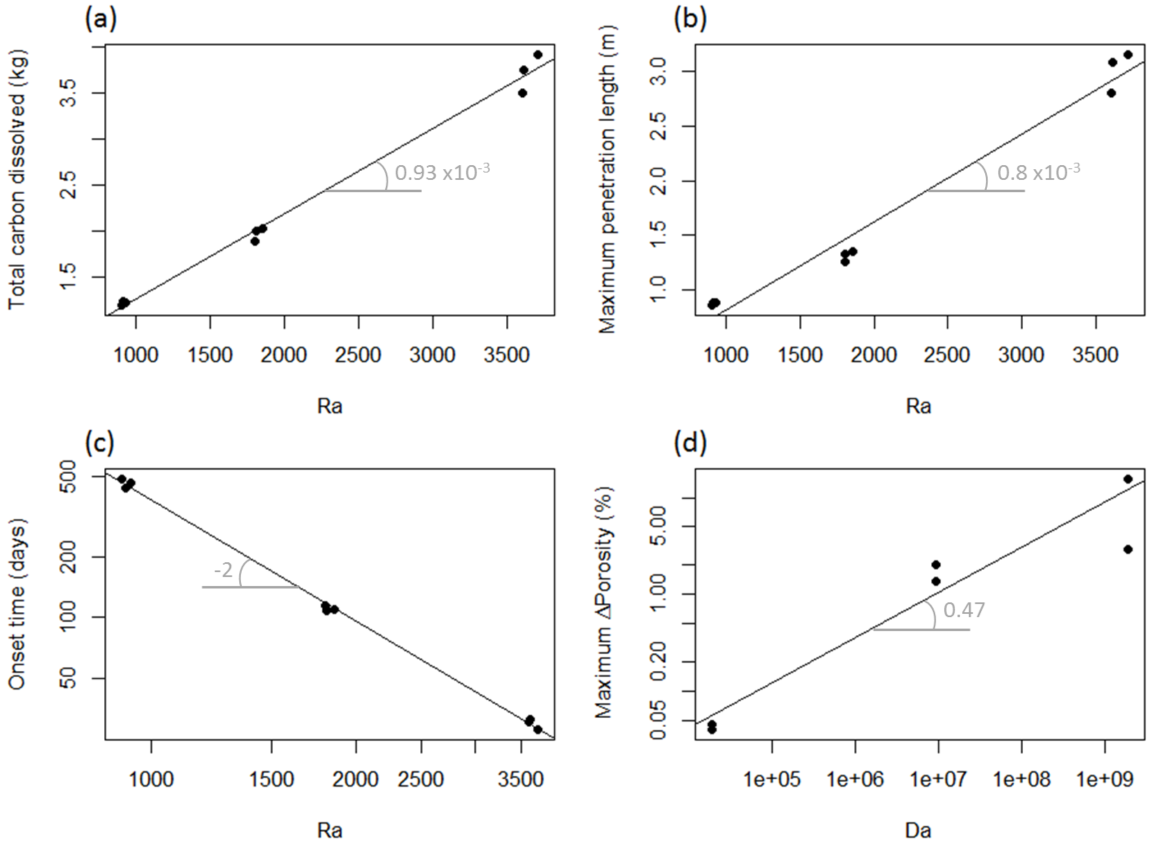

Figure 3-15. Total dissolved carbon (a), maximum downward penetration of fingers (b) and time of convection onset (c) versus Rayleigh number; and maximum porosity development (d) versus Damköhler number for all simulations after one year. In (d) values from simulations with high and medium Da are overlapped. Note the log scales in (c) and (d). The slopes of the linear regression between the axes are plotted in the figures.

The total amount of carbon dissolved and the maximum downward penetration depth of the fingers also illustrate the relevance of the Rayleigh number on the system (Figure 3-15a,b). Both are linearly related to the *Ra* number and little impact of the chemical reactions is observed. However, a system with a higher reactivity (high Damköhler number) accelerates convection, leading to shorter convection onset times, enhanced CO_2 dissolution, and longer fingers.

Porosity development is driven by both physical and chemical processes (Figure 3-15d). Simulations with developed convective mixing after one year (Rayleigh numbers of 1800 and 3600) demonstrate that porosity is controlled by mineral dissolution/precipitation reactions, with similar porosity values for equal *Da* numbers. While simulations with lower *Ra* exhibit a lower porosity development, independently of their *Da*. This can be due to the retardation of the onset of convection. Before convection fluid mixing is low and, therefore, little dissolution occurs.

3.3.4 Conclusions

The interaction between convective flow and geochemistry in a subsurface saline aquifer has been investigated using a coupled reactive transport model. The carbonate aquifer with a high aqueous sulphate content modelled in this study is representative of the natural Hontomín pilot CCS storage site and it is anticipated that the behavior calculated in this study may provide insight into other potential carbon storage aquifers.

As expected, fingering favours CO_2 dissolution, leading to more stable storage and to a safer CO_2 injection. Convective mixing is expected in CCS sites, although the time of onset will vary dramatically with the Rayleigh number of the aquifer. Once started, convective mixing will take place until the aqueous concentration of CO_2 is homogenized throughout the aquifer. This depends on the width of the aquifer. Although the key driving force of convection and, thus of CO_2 dissolution, is the Rayleigh number of the system, it is also influenced by chemical reactions. Contrary to previous studies with a single chemical reaction consuming carbon dioxide (Andres and Cardoso, 2012, 2011; Ghesmat et al., 2011), in the chemical system analysed in this study, the higher the mineral reaction rates, the faster the onset of convection; which in turns leads to higher CO_2 dissolution rates.

Convective mixing leads to a heterogeneous distribution of aqueous species and non-uniform calcite dissolution and gypsum precipitation patterns. The simulations presented above illustrate the role of calcite as a buffer for acidic fluid fronts. Calcite dissolution restricts lower pH fluids to upper layers of the domain, where the majority of porosity development occurs. Besides, the degree of porosity development in the upper layer of the aquifer and at finger boundaries shows the relevance of fluid mixing in chemical reactions. Demonstrating that major reactivity occurs where concentration gradient is perpendicular to the flow direction.

The role of non-carbonate minerals and species on the dissolution of CO_2 is demonstrated to be significant. Although, gypsum precipitation reduces porosity and permeability, it also acts as a Ca^{2+} sink, leading to further calcite dissolution. Thus, gypsum precipitation generally enhances porosity development. This coupling between reactions and fluid flow is not obvious and demonstrate the need for comprehensive flow models that includes a realistic description of the chemical system.

For the aquifer chemical composition of this study, a relatively accurate estimate of the CO_2 dissolution rate could be obtained from the Rayleigh number of the system alone. This, however, depends on the specific conditions of each injection site. Coupled models to study the interaction between fluid flow and geochemistry would be needed to ensure the precision of physical models to accurately represent carbon-dioxide injection into subsurface storage sites.

4 Underground hydrogen storage

4.1 Hydrogen as energy storage from renewables

The reduction of fossil fuel-based energy sources to meet climate protection international agreements (European Commission, 2010; Paris Agreement, 2015) will require an increase on renewable energy production (European Commission, 2012). The contribution of renewable sources to the energy mix has increased significantly in last decades. They have become one of the main electricity sources in some European countries as Spain, Germany and Denmark (European Commission, 2015, 2014). A major disadvantage of these sources is their unsteadiness, which results in an intermittent electricity delivery to the grid. The imbalance between demand and supply generates alternating periods of excess and shortage of energy. Surplus energy can be defined as the energy generated (or potentially available) that is beyond the immediate needs of the electricity grid. It is generally lost, being its storage one of the options to compensate this imbalance (European Commission, 2011; Heide et al., 2011). Storage options at different time scales (hourly, daily and seasonal) are needed. Small decentralized storage technologies can adjust to short-term energy shortage. However, mid to long-term electricity storage is still a challenge. The conversion of surplus energy from renewables to hydrogen (H_2) and its storage is one of the proposed measures to address the long-term storage (Andrews and Shabani, 2012; Heide et al., 2011; Lord, 2009) and numerous power-to-gas pilot plants have been developed in recent years (Gahleitner, 2013).

Hydrogen is a suitable energy vector that can be produced by electrolysis, presents a high energy density and can be used in a wide range of end-use applications such as re-electrification, methanation, and fueling vehicles. Hydrogen has a very small density at standard conditions ($0.089\ kg\cdot m^{-3}$) and prevails in gas phase under a very large range of pressures and temperatures. Geological formations provide the necessary capacity to storage the large volumes of hydrogen required to buffer seasonal demands with a reasonable cost (Carden and Paterson, 1979; Carr et al., 2014; Landinger et al., 2014; Taylor et al., 1986).

4.2 Quantitative assessment of seasonal underground hydrogen storage from surplus energy in Castilla-León (north Spain)[3]

4.2.1 Introduction

Similar to natural gas, two options are preferred for underground hydrogen storage, (1) man-made salt caverns in thick evaporitic formations (Ozarslan, 2012), and (2) deep porous formations such as saline aquifers or depleted oil fields (Evans, 2007; Lord, 2009). Several salt caverns are currently under operation for hydrogen storage (Crotogino and Huebner, 2008; Leighty, 2008; Lord, 2009). The viscoplastic properties of evaporitic rocks ensure the seal and mechanical stability of the salt caverns, making the operation (injection-extraction) flexible and appropriated for medium and even short-term storage. Moreover, the high saline environment prevents the microbial consumption of H_2. However, salt caverns are relatively small, up to few millions of m^3, and are not as widespread as porous formations, at least those formations with sufficient thickness.

Saline aquifers have large potential storage capacity (hundreds of Mm^3) and are distributed worldwide (Orr Jr, 2009). They accumulate the majority of the total natural gas storage in the subsurface (EIA-International Energy Agency, 2016). However, to date, no pure hydrogen storage exists. Four aquifers stored town gas (with a composition of around 50% of H_2 and 50% CH_4): Engelbostel and Bad Lauchstädt in Germany, Lobodice in the Czech Republic and Beynes in France (Kruck et al., 2013; Panfilov et al., 2006). Storage in deep aquifers is the most cost-effective option for underground hydrogen storage (Lord et al., 2014).

These conditions confirm saline aquifers as a promising alternative for seasonal hydrogen storage. However, some questions remain open. The stability and integrity of the overlying seal is a critical, allowing a limited range of fluid pressures in the aquifer and, thus, low flow rates. Other aspect to consider is the reactivity of the hydrogen with

---

[3] This chapter is based on the scientific article "*Assessment of feasible strategies for seasonal underground hydrogen storage in a saline aquifer* ", published in 2017 at the Int. J. Hydrogen Energy.
Sáinz-García, A., Abarca, E., Rubi, V., Grandia, F.
doi:10.1016/j.ijhydene.2017.05.076 - Annex IV

aquifer components. Abiotic reaction with minerals able to consume hydrogen, e.g., sorption onto clays, reduction of Fe^{3+} in Fe-bearing minerals, can be considered negligible (Bardelli et al., 2014; Didier et al., 2012; Mondelli et al., 2015; Truche et al., 2010). Biotic consumption could be of concern under some conditions. Methanogenic, acetogenic and sulphate-reducing bacteria can use hydrogen as electron donor (Ebigbo et al., 2013; Panfilov, 2016, 2010; Toleukhanov et al., 2012). The low hydrogen solubility restricts consumption to the gas/liquid interface (Hagemann et al., 2015), minimizing the effect of biotic consumption when large volumes of hydrogen is stored.

The hydrogen low density and viscosity result in a high hydrogen mobility that can lead to hydrogen losses due to large displacements and, eventually, to viscous fingering (Paterson, 1983). The assessment of the hydrogen footprint and its recovery ratio are the main challenges in aquifer storage. Recently, the dynamics of hydrogen gas in porous media has been investigated by means of multiphase numerical models. Hagemann et al. (Hagemann et al., 2015) studied the formation of viscous fingering in a 2D domain. This study was extended by Feldmann et al. (Feldmann et al., 2016) to a 3D domain where the gas mixing processes was analyzed. These models show that low injection-extraction rate would limit hydrogen mixing in underground storage. An existing 3D anticline structure was modeled to study the effect of aquifer heterogeneity on the storage operation (Pfeiffer et al., 2017) and to assess geophysical monitoring methods for hydrogen gas detection (Pfeiffer et al., 2016). The influence of different well configurations has, however, not been yet investigated.

This study is an appraisal of the feasibility for an underground storage of hydrogen produced from surplus energy from wind power generation in Castilla-León region (northern Spain). Hydrogen conversion and storage is more favourable in areas with potential geological storage near high renewable electricity production. In Spain this combination can be found, among others, in Castilla-León (the region with highest wind power production in the country) (AEE-Spanish Wind Energy Association, 2016), where a number of saline aquifers with suitable seal formations have been described in the frame of previous carbon storage projects (Martinez et al., 2009; Zapatero-Rodriguez et al., 2009). In this article, current data from power generation in the region and an actual dome-shape aquifer will be analysed, by means of a 3D multiphase numerical model. The dynamics of seasonal hydrogen injection-production cycles during 3 years are explored for three different extraction well configurations, paying especial attention to the amount of hydrogen recovered.

4.2.2 Problem definition

4.2.2.1 Annual surplus wind energy for hydrogen storage

Wind power has been the fastest growing renewable energy in Spain during the last decade. It has increased from 2 GW in 2000 to 23 GW in 2015, becoming the 5th country in national wind production in the world (AEE-Spanish Wind Energy Association, 2016). In 2015, it supplied 47700 GWh; contributing a 20% to the electricity mix and growing into the third energy source in Spain. Continuous growth of wind power is foreseen for the next future. Additional 6.4 GW are planned to be installed before 2020 (Apecyl, 2016). The Castilla-León region is leading wind power generation in Spain with 230 wind farms and a total power of 5550 MW, which represents 24% of the national production (Junta de Castilla-Leon, 2015).

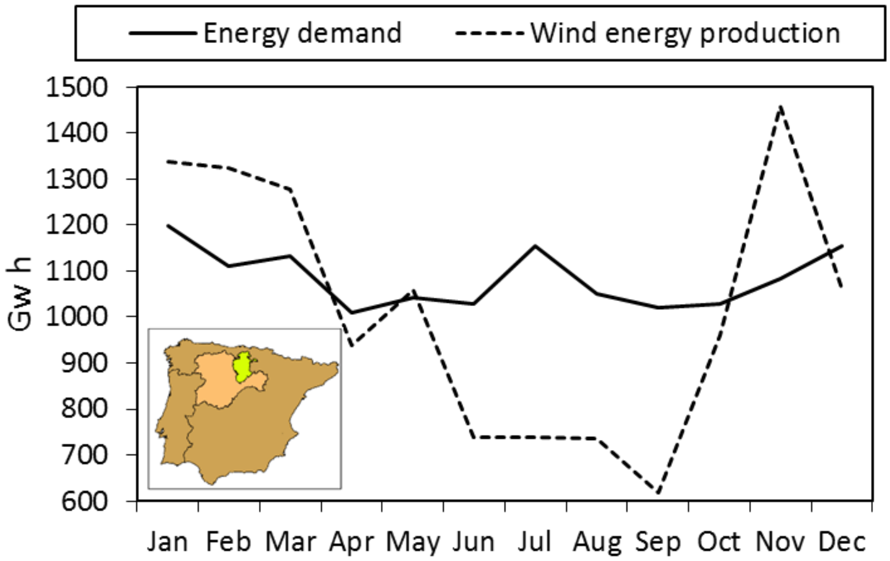

Figure 4-1. Average electricity demand and wind energy production in Castilla-León annual evolution in the period between 2013 and 2015. Data from REE-Red Electrica de España (2016). The location map shows Castilla-León region (brown) and the Burgos province (green).

In Castilla-León, energy consumption is quite constant along the year, whereas wind power production is higher in fall and winter seasons due to more favorable wind conditions (Figure 4-1). Generally, wind electricity production excesses the demand from October to May, while extra energy is needed in summer. Other energy sources and electricity transferences between regions have been used to balance the energy generation-demand. In this work, we analyze the feasibility of storing the theoretical surplus energy as hydrogen during the months from October to May and its recovery between June and September. Predicting surplus energy on wind farms is rather complex because it depends on many factors such as meteorology, energy consumption, market variation, wind farm operation and maintenance. Best estimates indicate that it could range between 1 and 7% of the total electricity production (CENER. National Center of Renewable Energy, 2013; REE-Red Electrica de España, 2011).

Between 2013 and 2015, the average wind power produced in Castilla-León from October to May has been 9415 GWh (REE-Red Electrica de España, 2016). Assuming a 4% of surplus energy, the estimated energy loss is 377 GWh. This represents 16% of the annual consumption and 51% of the summer consumption of Burgos, the second most populated city in the region with more than 175.000 inhabitants (Junta de Castilla-Leon, 2015). Assuming that all this energy is converted to hydrogen using a PEM (Polymer electrolyte membrane) with a rate of 52 kWh per kg of hydrogen (Bertuccioli et al., 2014), the annual mass of hydrogen that can be stored is 7242 tons.

4.2.2.2 Storage structure: the San Pedro Belt

Underground storage formations should ensure the confinement of the injected fluid. A well-characterized impervious overlaying seal is needed to prevent the upward migration of the gas. In addition, the target aquifer should have sufficient capacity and a high permeability to allow the migration of the injected gas and pressure dissipation. Due to the high mobility of hydrogen, the storage must be located in suitable tectonic trap with a steeply dipping structure such as domes; allowing the recovery of high quality H_2 (Sainz-Garcia et al., 2016). In Spain, several potential storage aquifers can be found in Tertiary sedimentary basins as the Duero, Ebro and Guadalquivir basins (Figure 4-2a) (Zapatero-Rodriguez et al., 2009).

In particular, in the Duero basin a number of favorable structures for gas storage has been recognized and studied in the frame of carbon storage projects (Martinez et al., 2009; Zapatero-Rodriguez et al., 2009). They are located in the NW margin of the basin, close to the boundary with the Basque-Cantabrian basin Figure 4-2a). It can be considered the foreland basin of the Cantabrian orogenic range (Barnolas and Pujalte, 2004). It shows very mild deformation in the central and south area; while, thick-skinned tectonic structures occurred in the NW margin, leading to two fold belts called

Montorio-Ubierna and San Pedro. These belts include thrust faults of high angle trending NW to SE, and dome-shaped structures between them. Interestingly, these thrust faults are fossilized by the latest Tertiary sedimentation, preventing any direct flow path towards the surface. These domes are of great interest for gas storage. In this work, a dome in the San Pedro belt has been considered as candidate for hydrogen storage (Figure 4-2a).

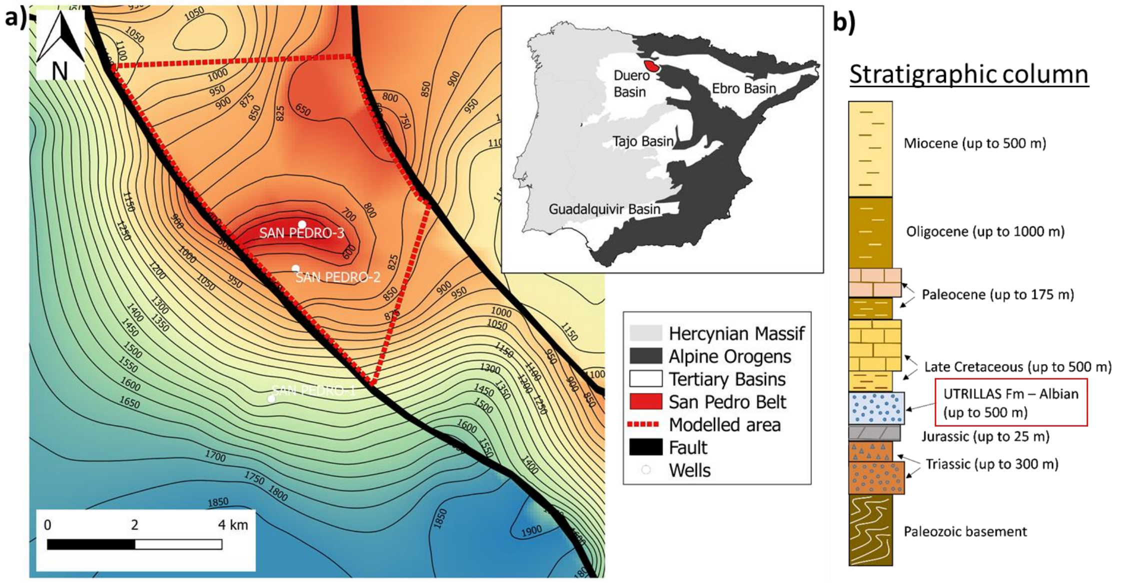

Figure 4-2. a) Top surface of the Utrillas formation, extension of the Spanish Tertiary sedimentary basins, location of the San Pedro belt (red), drilled core (white) and limits of the numerical model. b) Stratigraphy of the NE margin of the Duero basin. The Utrillas sandstone formation is the target aquifer for hydrogen storage. Thicknesses of Tertiary cover in the thrust belts are largely decreased. Data extracted from Leon et al. (Leon et al., 2010).

The lithoestratigraphic record of the dome (Motis et al., 2012) has been reported from seismic and drill core investigations (San Pedro 1, 2 and 3 wells in Figure 4-2). The Utrillas formation that covers the Triassic-Jurassic rocks is the target formation for gas storage. It is hosted by quartz-rich Albian sandstones, with high permeability ($1\text{x}10^{-13}\ m^2$), high salinities (> 50,000 ppm of total dissolved solids) and thickness up to 350 m in the top of the dome (Figure 4-2b). The porosity of the Utrillas sandstones ranges between 13 to 20 %. The Utrillas formation is covered by low permeable rocks of Late Cretaceous age that ensure the isolation of the stored gas. The storage-seal system is overlaid by a number of sedimentary facies deposited until the Neogene with a total thickness over 1700 m (Figure 4-2b). However, in the San Pedro dome the Tertiary sequence is much thinner, being the top of the dome at 500 m depth.

4.2.3 Mathematical Model

The mathematical description of two-phase flow systems can be found extensively in the literature (Bear et al., 1991; Helmig, 1997; X. Xu et al., 2006). In this study, the hydrogen-water system is reproduced by a finite element approximation with a fully implicit approach implemented in COMSOL Multiphysics (Comsol, 2016). Due to the low solubility of hydrogen in water (Kolev, 2007), especially for the time scales of underground hydrogen storage, an immiscible model has been used.

4.2.3.1 Governing equations

The mass conservation (equation 4-1) of two phases (α): liquid (l) and gas (g) results in a system of two equations.

$$\partial_t(\phi\rho_\alpha S_\alpha) + \nabla\cdot(\rho_\alpha \boldsymbol{q_\alpha}) - Q_\alpha^0 = 0\,, \qquad \alpha = l, g \tag{4-1}$$

where ϕ is the porosity of the medium ($m^3 \cdot m^{-3}$), S_α is the phase saturation ($m^3 \cdot m^{-3}$), ρ_α is the phase density ($kg \cdot m^{-3}$), $\boldsymbol{q_\alpha}$ corresponds to the Darcy's flow in its multiphase form ($m^3 \cdot s^{-1} \cdot m^{-2}$) and Q_α^0 is the phase mass source term ($kg \cdot s^{-1}$). The Darcy´s flow for two-phase systems can be extended as:

$$\boldsymbol{q_\alpha} = -\frac{kk_\alpha^r}{\mu_\alpha}(\nabla P_\alpha - \rho_\alpha \boldsymbol{g}) \tag{4-2}$$

where k is the permeability tensor (m^2), k_α^r is the relative phase permeability (-), μ_α is the phase dynamic viscosity ($Pa \cdot s^{-1}$), P_α is the pressure (Pa) and $\boldsymbol{g}$ is the gravity vector ($m \cdot s^{-2}$).

In order to reduce the system stiffness, different linear combinations and state variables can be chosen (Binning and Celia, 1999; Chavent, 1981; Chen et al., 2000) assuming that $\sum_{\alpha=l,g} S_\alpha = 1$. In this study, the so-called coupled pressure-saturation formulation (section 2.1.1.2) has been implemented. The system of two equations is formed by the gas mass conservation equation and the total mass conservation equation. The gas mass conservation equation (equation 4-3) results from equation (4-1) solved for the gas phase with gas saturation (S_g) as independent variable. The total mass conservation (equation 4-4) is obtained by summing both phase equations in equation (4-1) with liquid pressure (P_l) as state variable.

$$\partial_t\left(\phi\rho_g S_g\right) + \nabla\cdot\left(\rho_g \boldsymbol{q_g}\right) - Q_g^0 = 0 \tag{4-3}$$

$$\sum_{\alpha=l,g}\left(\partial_t(\phi\rho_\alpha S_\alpha)+\nabla\cdot(\rho_\alpha \boldsymbol{q_\alpha})-Q_\alpha^0\right)=0 \tag{4-4}$$

Algebraic relations as the retention curve and the hydrodynamic properties of the fluids are defined to close the system. Capillary pressure (equation 2-1) and relative permeabilities are described following the Brooks and Corey (Brooks and Corey, 1964) relations (Table 2-2) where S_e is the effective saturation (-), S_l^r is the residual liquid saturation (-), S_g^r is the residual gas saturation (-), ω is the pores size distribution index (-) and P_t is the entry pressure (Pa).

Gas density is evaluated following the Peng-Robinson equation of state (Robinson and Peng, 1978). Gas viscosity and water hydrodynamic properties depend on aquifer temperature and are calculated with the built-in COMSOL state equations (Comsol, 2016). A constant thermal gradient has been assumed through the aquifer**:**

$$T=T_0+k_T z \tag{4-5}$$

where T is temperature (K), T_0 the temperature at earth surface (K), k_T is the geothermal gradient *($K\cdot m^{-1}$)* and z is the depth respect to surface (m).

4.2.3.2 Numerical implementation

The Utrillas formation in the San Pedro dome (Figure 4-2) is represented with a 3D numerical model. Data from the ALGECO2 project (Leon et al., 2010) is used to define the aquifer geometry and parameters (Table 4-1). However, no site-specific data of capillary pressure and relative permeability are available and typical literature values are used (Bachu and Bennion, 2008; Hildenbrand et al., 2004, 2002). The model domain is discretized in more than 270,000 tetrahedral elements. The upper part of the dome, where gas is expected to migrate, has a refined grid (Figure 4-3). The top and bottom boundaries are considered impervious as well as the east and west limits, where sealed thrust faults act as flow barriers. A Dirichlet condition with prescribed hydrostatic liquid pressure and $S_g = 0$ is imposed in the north and southeast boundaries where the Utrillas formation has continuity (Figure 4-3). Before injection, the aquifer is considered filled by water under hydrostatic conditions.

Initially, 7492 tons of H_2 are injected during one year as cushion gas. Although cheaper gases like nitrogen could be used; gas mixing would lower the quality of the recovered gas (Pfeiffer et al., 2017). Impurities should be removed from the withdrawn gas, increasing the cost of above ground facilities. The injection is distributed along a vertical

40 m-long well located at the top of the dome (Figure 4-4). The well is opened below the impervious caprock, 500 m below the ground surface. A volumetric flux of hydrogen in the well (0.085 $m^3 \cdot s^{-1}$) is imposed as a gas source. The mass of H_2 injected varies depending on the gas density, which is function of the temperature and pressure of the aquifer. This leads to an injection of approximately 0.24 $kg \cdot s^{-1}$ (230,000 $sm^3 \cdot d^{-1}$).

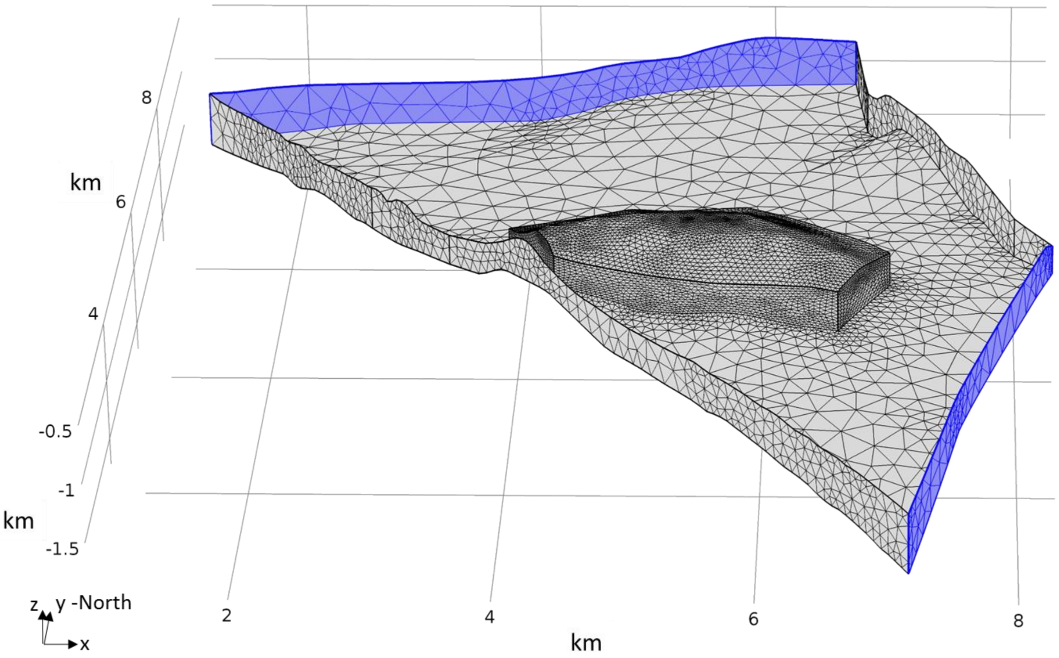

Figure 4-3. Spatial discretization of the modelled 3D structure. A refined tetrahedral grid is used in the axial part of the dome. Results are plotted focusing in this refined area. Blue limits indicate where Dirichlet conditions are imposed.

Three years of operation are simulated after the injection of the cushion gas. Hydrogen is injected during 243 days (from October to May) and extracted during 122 days (from June to September). Hydrogen is injected continuously through the same well as the cushion gas, but increasing the hydrogen flux to 0.15 $m^3 \cdot s^{-1}$ (approximately 0.345 $kg \cdot s^{-1}$ or 335,000 $sm^3 \cdot d^{-1}$). Gas flux increases linearly during the first 10 days of injection, to prevent a steep pressure rise at the aquifer. The pressure threshold to prevent gas flow through the aquifer seal is site-dependent and has to be further analyzed for the San Pedro dome. In this study aquifer pressure is preserved between 3 and 8 MPa. Injection is stopped when the injected H_2 mass reaches the estimated annual mass of hydrogen produced in Castilla-León (7242 tons). Due to gas density variations, the end of injection occurred at different times each year. The injection is stopped for the remaining year until production began again.

In practice, extraction is controlled by maintaining a constant pressure in the well and, a priori, the proportion of gas and liquid extracted is unknown. To implement the extraction in the numerical model, a mixed-type (Cauchy) boundary condition was imposed. This boundary condition specifies that the mass flow at the well (Q_α^0 in $\mathrm{kg} \cdot \mathrm{s}^{-1}$) is proportional to the pressure difference between the calculated pressure (P_α) and a prescribed external gas pressure (P_{well}). The phase-dependent condition can be extracted from the form of Darcy flow taking into account the density and mobility of each phase:

$$Q_\alpha^0 = -\frac{k_{well} k_\alpha^r}{\mu_\alpha} \rho_\alpha (P_\alpha - P_{well}) \quad (4\text{-}6)$$

where k_{well} is the well coating permeability (m^2).

Similar to injection, the extraction increased linearly during the first 10 days and decreased progressively the last 5. The production period lasts 122 days unless extraction is stopped due to high proportion of liquid withdrawal. The extraction is automatically shut-down if the calculated gas saturation at the well is below 0.4.

Table 4-1. Model parameters.

	Parameter	Symbol	Value	Unit
Aquifer	Porosity*	ϕ	0.2	-
	Permeability*	k	$1\text{x}10^{-13}$	m^2
	Earth surface temperature	T_0	298	K
	Thermal gradient	k_T	0.027	$K \cdot m^{-1}$
Retention curve	Entry Pressure	P_t	$1\text{x}10^5$	Pa
	Pore index	ω	2	-
	Residual liquid saturation	S_l^r	0.3	-
	Residual gas saturation	S_g^r	0	-
Extraction boundary condition	Well liquid pressure	P_{well}	$3\text{x}10^6$	Pa
	Well permeability	k_{well}	$1\text{x}10^{-13}$	m^2

* Data taken from the ALGECO2 project (Leon et al., 2010).

Three different configurations of extraction wells have been analyzed (Figure 4-4):

- case A with a horizontal extraction well of 40 m long located 60 m south from the injection well and 10 m below the caprock;
- case B where the extraction takes place at the injection well;
- and case C with two wells of 20 m located 60 m south and 150 m east and west respectively from the injection well.

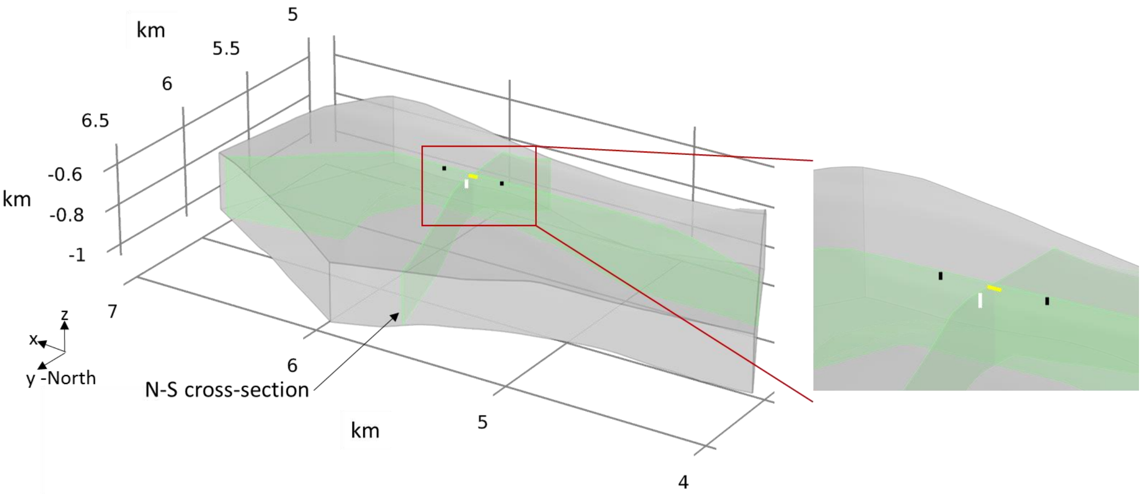

Figure 4-4. Utrillas formation at the axial area of the San Pedro dome and wells' location: Injection well and extraction well in case B well (white), horizontal extraction well in case A (yellow) and short vertical extraction wells in case C (black). The N-S cross-section is displayed in Figure 4-5.

4.2.4 Results and discussion

The maximum gas saturation (0.7 due to the residual liquid saturation) takes place around the well and in the upper part of the aquifer (Figure 4-5). The density contrast between H_2 and water promotes the upward migration of the gas towards the top surface of the aquifer where gas accumulates. Hydrogen spreads along surfaces with equal elevation, while the steep slopes of the dome prevent its dispersion. Simultaneously, pressure variations due to well operation prompt gas plume enlargement or contraction. During injection (Figure 4-5a), fluid pressure increases around the injection well and H_2 expands in all directions, including underneath the injection well. Where the dome steeply dipping borders are closer to the well, the injection pressure leads to a larger H_2 downward reach. In case A, gas plume is approximately 20 m thicker at north side of the section in Figure 4-5 than in the south side.

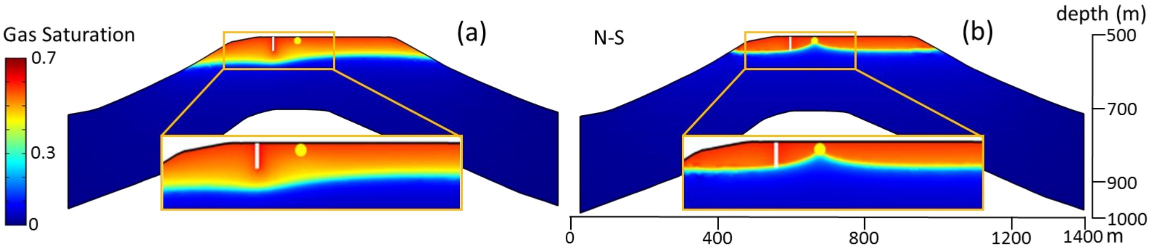

Figure 4-5. Gas saturation in the upper part of the aquifer for the A case after second year injection (a) and extraction (b). Injection well (white bar) and extraction well (yellow circle) are displayed. The cross-section plotted correspond to the N-S section in Figure 4-4.

During extraction, the pressure drops around the production well leading to a reduction of the gas plume. The contraction of the plume is observed at its lateral boundaries as the thickness of the gas plume is reduced. In case A, the plume is reduced 45 and 25 m in the north and south sides of the N-S section respectively (Figure 4-5b). Gas withdrawn leads to the upconing of the gas-water interface, a well-known process that occurs when pumping a light fluid overlying a dense fluid (i.e., freshwater above saltwater) (Bear and Dagan, 1964; Dagan and Bear, 1968; Muskat, 1949; Nordbotten and Celia, 2006). The pressure drop in the extraction well increases the pressure gradient between the well and the denser underlying fluid. Therefore, water migrates upwards towards the well leading, potentially, to the production of water and the mixing of both phases on the well (Figure 4-5b). To avoid massive water extraction, production wells are shut-down when gas saturation in the well is below 0.4.

The dynamics of hydrogen plume can be also observed through the mass of H_2 stored per aquifer square meter, calculated by vertically integrating the H_2 concentration over the aquifer thickness (Figure 4-6). During injection (Figure 4-6 a,c,e), the thickness of the H_2 plume increases leading to a maximum of 24 $kg \cdot m^{-2}$. The maximum hydrogen concentration coincides with the well location. High H_2 mass can be observed also towards the east of the dome, where the steeply dipping structures retain the gas. During production (Figure 4-6b,d,f), the hydrogen content decreases, being after production always below 15 $kg \cdot m^{-2}$. The gas plume narrows especially around the extraction well (the lowest H_2 mass within the plume); where the water upconing is more patent.

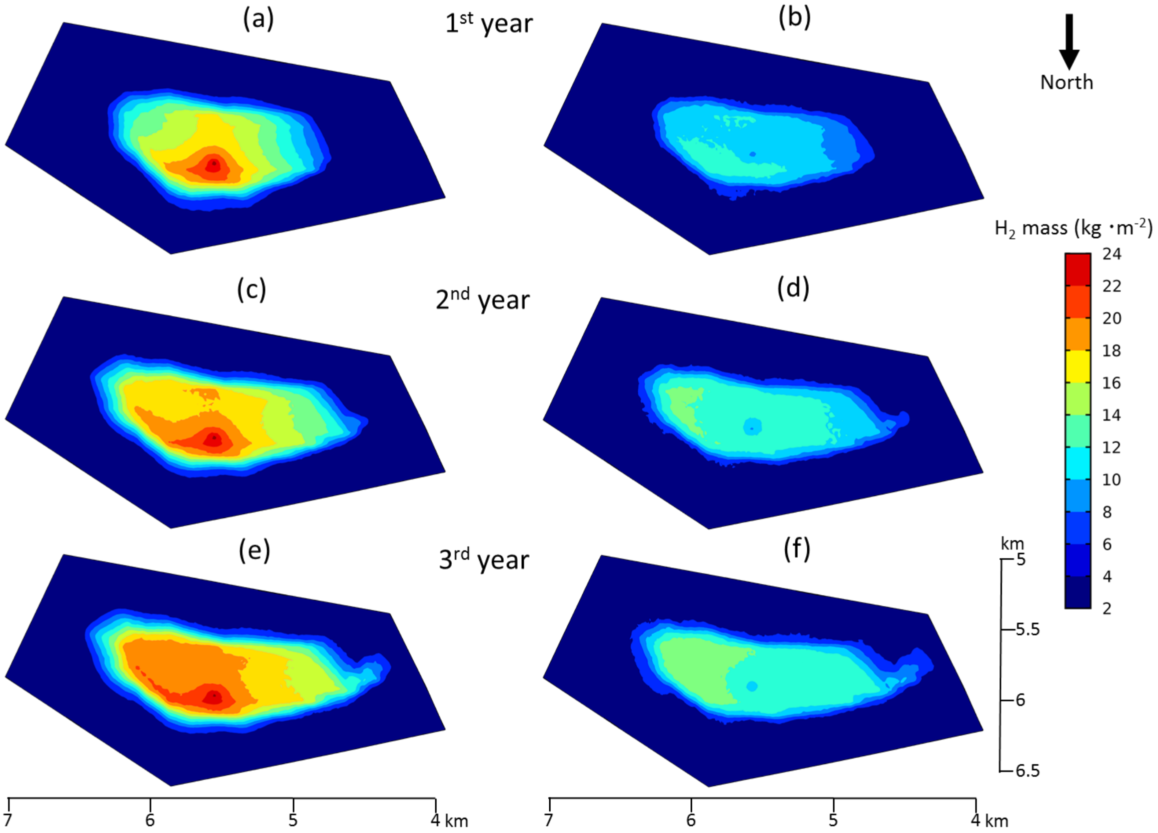

Figure 4-6. vertically integrated H_2 concentration over the aquifer thickness ($kg \cdot m^{-2}$) for the case A after: (a) first year injection, (b) first year extraction, (c) second year injection, (d) second year extraction, (e) third year injection and (f) third year extraction.

Hydrogen plume extends following the anticline crest (Figure 4-6). Expansion towards north, south and east is halted by the dome steeply slopes, while H_2 spreads continuously towards west. The footprint length ranges between 800 *m* (after injection) and 700 *m* (after production) in the direction perpendicular to the dome axis (N-S). However, the plume increasingly spreads following the dome axis (EW). It enlarges 550 *m* after three injection/production cycles, reaching a length of around 2 *km*. Thus, the shape of the footprint evolves with time. After the first cycle, the footprint has a pseudo-circular shape that responds to the radial pressure gradient induced by injection. After later cycles, the footprint becomes controlled by the shape of the caprock-aquifer surface. The area occupied by the footprint increases 0.22 km^2 in two years, reaching a maximum area of 1.11 km^2. The total volume of hydrogen injected is below the structure capacity and gas is retained in the dome; however, not all H_2 can be recovered after one injection/production cycle. The amount of gas in the subsurface and, consequently, the plume footprint increase each injection-extraction cycle (Figure 4-6).

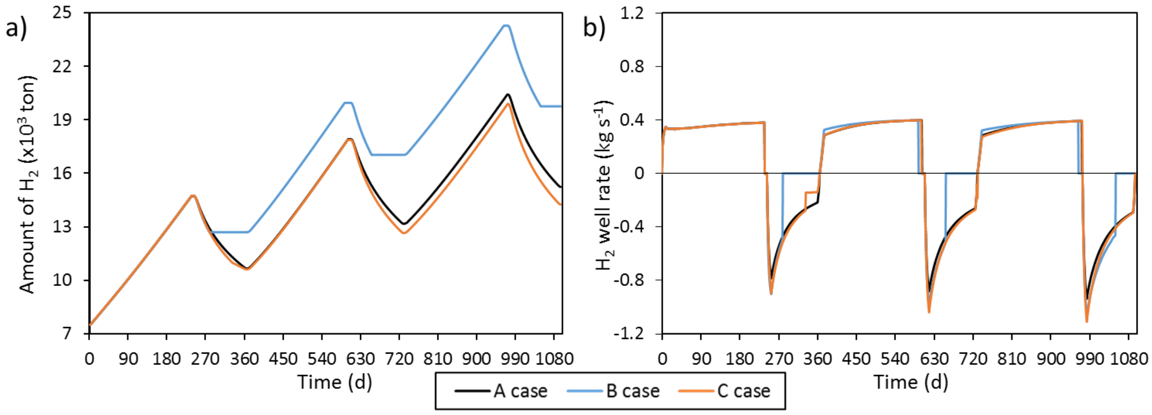

Figure 4-7. Evolution of the total amount of H_2 stored in the aquifer (a) and well injection and extraction rate (b) during operation for the three cases analysed.

The location of the extraction wells controls the efficiency of H_2 storage. The amount of hydrogen that can be withdrawn and the mass extraction flux achieved varies each year and depending on the well production scheme (Figure 4-7). The total mass of hydrogen stored increases every year regardless the annual production (Figure 4-7a). The amount of gas increases almost linearly during injection with a mass flux of around 0.345 $kg \cdot s^{-1}$. It should be kept in mind that the exact mass flux injected depends on gas density, which is function of pressure and temperature. As fluid pressure grows along the injection, gas density rises and, thus, injection mass flux is slightly and constantly increasing (Figure 4-7b). The pressure needed to maintain the prescribed gas volume flux in the injection well decreases in around 0.1 MPa every cycle. The hydrogen plume broadens with each operation cycle, providing a larger area for the hydrogen to migrate without having to overcome the capillary entry pressure that gas needs to occupy new aquifer regions. This lower resistance to gas migration explains the minor injection pressure required. At lower pressure, hydrogen density diminishes and the time required to inject the annual mass of hydrogen produced in Castilla-León (7242 tons) grows 5 days per cycle.

During production, the amount of hydrogen stored in the aquifer decreases except if the wells are shut-down due to upconing (Figure 4-7a). The gas-water interface reaches the production well in cases B (every year) and C (the first year at the eastern well) (Figure 4-7b). Due to upconing the gas saturation drops abruptly in the lower part of the well, increasing the water extracted and reducing the efficiency of the H_2 production (Figure 4-8). Thus, extraction stops when water saturation exceeds 0.6 at the bottom of the well. The upconing is especially relevant in the case B due to the deeper location of the well bottom. Each cycle, however, the extraction operation time of the case B increases

(36, 48 and 76 days of operation the first, second and third year respectively) (Figure 4-7b). In each case and at every cycle, the extracted H_2 mass flux reaches its maximum at the beginning of production. Later, the extraction drops along with the gas saturation around the production well. The production mass flux and the total amount of hydrogen withdrawn increase every cycle due to the higher amount of H_2 stored in the aquifer.

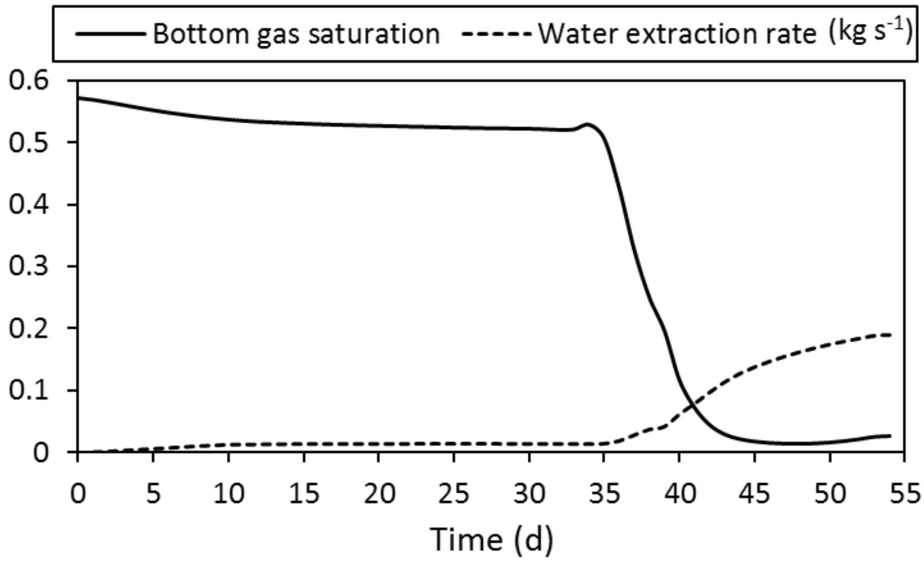

Figure 4-8. Gas saturation evolution at the extraction well bottom and water extraction mass flux ($kg \cdot s^{-1}$) during the first production cycle for case B if production well is not stopped. Upconing is evident after 35 days.

The different extraction strategies can be better compared by means of the amount of hydrogen recovered (Figure 4-9). Each year the amount of produced hydrogen increases for all extraction strategies. This trend, however, is expected to attenuate as more injection-extraction cycles are operated. In cases A and C the percentage of H_2 recovered is significant even after one injection/production cycle. In case B, the reduced production period due to upconing hinders the total amount of H_2 produced. Interestingly, case C shows consistently the best recovering ratio despite the closure of its eastern well after 89 days of operation the first year. Upconing on the eastern well of case C, nevertheless, causes the highest water volume extracted in a cycle (Table 4-2).

Assuming a re-electrification efficiency of 60% (EERE-Energy Efficiency & Renewable Energy, 2016), the amount of electricity that could be delivered to the grid during summer can be evaluated (Table 4-2). In the best case, 15% of the electricity consumed in the city of Burgos between June and September can be saved through underground hydrogen storage. Compared with the high recovering ratio of hydrogen from the underground storage (78% in the best case) only a maximum of 30% of the initial surplus energy can be regained. It should be notice that other uses of hydrogen, like fuel for vehicles or industrial applications, have much higher conversion efficiency. Furthermore, well-stablish technologies for H_2 production and re-electrification have been evaluated in this study. More efficient technologies are in first application phases and it is anticipated that the over ground conversion processes will improve in the near future (Bertuccioli et al., 2014).

Table 4-2. Summary of gas storage and energy efficiency values. % water mass withdrawn is the ratio between the mass of water and the mass of H_2 extracted; % energy recovered is the ratio between the energy re-electrified and the initial yearly surplus energy on Castilla-Leon; and % Burgos consumption is the ration between the energy re-electrified and the energy summer (Jun.-Sept.) consumption in Burgos.

	A case			B case			C case		
	1st y	2nd y	3rd y	1st y	2nd y	3rd y	1st y	2nd y	3rd y
H_2 produced (ton)	4068	4748	5183	2063	2943	4540	4117	5220	5637
Av. H_2 extraction (ton/d)	33.3	38.9	42.5	57.3	61.3	59.7	33.7	42.8	46.2
% H_2 recovered	56	65	71	28	41	63	57	72	78
% water mass withdrawn	5.04	2.10	1.41	1.84	1.08	0.92	6.49	2.25	1.41
Energy produced (GWh)	81	95	104	41	59	91	82	104	113
% energy recovered	22	25	28	11	16	24	22	28	30
% Burgos consumption	11	13	14	6	8	12	11	14	15

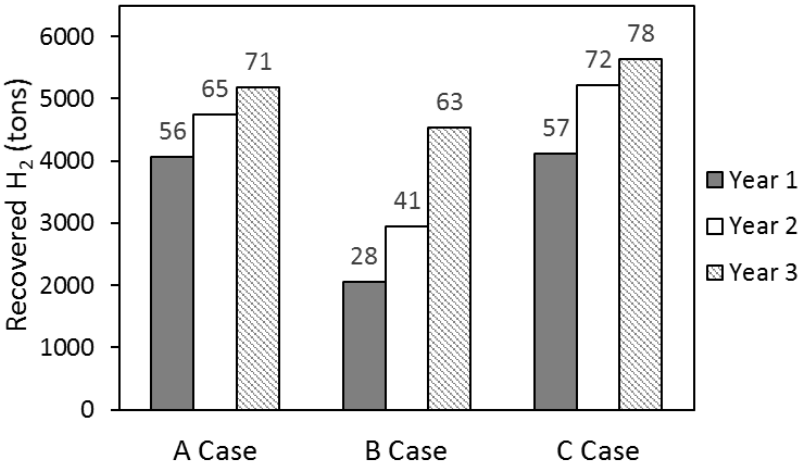

Figure 4-9. Total amount of H_2 produced for the three years of operation and for all the cases. The percentage of H_2 recovered (ration between the H_2 produced and the H_2 injected at the same year) is displayed on top of each column.

4.2.5 Conclusions

The study demonstrates that underground hydrogen storage in the San Pedro dome saline aquifer can be operated with reasonable recovery ratios for seasonal energy mismatches. No hydrogen crossed the structure spill point and, despite the high density and viscosity contrast between hydrogen and water, no viscous fingering occurs. The results infer that steeply dipping structures can store hydrogen gas without using other cushion gases. Such structures reveal critical for an efficient storage. More site-specific data of aquifer heterogeneity, which would promote a non-uniform gas distribution (Pfeiffer et al., 2017), should be acquired before actual operation in the San Pedro dome. However, the results here presented show the average performance in the aquifer.

Regardless the uncertainty in the model parameters such total H_2 injected, other well locations and length, and larger operational pressure range; the study found that significant amount of H_2 can be recovered if several shallow extraction wells are located beneath the caprock. Upconing appears as the major limitation on saline aquifer storage without using other cushion gases. However, different extraction well configurations can prevent its effects. The results also evidence the necessity of well monitoring during operation to prevent the loss of efficiency by water intrusion.

Current energy production data and estimations of surplus energy suggest that sufficient amount of hydrogen can be produced in Castilla-León to consider its storage in the subsurface. Up to 30% of global energy efficiency, with a maximum H_2 recovery ratio of 78% can be achieved. This means that up to 15% of the electricity consumption of a city like Burgos (175.000 inhabitants) during the months from June to September (the ones with lower wind energy production) can be delivered to the grid by re-electrification after underground hydrogen storage. Results show that dominant energy losses during the whole process arise from the energy-hydrogen conversion. The presence of favorable geological traps (like the one used in this study), the foreseen advances in H_2-energy conversion technologies and the expected increase of wind power generation in the next decade; anticipates a relevant role of underground hydrogen storage in the near future.

5 General conclusions and perspectives

The dynamics of gases in underground storage in porous media has been investigated using numerical models. Multiphase flow models have been applied to carbon and hydrogen storage and a reactive transport model was used to characterize the interaction between carbon dioxide and the minerals of the aquifer. These models appear to be useful tools for the pre-injection assessment of the gas storage and for monitoring.

The multiphase flow formulations and solute transport in porous media implemented in the thesis are explained in chapter 2. The mathematical models as well as the numerical approaches applied are described. Both numerical tools have been verified through various benchmarks and are applied to model the dynamics of underground gas storage in chapters 3 and 4.

Section 3.2 described the interplay between the processes affecting CO_2 after its injection into a subsurface anticline-syncline aquifer with a multiphase flow model. A large range of temporal and spatial scales are involved, posing numerous challenges. These challenges include the numerical representation of gravity current migration, capillarity, dissolution and convective mixing. The model is able to evaluate such processes, thereby quantifying the evolution of the different trapping mechanism acting on the carbon dioxide. The injection locations have been varied to evaluate the effects of aquifer slope on the fate of the injected CO_2.

The interaction between convective flow and geochemistry in a carbon storage project is evaluated in section 3.3. A coupled reactive transport model, where chemical reactions vary fluid density, aquifer porosity and permeability; while flow influences geochemistry was implemented for a variety of Rayleigh and Damköhler numbers. The chemical system is representative of the Hontomín CCS pilot storage site, a carbonate aquifer with high sulphate content. The effect on CO_2 solubility of the interplay between geochemistry and convective mixing was investigated.

Section 4.2 analyzes a seasonal hydrogen storage in a saline aquifer by means of a 3D two-phase flow model. Current data from Castilla-León (north Spain) wind energy generation has been used to estimate the surplus energy quantity and occurrence.

Three years of injection-production cycles were evaluated in an aquifer structure with different extraction well configurations.

Numerical models are a representation of the processes occurring in the nature. A number of assumptions have to be made to depict the driving forces of the complex natural systems. Depending on the purpose of the model, the key processes will vary and, consequently, the features implemented in the model. In the research presented in this thesis some aspects as the heterogeneity of the media have been neglected. Furthermore, some key parameters for flow in porous media, as geometry and permeability of the aquifers, are case dependent. One should, therefore, be cautious not to over-generalize the results of this research. Some insights for underground gas storage arise, however, from the numerical experiences presented above.

Due to the lower density of injected fluids compared with native fluids, they tend to migrate upwards to the top of the storage formation. Gas migration and accumulation is, thus, greatly influenced by aquifer geometry and the surface slope of the aquifer/caprock interface. In the case of hydrogen storage, steeply dipping structures are essential for the retention of H_2. The high mobility of hydrogen promotes its spreading along the top surface, making leakage more likely in less dipping structure.

The anticline-syncline case evidences the strong influence of aquifer geometry on CO_2 storage: gravity current velocity, plume splitting and the CO_2 footprint are driven by variations in aquifer slope. The evolution of the different CO_2 trapping mechanisms depends as well on aquifer geometry and free-phase plume depletion time is determined by the distance of injection to anticline crest. A larger distance leads to a longer plume footprint, with the consequent risk of leakage, although, capillary trapping is enhanced.

Furthermore, the presence of flat or concave surfaces (as anticlines or domes) in the top of the aquifer leads to a drop in plume migration velocity; promoting convective mixing in the case of carbon dioxide storage. This process accelerates greatly CO_2 dissolution, leading to more stable storage and to a safer CO_2 injection. The reactive transport model of section 3.3 shows that convective mixing is also influenced by chemical reactions. In the carbonate aquifer, with a high sulphate concentration, analysed in this thesis, the CO_2 dissolution rate is enhanced by chemical reactions. Although, gypsum precipitation reduces porosity and permeability; it also acts as a Ca^{2+} sink, leading to further calcite dissolution and, consequently, the general increase of porosity development.

The influence of chemical reactions on convective mixing depends on the specific chemical system of the aquifer. In addition, the time of onset of fluid convection varies with the physical characteristics of the aquifer (Rayleigh number, porosity and diffusivity). Results described above, taking account of these factors suggests that solubility trapping in carbon storage may have a more relevant role at initial times than initially expected (Metz et al., 2005, p., 208, figure 5.9). It should be noticed that the homogenization of aqueous CO_2 concentration throughout the aquifer will constrain convective mixing. The total capacity and width of the aquifers would, thus, influence the amount and velocity of carbon dissolution.

The interplay between chemical reactions and flow is complex. As such comprehensive site specific reactive transport models are recommended for CCS projects. Fluid mixing is critical in geochemical reactions. The majority of reactions occur where concentration gradient is perpendicular to the flow direction, leading to a non-uniform mineral dissolution-precipitation. The results suggest that addition of certain aqueous species to carbon dioxide injection may enhance CO_2 dissolution and, therefore, increase storage safety. The elaboration of multiphase reactive transport models in both contexts (CCS and UHS) would be interesting to assess such relations.

For the case of underground hydrogen storage, this research demonstrates the viability of hydrogen storage in saline aquifers. A maximum hydrogen recovery ratio of 78% has been estimated. Upconing of the denser native fluid phase represents the major challenge. However, it can be avoided by locating extraction wells close to the top surface of the aquifer and with appropriate operation and monitoring during gas production. Energy-hydrogen conversion represents the major energy losses in the process. The anticipated improvement of these technologies together with the foreseen increase of the wind power generation, suggests a relevant role of UHS in the future energy supply system.

Future work on modeling of multiphase flows in the subsurface could usefully explore the coupling with other relevant processes in the gas storage operation like geomechanics, geochemistry and thermal effects. As shown in this thesis, geochemical reactions can influence the fate of CO_2 in the subsurface. Carbon immobilization occur, generally, at large time scales being of minor relevance in deep saline storages. However, chemical reactions may modify the characteristics of the aquifer, i.e. changing porosity and permeability, being relevant for the dynamics of the storage. Furthermore, experiences in basaltic rocks show a fast carbon mineralization (Gislason et al., 2014). On other hand, fluid injection in saline aquifers lead to overpressurization with the consequent risk of fracture creation in the caprock or re-activation of existing faults. The pressure build up can, thus, potentially promote gas leakage or induce seismicity. The modeling of multiphase flow coupled with geochemistry and geomechanics can give insights in such processes.

The iCP numerical tool integrates together the capabilities of the general purpose finite element framework COMSOL Multiphysics (Comsol, 2016) and geochemical simulator PHREEQC (Parkhurst and Appelo, 2013). The coupling of the multiphase formulations used in this thesis with iCP would generate a useful tool for multiphase flow challenges in porous media. In comparison with other available multiphase software that can deal with geochemical reactions (Farajzadeh et al., 2012; Lu and Lichtner, 2005; Sin, 2015; Van der Lee et al., 2003; T. Xu et al., 2006), iCP would allow the representation of a large range of physical processes. Full multiphysics models could be developed to tackle strongly coupled geochemical challenges.

Another aspect that would be interesting to address in a further study is the comparison of numerical models with data from injection sites and from experimental work. Monitored and experimental data are essential to understand the dynamics and long-term safety of the storages. They can assure reliability and accuracy of numerical models while numerical predictions would aid the interpretation of data and the assessment of critical parameters. The iterative cross-validation between numerical simulations and monitoring and experimental data would improve the understanding of gas storage dynamics, increasing the safety and efficiency of storage operation.

5.1 Conclusions générales et perspectives en français

La dynamique des gaz dans un stockage souterrain en milieu poreux a été étudiée à l'aide de modèles numériques. Des modèles d'écoulement multiphasique ont été appliqués au stockage du dioxyde de carbone et de l'hydrogène et un modèle de transport réactif utilisé pour caractériser l'interaction entre le CO_2 et les minéraux de l'aquifère. Il s'est avéré que ces modèles sont utiles pour l'évaluation préliminaire à l'injection du stockage de gaz ainsi que de sa surveillance.

Les formulations des flux multiphasiques et le transport des solutés dans les milieux poreux implémentés au cours de cette thèse sont expliqués dans la section 2. Les modèles mathématiques ainsi que les approches numériques appliquées sont décrits. Les deux outils numériques ont été vérifiés et sont appliqués pour modéliser la dynamique du stockage de gaz souterrain dans les chapitres 3 et 4.

La section 2 décrit à l'aide d'un modèle d'écoulement multiphasique l'interaction des processus affectant le CO_2 après son injection dans un aquifère souterrain anticlinal-synclinal. De nombreux problèmes se sont posés en raison des grandes différences dans les échelles temporelles et spatiales. Parmi ceux-ci, on peut noter la représentation numérique de la migration du courant gravitaire, de la capillarité, de la dissolution et du mélange convectif. Le modèle est capable d'évaluer de tels processus, quantifiant ainsi l'évolution des différents mécanismes de piégeage du dioxyde de carbone. Différents points d'injection ont été choisis pour évaluer les effets de la pente de l'aquifère sur le sort du CO_2 injecté.

L'interaction entre l'écoulement convectif et la géochimie dans un projet de stockage est évaluée dans la section 3.3. Un modèle de transport réactif couplé a été mis en œuvre pour différentes valeurs de Rayleigh et de Damköhler, dans lequel les réactions chimiques font varier la densité des fluides, la porosité et la perméabilité de l'aquifère, pendant que l'écoulement affecte la géochimique. Le système chimique est représentatif du site pilote de stockage CO_2 d'Hontomín, un aquifère carbonaté avec de grandes quantités de sulfates. L'effet de l'interaction entre la géochimie et le mélange convectif sur la solubilité du CO_2 a été étudié.

La section 4.2 analyse un stockage saisonnier d'hydrogène dans un aquifère salin au moyen d'un modèle d'écoulement diphasique en 3D. Les données courantes de production d'énergie éolienne en Castille-et-León, dans le nord de l'Espagne, ont été utilisées pour évaluer les occurrences et la quantité des surplus d'énergie. Des cycles d'injection-production sur une période de trois ans ont été évalués sous différentes configurations de puits d'extraction dans une structure aquifère.

Les modèles numériques constituent une représentation des processus qui se produisent dans la nature. De nombreuses hypothèses doivent être faites pour décrire les forces qui agissent sur les systèmes naturels complexes. Les processus essentiels et, donc, les caractéristiques du modèle, varient en fonction de l'objectif de la modélisation. Dans la recherche présentée dans cette thèse, certains aspects tels que l'hétérogénéité du milieu ont été négligés. De plus, certains paramètres essentiels de l'écoulement dans les milieux poreux, tels que la géométrie et la perméabilité des aquifères, dépendent également des cas à l'étude. Il ne faut donc pas généraliser outre mesure les résultats de cette recherche. En revanche, les expériences numériques présentées ici apportent des éléments intéressants sur le stockage souterrain de gaz.

Comme la densité des fluides natifs est plus élevée que celle des fluides injectés, ces derniers tendent à migrer vers le haut de la formation de stockage. La migration et l'accumulation de gaz est donc grandement influencée par la géométrie de l'aquifère et par la pente de la surface de l'interface aquifère/roche de couverture. Dans le cas du stockage de l'hydrogène, des structures à fort pendage sont essentiels pour sa rétention. La grande mobilité de l'hydrogène favorise sa dispersion le long de la surface supérieure et les fuites sont plus probables dans des structures de moindre pendage.

Le cas anticlinal-synclinal met en évidence la forte influence de la géométrie de l'aquifère sur le stockage du CO_2. La vitesse du courant gravitaire, la division du panache et l'empreinte du CO_2 sont déterminés par les variations de la pente de l'aquifère. L'évolution des différents mécanismes de piégeage du CO_2 dépend également de la géométrie de l'aquifère. La durée de résorption du panache en phase libre est déterminée par la distance du point d'injection à la crête de l'anticlinal. Une distance plus grande conduira à une empreinte du panache plus longue, avec les risques de fuite induits, bien que le piégeage capillaire soit plus important.

De plus, la présence de surfaces planes ou concaves (comme des anticlinaux ou des dômes) au sommet de l'aquifère provoque une baisse de la vitesse de migration, ce qui favorise le mélange convectif dans le cas du stockage du dioxyde de carbone. Ce processus accélère grandement la dissolution du CO_2, ce qui augmente la stabilité du stockage et la sécurité de l'injection. Le modèle de transport réactif, exposé en section 3.3, montre que le mélange convectif est également influencé par les réactions chimiques. Dans l'aquifère carbonaté à haute concentration en sulfates, analysé dans cette thèse, le taux de dissolution du CO_2 augmente avec les réactions chimiques. Bien que la précipitation du gypse réduise la porosité et la perméabilité, elle agit aussi en tant que puits de Ca^{2+}, conduisant à une dissolution supplémentaire de calcite et, donc, un accroissement général de la porosité.

L'influence des réactions chimiques sur le mélange convectif dépend du système chimique spécifique de l'aquifère. De plus, le début de la convection varie avec les caractéristiques physiques de l'aquifère (valeur de Rayleigh, porosité et diffusivité). Les résultats décrits ci-dessus, prenant en compte ces facteurs, laissent à penser que le piégeage par dissolution dans le stockage de CO_2 peut avoir un rôle plus important au début que celui espéré initialement (Metz et al., 2005, p., 208, figure 5.9). Il faut noter que l'homogénéisation de la concentration du CO_2 en phase aqueuse sur l'ensemble de l'aquifère va contraindre le mélange convectif. La capacité totale et la largeur de l'aquifère va donc influencer la quantité et la vitesse de dissolution du CO2.

L'interaction entre les réactions chimiques et l'écoulement est complexe. C'est pourquoi il est recommandé pour les projets de CCS de disposer de modèles de transport réactif complets et spécifiques au site. Le mélange des fluides est essentiel dans les réactions chimiques. La majeure partie des réactions advient là où le gradient de concentration est perpendiculaire à la direction de l'écoulement, ce qui conduit à une dissolution-précipitation minérale non uniforme. Les résultats suggèrent également que l'addition de certaines substances au dioxyde de carbone peut augmenter sa dissolution et augmenter ainsi la sécurité du stockage. Pour évaluer de telles relations, il serait intéressant d'élaborer des modèles de transport réactif de fluide multiphasique dans les deux contextes, CSS et UHS.

Dans le cas de l'UHS, cette recherche démontre la viabilité du stockage de l'hydrogène dans des aquifères salins. Un taux de récupération d'hydrogène de 78% a été estimé. L'intrusion du fluide natif plus dense est le principal problème à résoudre. Il peut cependant être évité en situant les puits d'extraction à proximité de la surface supérieure de l'aquifère et en opérant et surveillant adéquatement la phase de production du gaz. La majeure partie des pertes énergétiques du processus proviennent de la conversion électricité-hydrogène. L'amélioration escomptée de ces technologies, associée à l'accroissement prévu de la production électrique éolienne, laisse à prévoir que l'UHS va jouer un rôle important dans le système de production électrique à l'avenir.

Le futur travail sur la modélisation de l'écoulement des fluides multiphasiques dans le sous-sol devra examiner le couplage avec d'autres processus intervenant dans l'opération de stockage gazier, relevant de la géomécanique, de la géochimie et des effets thermiques. Comme cette thèse le montre, les réactions géochimiques peuvent influencer le sort du CO_2 dans le sous-sol. L'immobilisation du CO_2 se produit généralement sur de longues durées, de moindre importance pour les stockages salins profonds. En revanche, les réactions chimiques peuvent modifier les caractéristiques de l'aquifère, c'est-à-dire en changer la porosité et la perméabilité, ce qui devient important pour la dynamique du stockage. De plus, les expériences dans des roches basaltiques montrent une minéralisation rapide du carbone (Gislason et al., 2014). Par ailleurs, l'injection de fluide dans des aquifères salins provoque une surpression risquant de fracturer la roche de couverture ou de réactiver des défauts existants. La montée en pression peut alors éventuellement favoriser les fuites de gaz ou entraîner une séismicité. La modélisation d'écoulement multiphasique couplée à la géochimique et la géomécanique peut permettre de mieux connaître ces processus.

L'outil numérique iCP réunit les capacités du logiciel COMSOL Multiphysics (Comsol, 2016), cadre universel de calcul par éléments finis, et le simulateur géochimique PHREEQC (Parkhurst and Appelo, 2013). Le couplage avec iCP des formulations multiphasiques utilisées dans cette thèse devrait donner un outil utile pour traiter les problèmes difficiles d'écoulement multiphasique dans les milieux poreux. Comparé à d'autres logiciels multiphasiques qui peuvent traiter les réactions géochimiques (Farajzadeh et al., 2012; Lu and Lichtner, 2005; Sin, 2015; Van der Lee et al., 2003; T. Xu et al., 2006; Yeh et al., 2012), iCP permet de prendre en compte des processus physiques d'une plus grande diversité. Des modèles multiphysiques complets pourraient être développés pour aborder des problèmes géochimiques à fort couplage.

Un autre aspect intéressant à traiter dans une future étude serait la comparaison des modèles numériques avec des données provenant des sites d'injection et d'expériences. Les données d'expériences et de suivi sont essentielles pour comprendre la dynamique et la sécurité à long terme des sites de stockage. Elles peuvent conforter la fiabilité et la précision des modèles numériques et les prévisions numériques pourraient aussi aider à interpréter les données et l'évaluation des paramètres critiques. La validation croisée itérative entre simulations numériques et données d'expériences et de suivi pourraient améliorer la connaissance de la dynamique du stockage de gaz et accroître la sécurité et l'efficacité des opérations de stockage.

References

Abadpour, A., Panfilov, M., 2009. Method of Negative Saturations for Modeling Two-phase Compositional Flow with Oversaturated Zones. Transp. Porous Media 79, 197–214. doi:10.1007/s11242-008-9310-0

AEE-Spanish Wind Energy Association, 2016. Eolica 2016. Wind Energy in Spain 1–128.

Agaoglu, B., Copty, N.K., Scheytt, T., Hinkelmann, R., 2015. Interphase mass transfer between fluids in subsurface formations: A review. Adv. Water Resour. 79, 162–194. doi:10.1016/j.advwatres.2015.02.009

Agnelli, M., Grandia, F., Credoz, A., Gasparini, A., Bruno, J., 2014. Use of diffusive gradients in thin films (DGT) as an early detection tool of low-intensity leakage from CO $_2$ storage. Greenh. Gases Sci. Technol. 4, 163–175. doi:10.1002/ghg.1383

Ahusborde, E., Kern, M., Vostrikov, V., 2015. Numerical simulation of two-phase multicomponent flow with reactive transport in porous media: application to geological sequestration of CO2. ESAIM Proc.

Allen, M.B., 1984. Why Upwinding is Reasonable, in: Finite Elements in Water Resources. Springer Berlin Heidelberg, Berlin, Heidelberg, pp. 13–23. doi:10.1007/978-3-662-11744-6_2

Altunin, V. V, Sakhabetdinov, M.A., 1972. Viscosity of liquid and gaseous carbon dioxide at temperatures 220-1300 K and pressure up to 1200 bar. Teploenergetika 8, 85–89.

Andres, J.T.H., Cardoso, S.S.S., 2012. Convection and reaction in a diffusive boundary layer in a porous medium: Nonlinear dynamics. Chaos An Interdiscip. J. Nonlinear Sci. 22, 37113.

Andres, J.T.H., Cardoso, S.S.S., 2011. Onset of convection in a porous medium in the presence of chemical reaction. Phys. Rev. E 83, 46312.

Andrews, J., Shabani, B., 2012. Re-envisioning the role of hydrogen in a sustainable energy economy. Int. J. Hydrogen Energy 37, 1184–1203. doi:10.1016/j.ijhydene.2011.09.137

Angelini, O., Chavant, C., Chénier, E., Eymard, R., Granet, S., 2011. Finite volume approximation of a diffusion–dissolution model and application to nuclear waste storage. Math. Comput. Simul. 81, 2001–2017. doi:10.1016/j.matcom.2010.12.016

Antontsev, S., 1972. On the solvability of boundary value problems for degenerate two-phase porous flow equations. Din. Splos. Sredy Vyp.

Apecyl, 2016. Castilla y Leon podria llegar a asumir una parte relevante de la nueva potencia eolica hasta 2020 pero vamos con mucho retraso.

Assteerawatt, A., Bastian, P., Bielinski, A., Breiting, T., Class, H., Ebigbo, A., Eichel, H., Freiboth, S., Helmig, R., Kopp, A., others, 2005. MUFTE-UG: structure, applications and numerical methods.

Audigane, P., Gaus, I., Czernichowski-Lauriol, I., Pruess, K., Xu, T., 2007. Two-dimensional reactive transport modeling of CO_2 injection in a saline aquifer at the Sleipner site, North Sea. Am. J. Sci. 307, 974–1008. doi:10.2475/07.2007.02

Azad, V.J., Li, C., Verba, C., Ideker, J.H., Isgor, O.B., 2016. A COMSOL–GEMS interface for modeling coupled reactive-transport geochemical processes. Comput. Geosci. 92, 79–89. doi:10.1016/j.cageo.2016.04.002

Aziz, K., Settari, A., 1979. Petroleum reservoir simulation.

Bachu, S., 2003. Screening and ranking of sedimentary basins for sequestration of CO_2 in geological media in response to climate change. Environ. Geol. 44, 277–289.

Bachu, S., Bennion, B., 2008. Effects of in-situ conditions on relative permeability characteristics of CO2-brine systems. Environ. Geol. 54, 1707–1722. doi:10.1007/s00254-007-0946-9

Bailey, R.T., Morway, E.D., Niswonger, R.G., Gates, T.K., 2013. Modeling Variably Saturated Multispecies Reactive Groundwater Solute Transport with MODFLOW-UZF and RT3D. Groundwater 51, 752–761. doi:10.1111/j.1745-6584.2012.01009.x

Bandilla, K.W., Celia, M.A., Birkholzer, J.T., Cihan, A., Leister, E.C., 2015. Multiphase Modeling of Geologic Carbon Sequestration in Saline Aquifers. Groundwater 53, 362–377. doi:10.1111/gwat.12315

Bardelli, F., Mondelli, C., Didier, M., Vitillo, J.G., Cavicchia, D.R., Robinet, J.-C., Leone, L., Charlet, L., 2014. Hydrogen uptake and diffusion in Callovo-Oxfordian clay rock for nuclear waste disposal technology. Appl. Geochemistry 49, 168–177. doi:10.1016/j.apgeochem.2014.06.019

Barnolas, A., Pujalte, V., 2004. La Cordillera Pirenaica. Geol. España 233–241.

Barrett, R., Berry, M., Chan, T.F., Demmel, J., Donato, J., Dongarra, J., Eijkhout, V., Pozo, R., Romine, C., van der Vorst, H., 1994. Templates for the solution of linear systems: Building blocks for iterative methods xvii + 118. doi:10.1137/1.9781611971538

Barry, D.A., Miller, C.T., Culligan-Hensley, P.J., 1996. Temporal discretisation errors in non-iterative split-operator approaches to solving chemical reaction/groundwater transport models. J. Contam. Hydrol. 22, 1–17.

Bastian, P., 1999. Numerical computation of multiphase flows in porous media. Christian-Albrechts-Universität Kiel.

Bear, J., 1972. Dynamics of fluids in porous media. Dover.

Bear, J., Buchlin, J.M., others, 1991. Modelling and applications of transport phenomena in porous media. Springer.

Bear, J., Dagan, G., 1964. Some exact solutions of interface problems by means of the hodograph method. J. Geophys. Res. 69, 1563–1572.

Benzi, M., 2002. Preconditioning Techniques for Large Linear Systems: A Survey. J.

Comput. Phys. 182, 418–477. doi:10.1006/jcph.2002.7176

Bertuccioli, L., Chan, A., Hart, D., Lehner, F., Madden, B., Standen, E., 2014. Study on development of water electrolysis in the EU. Fuel cells Hydrog. Jt. Undert. 114.

Bickle, M., Chadwick, A., Huppert, H.E., Hallworth, M., Lyle, S., 2007. Modelling carbon dioxide accumulation at Sleipner: Implications for underground carbon storage. Earth Planet. Sci. Lett. 255, 164–176.

Binning, P., Celia, M.A., 1999. Practical implementation of the fractional flow approach to multi-phase flow simulation. Adv. Water Resour. 22, 461–478.

Boot-Handford, M.E., Abanades, J.C., Anthony, E.J., Blunt, M.J., Brandani, S., Mac Dowell, N., Fernandez, J.R., Ferrari, M.-C., Gross, R., Hallett, J.P., Haszeldine, R.S., Heptonstall, P., Lyngfelt, A., Makuch, Z., Mangano, E., Porter, R.T.J., Pourkashanian, M., Rochelle, G.T., Shah, N., Yao, J.G., Fennell, P.S., 2014. Carbon capture and storage update. Energy Environ. Sci. 7, 130–189. doi:10.1039/C3EE42350F

Bourgeat, A., Granet, S., Smaï, F., 2013. Compositional two-phase flow in saturated–unsaturated porous media: benchmarks for phase appearance/disappearance. Simul. Flow Porous. Appl. Energy Environ. 81–106.

Bradshaw, J., Bachu, S., Bonijoly, D., Burruss, R., Holloway, S., Christensen, N.P., Mathiassen, O.M., 2007. CO_2 storage capacity estimation: issues and development of standards. Int. J. Greenh. Gas Control 1, 62–68.

Brenan, K.E., Campbell, S.L., Petzold, L.R., 1995. Numerical Solution of Initial-Value Problems in Differential-Algebraic Equations. Society for Industrial and Applied Mathematics. doi:10.1137/1.9781611971224

Brezzi, F., Douglas, J., Marini, L.D., 1985. Two families of mixed finite elements for second order elliptic problems. Numer. Math. 47, 217–235. doi:10.1007/BF01389710

Brooks, A.N., Hughes, T.J.R., 1982. Streamline upwind/Petrov-Galerkin formulations for convection dominated flows with particular emphasis on the incompressible Navier-Stokes equations. Comput. Methods Appl. Mech. Eng. 32, 199–259. doi:10.1016/0045-7825(82)90071-8

Brooks, R.H., Corey, A.T., 1964. Hydraulic properties of porous media and their relation to drainage design. Trans. ASAE 7, 26–28.

Brown, P.N., Hindmarsh, A.C., Petzold, L.R., 1994. Using Krylov Methods in the Solution of Large-Scale Differential-Algebraic Systems. SIAM J. Sci. Comput. 15, 1467–1488. doi:10.1137/0915088

Buckley, S.E., Leverett, Mc., 1942. Mechanism of fluid displacement in sands. Trans. AIME 146, 1–7.

Calvo, D., Barranco, J., Padilla, G., Brito, M., Becerra-Ramirez, R., Gosalvez, R., Gonzalez, E., Escobar, E., Melian, G., Nolasco, D., 2010. Emisión difusa de CO2 en el Campo de Calatrava, Ciudad Real» en Aportaciones recientes en Volcanología, 2005-2008 (González et al., eds.). Almagro (Spain), Cent. Estud. Calatravos 57–65.

Cao, H., 2002. Development of techniques for general purpose simulators.

Carden, P.O., Paterson, L., 1979. Physical, chemical and energy aspects of underground hydrogen storage. Int. J. Hydrogen Energy 4, 559–569. doi:10.1016/0360-3199(79)90083-1

Cardoso, S.S.S., Andres, J.T.H., 2014. Geochemistry of silicate-rich rocks can curtail spreading of carbon dioxide in subsurface aquifers. Nat. Commun. 5, 5743.

Carr, S., Premier, G.C., Guwy, A.J., Dinsdale, R.M., Maddy, J., 2014. Hydrogen storage and demand to increase wind power onto electricity distribution networks. Int. J. Hydrogen Energy 39, 10195–10207. doi:10.1016/j.ijhydene.2014.04.145

Carrayrou, J., Mosé, R., Behra, P., 2004. Operator-splitting procedures for reactive transport and comparison of mass balance errors. J. Contam. Hydrol. 68, 239–268. doi:10.1016/S0169-7722(03)00141-4

Carrayrou, J., Mosé, R., Behra, P., 2003. Modeling reactive transport in porous media: iterative scheme and combination of discontinuous and mixed-hybrid finite elements. Comptes Rendus. Mec. 211–216.

Carroll, S., Hao, Y., Smith, M., Sholokhova, Y., 2013. Development of scaling parameters to describe CO_2-rock interactions within Weyburn-Midale carbonate flow units. Int. J. Greenh. Gas Control 16, S185--S193.

Cavanagh, A.J., Haszeldine, R.S., 2014. The Sleipner storage site: Capillary flow modeling of a layered CO2 plume requires fractured shale barriers within the Utsira Formation. Int. J. Greenh. Gas Control 21, 101–112. doi:10.1016/j.ijggc.2013.11.017

Celia, M.A., Bachu, S., Nordbotten, J.M., Bandilla, K.W., 2015. Status of CO2 storage in deep saline aquifers with emphasis on modeling approaches and practical simulations, Water Resources Research. doi:10.1002/2015WR017609

Celia, M.A., Nordbotten, J.M., 2009. Practical Modeling Approaches for Geological Storage of Carbon Dioxide. Ground Water 47, 627–638. doi:10.1111/j.1745-6584.2009.00590.x

CENER. National Center of Renewable Energy, 2013. Current and future analysis of potential storage in the Spanish electric system. Intern. Rep.

Charlton, S.R.S., Parkhurst, D.L.D., 2011. Modules based on the geochemical model PHREEQC for use in scripting and programming languages. Comput. Geosci. 37, 1653–1663. doi:10.1016/j.cageo.2011.02.005

Chavent, G., 1981. The global pressure, a new concept for the modelization of compressible two-phase flows in porous media. Flow Transp. Porous Media 191–198.

Chavent, G., Jaffré, J., 1986. Mathematical Models and Finite Elements for Reservoir Simulation: Single Phase, Multiphase and Multicomponent Flows through Porous Media. North-Holland.

Chen, Z.-X., Bodvarsson, G.S., Witherspoon, P.A., 1992. Comment on “Exact integral solutions for two-phase flow” by David B. McWhorter and Daniel K. Sunada. Water Resour. Res. 28, 1477–1478. doi:10.1029/92WR00473

Chen, Z., Ewing, R.E., 1997a. Comparison of various formulations of three-phase flow in porous media. J. Comput. Phys. 132, 362–373.

Chen, Z., Ewing, R.E., 1997b. Fully Discrete Finite Element Analysis of Multiphase Flow in Groundwater Hydrology. SIAM J. Numer. Anal. 34, 2228–2253. doi:10.1137/S0036142995290063

Chen, Z., Huan, G., Ma, Y., 2006. Computational methods for multiphase flows in porous media. Siam.

Chen, Z., Qin, G., Ewing, R.E., 2000. Analisis of a compositonal model for fluid flow in porous media. SIAM J. Appl. Math. 60, 747–777.

Chu, S., 2009. Carbon capture and sequestration. Science (80-.). 325, 1599.

Chung, J., Hulbert, G.M., 1993. A Time Integration Algorithm for Structural Dynamics With Improved Numerical Dissipation: The Generalized-α Method. J. Appl. Mech. 60, 371. doi:10.1115/1.2900803

Civan, F., 2001. Scale effect on porosity and permeability: Kinetics, model, and correlation. AIChE J. 47, 271–287.

Class, H., Ebigbo, A., Helmig, R., Dahle, H.K., Nordbotten, J.M., Celia, M.A., Audigane, P., Darcis, M., Ennis-King, J., Fan, Y., others, 2009. A benchmark study on problems related to CO_2 storage in geologic formations. Comput. Geosci. 13, 409–434.

Class, H., Helmig, R., Bastian, P., 2002. Numerical simulation of non-isothermal multiphase multicomponent processes in porous media. Adv. Water Resour. 25, 533–550. doi:10.1016/S0309-1708(02)00014-3

Coats, K.H.K., 1980. No Title. Soc. Pet. Eng. J. 20, 363–376. doi:10.2118/8284-PA

Codina, R., 1998. Comparison of some finite element methods for solving the diffusion-convection-reaction equation. Comput. Methods Appl. Mech. Eng. 156, 185–210. doi:10.1016/S0045-7825(97)00206-5

Comsol, A.B., 2016. COMSOL Reference Manual (version 5.2a). Version Sept. 1–1378.

Cosmin, P.G., Schenk, O., Lubin, M., Gäertner, K., 2014. An Augmented Incomplete Factorization Approach for Computing the Schur Complement in Stochastic Optimization. SIAM J. Sci. Comput. 36, C139–C162. doi:10.1137/130908737

Crotogino, F., Huebner, S., 2008. Energy storage in salt caverns: developments and concrete projects for adiabatic compressed air and for hydrogen storage, in: KBB

Underground Technologies GMBh, Hannover, Germany. SMRI Spring Technical Meeting, Porto, Portugal. pp. 28–29.

Dagan, G., Bear, J., 1968. Solving the problem of local interface upconing in a coastal aquifer by the method of small perturbations. J. Hydraul. Res. 6, 15–44.

Davis, T.A., 2006. Direct Methods for Sparse Linear Systems. Society for Industrial and Applied Mathematics. doi:10.1137/1.9780898718881

De Lucia, M., Bauer, S., Beyer, C., Kühn, M., Nowak, T., Pudlo, D., Reitenbach, V., Stadler, S., 2012. Modelling CO2-induced fluid–rock interactions in the Altensalzwedel gas reservoir. Part I: from experimental data to a reference geochemical model. Environ. Earth Sci. 67, 563–572. doi:10.1007/s12665-012-1725-9

De Windt, L., Burnol, A., Montarnal, P., van der Lee, J., 2003. Intercomparison of reactive transport models applied to UO2 oxidative dissolution and uranium migration. J. Contam. Hydrol. 61, 303–312. doi:10.1016/S0169-7722(02)00127-4

Delany, J.M., Lundeen, S.R., 1990. The LLNL thermochemical database. Lawrence Livermore Natl. Lab. Rep. UCRL-21658 150.

Didier, M., Leone, L., Greneche, J.-M., Giffaut, E., Charlet, L., 2012. Adsorption of hydrogen gas and redox processes in clays. Environ. Sci. Technol. 46, 3574–3579.

Doster, F., Nordbotten, J.M., Celia, M.A., 2013. Impact of capillary hysteresis and trapping on vertically integrated models for CO2 storage. Adv. Water Resour. 62, 465–474.

Douglas, J., Peaceman, D.W., Rachford, H.H.H., 1959. a Method for Calculating Multi-Dimensional Immiscible Displacement. Trans. AIME 216, 297–308.

Drummond, S.E., 1981. Boiling and mixing of hydrothermal fluids: chemical effects on mineral precipitation. Pennsylvania State University.

Ebigbo, A., Class, H., Helmig, R., 2007. CO2 leakage through an abandoned well: problem-oriented benchmarks. Comput. Geosci. 11, 103–115.

Ebigbo, A., Golfier, F., Quintard, M., 2013. A coupled, pore-scale model for methanogenic microbial activity in underground hydrogen storage. Adv. Water Resour. 61, 74–85. doi:10.1016/j.advwatres.2013.09.004

ECLIPSE, S., 2004. ECLIPSE Reference Manual 2004A.

Edenhofer, O., Pichs-Madruga, R., Sokona, Y., Farahani, E., Kadner, S., Seyboth, K., Adler, A., Baum, I., Brunner, S., Eickemeier, P., Kriemann, B., Savolainen, J., Schlimer, S., von Stechow, C., Zwickel, T., Minx, J.C., others, Schlümer, S., von Stechow, C., Zwickel, T., Minx, J.C., 2014. IPCC, Climate Change 2014: Mitigation of Climate Change. Cambridge University Press.

EERE-Energy Efficiency & Renewable Energy, 2016. Comparison of Fuel Cell Technologies.

EIA-International Energy Agency, 2016. Underground Natural Gas Storage Capacity.

Elenius, M.T., Voskov, D. V, Tchelepi, H.A., 2015. Interactions between gravity currents and convective dissolution. Adv. Water Resour. 83, 77–88. doi:http://dx.doi.org/10.1016/j.advwatres.2015.05.006

Elío, J., Ortega, M.F., Nisi, B., Mazadiego, L.F., Vaselli, O., Caballero, J., Grandia, F., 2015. CO2 and Rn degassing from the natural analog of Campo de Calatrava (Spain): Implications for monitoring of CO2 storage sites. Int. J. Greenh. Gas Control 32, 1–14. doi:10.1016/j.ijggc.2014.10.014

Emami-Meybodi, H., Hassanzadeh, H., 2015. Two-phase convective mixing under a buoyant plume of CO_2 in deep saline aquifers. Adv. Water Resour. 76, 55–71.

Emami-Meybodi, H., Hassanzadeh, H., Green, C.P., Ennis-King, J., 2015. Convective dissolution of CO_2 in saline aquifers: Progress in modeling and experiments. Int. J. Greenh. Gas Control 40, 238–266. doi:http://dx.doi.org/10.1016/j.ijggc.2015.04.003

Ennis-King, J., Paterson, L., 2007. Coupling of geochemical reactions and convective mixing in the long-term geological storage of carbon dioxide. Int. J. Greenh. Gas Control 1, 86–93.

Ennis-King, J., Paterson, L., 2003. Role of convective mixing in the long-term storage of carbon dioxide in deep saline formations, in: SPE Annual Technical Conference and Exhibition.

Espie, T., Woods, A., 2014. Testing some common concepts in CO2 storage. Energy Procedia 63, 5450–5460.

European Commission, 2015. EU Energy in figures, Statistical pocketbook 2015. Publ. Off. Eur. Union 1–268. doi:10.2833/105662

European Commission, 2014. EU Energy Markets in 2014. Publ. Off. Eur. Union 1–172. doi:10.2833/2400

European Commission, 2012. Energy roadmap 2050. Publ. Off. Eur. Unio 1–24. doi:10.2833/10759

European Commission, 2011. Assessment of the required share for stable EU electricity supply until 2050 1–45.

European Commission, 2010. Energy 2020 A strategy for competitive, sustainable and secure energy. Publ. Off. Eur. Union, 1–28.

Evans, D.J., 2007. An appraisal of Underground Gas Storage technologies and incidents, for the development of risk assessment methodology. British Geological Survey Open Report.

Fahs, M., Carrayrou, J., Younes, A., Ackerer, P., 2008. On the Efficiency of the Direct Substitution Approach for Reactive Transport Problems in Porous Media. Water. Air. Soil Pollut. 193, 299–308. doi:10.1007/s11270-008-9691-2

Falta, R.W., 2003. Modeling sub-grid-block-scale dense nonaqueous phase liquid (DNAPL) pool dissolution using a dual-domain approach. Water Resour. Res. 39, n/a-n/a. doi:10.1029/2003WR002351

Falta, R.W., 2000. Numerical modeling of kinetic interphase mass transfer during air sparging using a dual-media approach. Water Resour. Res. 36, 3391–3400. doi:10.1029/2000WR900220

Farajzadeh, R., Matsuura, T., Batenburg, D. van, 2012. Detailed modeling of the alkali/surfactant/polymer (asp) process by coupling a multipurpose reservoir simulator to the chemistry package phreeqc. Reserv. Eval. ….

Feldmann, F., Hagemann, B., Ganzer, L., Panfilov, M., 2016. Numerical simulation of hydrodynamic and gas mixing processes in underground hydrogen storages. Environ. Earth Sci. 75, 1165.

Fillion, E., Noyer, M.-L., 1996. Flow modelling in a dual porosity domain with automatic mesh generation and parameter calibration: application to the Äspö site. J. Hydrol. 180, 1–19. doi:10.1016/0022-1694(95)02896-X

Firoozabadi, A., 1999. Thermodynamics of hydrocarbon reservoirs. McGraw-Hill.

Firoozabadi, A., Cheng, P., 2010. Prospects for subsurface CO_2 sequestration. AIChE J. 56, 1398–1405.

Flemisch, B., Darcis, M., Erbertseder, K., Faigle, B., Lauser, A., Mosthaf, K., Müthing, S., Nuske, P., Tatomir, A., Wolff, M., others, 2011. DuMu x: DUNE for multi-{phase, component, scale, physics,...} flow and transport in porous media. Adv. Water Resour. 34, 1102–1112.

Fredd, C.N., Fogler, H.S., 1998. Influence of transport and reaction on wormhole formation in porous media. AIChE J. 44, 1933–1949. doi:10.1002/aic.690440902

Fu, X., Cueto-Felgueroso, L., Bolster, D., Juanes, R., 2015. Rock dissolution patterns and geochemical shutdown of-brine-carbonate reactions during convective mixing in porous media. J. Fluid Mech. 764, 296–315.

Fučik, R., 2007. http://mmg.fjfi.cvut.cz/~fucik [WWW Document]. URL http://geraldine.fjfi.cvut.cz/~fucik/index.php?page=exact (accessed 4.30.17).

Fučik, R., Mikyška, J., Beneš, M., Illangasekare, T.H., 2008. Semianalytical solution for two-phase flow in porous media with a discontinuity. Vadose Zo. J. 7, 1001–1007.

Fučik, R., Mikyška, J., Beneš, M., Illangasekare, T.H., 2007. An improved semi-analytical solution for verification of numerical models of two-phase flow in porous media. Vadose Zo. J. 6, 93–104.

Gahleitner, G., 2013. Hydrogen from renewable electricity: An international review of power-to-gas pilot plants for stationary applications. Int. J. Hydrogen Energy 38, 2039–2061. doi:10.1016/j.ijhydene.2012.12.010

Galeati, G., Gambolati, G., 1989. On boundary conditions and point sources in the finite element integration of the transport equation. Water Resour. Res. 25, 847–856. doi:10.1029/WR025i005p00847

Gammer, D., Smith, G., Green, A., others, 2011. Energy Technology Institute, in: Offshore Europe.

Garcia-Rios, M., Cama, J., Luquot, L., Soler, J.M., 2014. Interaction between CO_2-rich sulfate solutions and carbonate reservoir rocks from atmospheric to supercritical CO_2 conditions: Experiments and modeling. Chem. Geol. 383, 107–122. doi:http://dx.doi.org/10.1016/j.chemgeo.2014.06.004

Garcia, J.E., 2003. Fluid dynamics of carbon dioxide disposal into saline aquifers. Lawrence Berkeley Natl. Lab.

Garcia, J.E., 2001. Density of aqueous solutions of CO_2, Lawrence Berkeley National Laboratory. Pap. LBNL-49023.

Gasda, S.E., Celia, M.A., Nordbotten, J.M., 2006. Significance of dipping angle on CO2 plume migration in deep saline aquifers, in: Proceedings of the XVI International Conference on Computational Methods in Water Resources.

Gasda, S.E., Nordbotten, J.M., Celia, M.A., 2011. Vertically averaged approaches for CO2 migration with solubility trapping. Water Resour. Res. 47, 5528.

Gharbia, I. Ben, Flauraud, E., Michel, A., 2015. Study of Compositional Multi-Phase Flow Formulations with Cubic EOS, in: SPE Reservoir Simulation Symposium. Society of Petroleum Engineers. doi:10.2118/173249-MS

Ghesmat, K., Hassanzadeh, H., Abedi, J., 2011. The impact of geochemistry on convective mixing in a gravitationally unstable diffusive boundary layer in porous media: CO_2 storage in saline aquifers. J. Fluid Mech. 673, 480–512.

Gislason, S.R., Oelkers, E.H., others, 2014. Carbon storage in basalt. Science (80-.). 344, 373–374.

Goater, A.L., Bijeljic, B., Blunt, M.J., 2013. Dipping open aquifers-The effect of top-surface topography and heterogeneity on CO2 storage efficiency. Int. J. Greenh. Gas Control 17, 318–331.

Goerke, U.-J., Park, C.-H., Wang, W., Singh, A.K., Kolditz, O., 2011. Numerical simulation of multiphase hydromechanical processes induced by CO2 injection into deep saline aquifers. Oil Gas Sci. Technol. dIFP Energies Nouv. 66, 105–118.

Golding, M.J., Huppert, H.E., Neufeld, J.A., 2013. The effects of capillary forces on the axisymmetric propagation of two-phase, constant-flux gravity currents in porous media. Phys. Fluids 25, 36602.

Golding, M.J., Neufeld, J.A., Hesse, M.A., Huppert, H.E., 2011. Two-phase gravity currents in porous media. J. Fluid Mech. 678, 248–270.

Goode, D.J., 1992. Modeling Transport in Transient Ground-Water Flow: An Unacknowledged Approximation. Ground Water 30, 257–261.

Greenbaum, A., 1997. Iterative Methods for Solving Linear Systems. Society for Industrial and Applied Mathematics. doi:10.1137/1.9781611970937

Haas Jr, J.L., 1976. Thermodynamics properties of the coexisting phases and thermochemical properties of the NaCl component in boiling NaCl solutions. US, Geol. Surv., Bull.;(United States) 1421.

Hagemann, B., Rasoulzadeh, M., Panfilov, M., Ganzer, L., Reitenbach, V., 2015. Mathematical modeling of unstable transport in underground hydrogen storage. Environ. Earth Sci. 73, 6891–6898.

Hassanizadeh, M., Gray, W.G., 1979. General conservation equations for multi-phase systems: 2. Mass, momenta, energy, and entropy equations. Adv. Water Resour. 2, 191–203. doi:10.1016/0309-1708(79)90035-6

Hassanzadeh, H., Pooladi-Darvish, M., Keith, D.W., 2007. Scaling behavior of convective mixing, with application to geological storage of CO2. AIChE J. 53, 1121–31.

Haszeldine, R.S., 2009. Carbon capture and storage: how green can black be? Science 80. 325, 1647–52.

Hauke, G., 2001. Simple stabilizing matrices for the computation of compressible flows in primitive variables. Comput. Methods Appl. Mech. Eng. 190, 6881–6893. doi:10.1016/S0045-7825(01)00267-5

Hauke, G., Hughes, T.J.R., 1994. A unified approach to compressible and incompressible flows. Comput. Methods Appl. Mech. Eng. 113, 389–395. doi:10.1016/0045-7825(94)90055-8

He, W., Beyer, C., Fleckenstein, J.H., Jang, E., Kolditz, O., Naumov, D., Kalbacher, T., 2015. A parallelization scheme to simulate reactive transport in the subsurface environment with OGS#IPhreeqc 5.5.7-3.1.2. Geosci. Model Dev. 8, 3333–3348. doi:10.5194/gmd-8-3333-2015

Heide, D., Greiner, M., von Bremen, L., Hoffmann, C., 2011. Reduced storage and balancing needs in a fully renewable European power system with excess wind and solar power generation. Renew. Energy 36, 2515–2523. doi:10.1016/j.renene.2011.02.009

Helgeson, H.C., 1969. Thermodynamics of hydrothermal systems at elevated temperatures and pressures. Am. J. Sci. 267, 729–804.

Helmig, R., 1997. Multiphase flow and transport processes in the subsurface: a contribution to the modeling of hydrosystems. Springer-Verlag.

Hesse, M.A., Orr, F.M., Tchelepi, H.A., 2008. Gravity currents with residual trapping. J. Fluid Mech. 611, 35–60.

Hesse, M., Tchelepi, H.A., Orr, F.M., others, 2006. Scaling analysis of the migration of CO2 in saline aquifers, in: SPE Annual Technical Conference and Exhibition.

Hestenes, M.R., Stiefel, E., 1952. Methods of conjugate gradients for solving linear systems. NBS.

Hewitt, D.R., Neufeld, J.A., Lister, J.R., 2013. Convective shutdown in a porous medium at high Rayleigh number. J. Fluid Mech. 719, 551–586.

Hidalgo, J.J., Carrera, J., 2009. Effect of dispersion on the onset of convection during CO_2 sequestration. J. Fluid Mech. 640, 441–452.

Hidalgo, J.J., Dentz, M., Cabeza, Y., Carrera, J., 2015. Dissolution patterns and mixing dynamics in unstable reactive flow. Geophys. Res. Lett. 42, 6357–6364.

Hidalgo, J.J., Fe, J., Cueto-Felgueroso, L., Juanes, R., 2012. Scaling of convective mixing in porous media. Phys. Rev. Lett. 109, 264503–264507.

Hidalgo, J.J., MacMinn, C.W., Juanes, R., 2013. Dynamics of convective dissolution from a migrating current of carbon dioxide. Adv. Water Resour. 62, 511–519.

Hildenbrand, A., Schlomer, S., Krooss, B.M., 2002. Gas breakthrough experiments on fine-grained sedimentary rocks. Geofluids 2, 3–23. doi:10.1046/j.1468-8123.2002.00031.x

Hildenbrand, A., Schlomer, S., Krooss, B.M., Littke, R., 2004. Gas breakthrough experiments on pelitic rocks: comparative study with N2, CO2 and CH4. Geofluids 4, 61–80. doi:10.1111/j.1468-8123.2004.00073.x

Hill, A.A., Morad, M.R., 2014. Convective stability of carbon sequestration in anisotropic porous media, in: Proceedings of the Royal Society of London A: Mathematical, Physical and Engineering Sciences. p. 20140373.

Hindmarsh, A.C., Brown, P.N., Grant, K.E., Lee, S.L., Serban, R., Shumaker, D.E., Woodward, C.S., 2005. SUNDIALS. ACM Trans. Math. Softw. 31, 363–396. doi:10.1145/1089014.1089020

Hinkelmann, R., 2005. Efficient Numerical Methods and Information-Processing Techniques for Modeling Hydro- and Environmental Systems.

Hoefner, M.L., Fogler, H.S., 1988. Pore evolution and channel formation during flow and reaction in porous media. AIChE J. 34, 45–54.

Hoteit, H., Firoozabadi, A., 2008. Numerical modeling of two-phase flow in heterogeneous permeable media with different capillarity pressures. Adv. Water Resour. 31, 56–73. doi:10.1016/j.advwatres.2007.06.006

Hughes, T.J.R., Mallet, M., 1986. A new finite element formulation for computational fluid dynamics: III. The generalized streamline operator for multidimensional advective-diffusive systems. Comput. Methods Appl. Mech. Eng. 58, 305–328. doi:10.1016/0045-7825(86)90152-0

Hummel, W., Berner, U., Curti, E., Pearson, F., 2002. Nagra/PSI chemical thermodynamic data base 01/01. Radiochimica.

Huyakorn, P.S., Mercer, J.W., Ward, D.S., 1985. Finite Element Matrix and Mass Balance

Computational Schemes for Transport in Variably Saturated Porous Media. Water Resour. Res. 21, 346–358. doi:10.1029/WR021i003p00346

Ide, S.T., Jessen, K., Orr, F.M., 2007. Storage of CO2 in saline aquifers: Effects of gravity, viscous, and capillary forces on amount and timing of trapping. Int. J. Greenh. Gas Control 1, 481–491.

Imhoff, P.T., Jaffé, P.R., Pinder, G.F., 1994. An experimental study of complete dissolution of a nonaqueous phase liquid in saturated porous media. Water Resour. Res. 30, 307–320.

Jacques, D., Šimůnek, J., 2005. User manual of the multicomponent variably-saturated flow and transport model HP1. Descr. Verif. Examples,.

Jacques, D., Simunek, J., Mallants, D., Van Genuchten, M.T., 2006. Operator-splitting errors in coupled reactive transport codes for transient variably saturated flow and contaminant transport in layered soil profiles. J. Contam. Hydrol. 88, 197–218.

Jaffré, J., Sboui, A., 2010. Henry' Law and Gas Phase Disappearance. Transp. Porous Media 82, 521–526. doi:10.1007/s11242-009-9407-0

Jiang, Y., 2008. Techniques for modeling complex reservoirs and advanced wells.

Juanes, R., MacMinn, C.W., Szulczewski, M.L., 2010. The footprint of the CO2 plume during carbon dioxide storage in saline aquifers: storage efficiency for capillary trapping at the basin scale. Transp. porous media 82, 19–30.

Juanes, R., Spiteri, E.J., Orr Jr, F.M., Blunt, M.J., 2006. Impact of relative permeability hysteresis on geological CO2 storage. Water Resour. Res 42, W12418.

Junta de Castilla-Leon, 2015. Anuario Estadistico de Castilla-Leon. Energia.

Kampman, N., Bickle, M., Wigley, M., Dubacq, B., 2014. Fluid flow and CO_2-fluid-mineral interactions during CO_2-storage in sedimentary basins. Chem. Geol. 369, 22–50.

Karimzadeh, L., Lippmann-Pipke, J., Franke, K., Lippold, H., 2017. Mobility and transport of copper(II) influenced by the microbial siderophore DFOB: Column experiment and modelling. Chemosphere 173, 326–329. doi:10.1016/j.chemosphere.2017.01.058

Kim, M.C., Choi, C.K., 2014. Effect of first-order chemical reaction on gravitational instability in a porous medium. Phys. Rev. E 90, 53016.

Kim, M.C., Kim, Y.H., 2015. The effect of chemical reaction on the onset of gravitational instabilities in a fluid saturated within a vertical Hele-Shaw cell: Theoretical and numerical studies. Chem. Eng. Sci. 134, 632–647.

Kioto Protocol, 1997. United Nations framework convention on climate change. Kyoto Protoc. Kyoto.

Kneafsey, T.J., Pruess, K., 2010. Laboratory flow experiments for visualizing carbon dioxide-induced, density-driven brine convection. Transp. Porous Media 82, 123–

139.

Kolditz, O., Bauer, S., Bilke, L., Böttcher, N., Delfs, J.O., Fischer, T., Görke, U.J., Kalbacher, T., Kosakowski, G., McDermott, C.I., Park, C.H., Radu, F., Rink, K., Shao, H., Shao, H.B., Sun, F., Sun, Y.Y., Singh, A.K., Taron, J., Walther, M., Wang, W., Watanabe, N., Wu, Y., Xie, M., Xu, W., Zehner, B., 2012a. OpenGeoSys: an open-source initiative for numerical simulation of thermo-hydro-mechanical/chemical (THM/C) processes in porous media. Environ. Earth Sci. 67, 589–599. doi:10.1007/s12665-012-1546-x

Kolditz, O., Görke, U., Shao, H., Kalbacher, T., Bauer, S., McDermott, C.I., Wang, W., 2012b. Thermo-hydro-mechanical-chemical processes in porous media : benchmarks and examples.

Kolev, N.I., 2007. Solubility of O2, N2, H2 and CO2 in water, in: Multiph. Flow Dyn. 3. Springer, pp. 209–239.

Kosakowski, G., Watanabe, N., 2014. OpenGeoSys-Gem: A numerical tool for calculating geochemical and porosity changes in saturated and partially saturated media. Phys. Chem. Earth, Parts A/B/C 70, 138–149. doi:10.1016/j.pce.2013.11.008

Kruck, O., Crotogino, F., Prelicz, R., Rudolph, T., 2013. HyUnder- Hydrogen Underground Storage at Large Scale:Overview on all Known Under ground Storage Technologies for Hydrogen Deliverabl, 1–93.

Kumar, A., Noh, M.H., Ozah, R.C., Pope, G.A., Bryant, S.L., Sepehrnoori, K., Lake, L.W., others, 2005. Reservoir simulation of CO2 storage in aquifers. Spe J. 10, 336–348.

Lackner, K.S., 2003. A guide to CO_2 sequestration. Science (80-.). 300, 1677–1678.

Lanczos, C., 1952. Solution of systems of linear equations by minimized iterations. J. Res. Nat. Bur. Stand. 49, 33–53.

Landinger, H., Buenger, U., Raksha, T., Weindorf, W., Simon, J., Correas, L., Crotogino, F., 2014. HyUnder- Hydrogen Underground Storage at Large Scale: Update of Benchmarking of large scale hydrogen underground storage with competing options Deliverabl, 1–74.

Lauser, A., Hager, C., Helmig, R., Wohlmuth, B., 2011. A new approach for phase transitions in miscible multi-phase flow in porous media. Adv. Water Resour. 34, 957–966. doi:10.1016/j.advwatres.2011.04.021

Le Gallo, Y., Trenty, L., Michel, A., Vidal-Gilbert, S., Parra, T., Jeannin, L., 2006. Long-term flow simulations of CO2 storage in saline aquifer, in: Proceedings of the GHGT8 Conference-Trondheim (Norway). pp. 18–22.

Leighty, W.C., 2008. Running the world on renewables: hydrogen transmission pipelines with firming geologic storage, in: ASME 2008 Power Conference. pp. 601–613.

Leon, J.M., Martin, A.P., Garcia-Riosa, M., Reguera Garcia, I., Garcia Lobon, J.L., 2010. ALGECO2. Plan de seleccion y caracterizacion de areas y estructuras favorables para el Almacenamiento Geologico de CO2 en España. IGME 1–164.

Lichtner, P.C., 1985. Continuum model for simultaneous chemical reactions and mass transport in hydrothermal systems. Geochim. Cosmochim. Acta 49, 779–800. doi:10.1016/0016-7037(85)90172-3

linalg/spooles [WWW Document], 2017. URL http://www.netlib.org/linalg/spooles/ (accessed 5.8.17).

Loodts, V., Thomas, C., Rongy, L., De Wit, A., 2014. Control of convective dissolution by chemical reactions: general classification and application to CO_2 dissolution in reactive aqueous solutions. Phys. Rev. Lett. 113, 114501.

Lord, A.S., 2009. Overview of geologic storage of natural gas with an emphasis on assessing the feasibility of storing hydrogen. SAND2009-5878, Sandia Natl. Lab. Albuquerque, NM.

Lord, A.S., Kobos, P.H., Borns, D.J., 2014. Geologic storage of hydrogen: Scaling up to meet city transportation demands. Int. J. Hydrogen Energy 39, 15570–15582. doi:10.1016/j.ijhydene.2014.07.121

Lu, C., Lichtner, P., Hammond, G.E., Mills, R.T., 2010. Evaluating variable switching and flash methods in modeling carbon sequestration in deep geologic formations using PFLOTRAN. Proc. SciDAC.

Lu, C., Lichtner, P.C., 2005. PFLOTRAN: Massively parallel 3-D simulator for CO2 sequestration in geologic media, in: DOE-NETL Fourth Annual Conference on Carbon Capture and Sequestration.

MacDonald, R.C., Coats, K.., 1970. Methods for Numerical Simulation of Water and Gas Coning. Trans. AIME 10, 425–436. doi:10.2118/2796-PA

MacMinn, C.W., Juanes, R., 2013. Buoyant currents arrested by convective dissolution. Geophys. Res. Lett. 40, 2017–2022.

MacMinn, C.W., Neufeld, J.A., Hesse, M.A., Huppert, H.E., 2012. Spreading and convective dissolution of carbon dioxide in vertically confined, horizontal aquifers. Water Resour. Res. 48, 11516–11526.

MacMinn, C.W., Szulczewski, M.L., Juanes, R., 2011. CO2 migration in saline aquifers. Part 2. Capillary and solubility trapping. J. Fluid Mech. 688, 321–351.

MacMinn, C.W., Szulczewski, M.L., Juanes, R., 2010. CO2 migration in saline aquifers. Part 1. Capillary trapping under slope and groundwater flow. J. Fluid Mech. 662, 329–351.

Marcondes, F., Maliska, C.R., Zambaldi, M.C., 2009. A comparative study of implicit and explicit methods using unstructured voronoi meshes in petroleum reservoir simulation. J. Brazilian Soc. Mech. Sci. Eng. 31, 353–361.

Martinez, R., Suarez, I., Zapatero, M.A., Saftic, B., Kolenkovic, I., Car, M., Persoglia, S., Donda, F., 2009. The EU GeoCapacity project. Saline aquifers storage capacity in group south countries. Energy Procedia 1, 2733–2740.

Masson, R., Trenty, L., Zhang, Y., 2014. Formulations of two phase liquid gas compositional Darcy flows with phase transitions. Int. J. Finite Vol. 11, pp.34.

Mayer, K., MacQuarrie, K., 2010. Solution of the MoMaS reactive transport benchmark with MIN3P—model formulation and simulation results. Comput. Geosci.

McWhorter, D.B., Sunada, D.K., 1992. Reply [to "Comment on 'Exact integral solutions for two-phase flow' by David B. McWhorter and Daniel K. Sunada"]. Water Resour. Res. 28, 1479–1479. doi:10.1029/92WR00474

McWhorter, D.B., Sunada, D.K., 1990. Exact integral solutions for two-phase flow. Water Resour. Res. 26, 399–413.

Meeussen, J.C.L., 2003. ORCHESTRA: An Object-Oriented Framework for Implementing Chemical Equilibrium Models. doi:10.1021/ES025597S

Metz, B., Davidson, O., de Coninck, H., Loos, M., Meyer, L., others, 2005. IPCC special report on carbon dioxide capture and storage. Cambridge University Press.

Meybodi, H.-E., Hassanzadeh, H., 2013. Stability analysis of two-phase buoyancy-driven flow in the presence of a capillary transition zone. Phys. Rev. E 87, 33009. doi:10.1103/PhysRevE.87.033009

Michael, K., Golab, A., Shulakova, V., Ennis-King, J., Allinson, G., Sharma, S., Aiken, T., 2010. Geological storage of CO2 in saline aquifers - a review of the experience from existing storage operations. Int. J. Greenh. Gas Control 4, 659–667.

Michelsen, M.L., Mollerup, J., Breil, M.P., 2008. Thermodynamic Models: Fundamental & Computational Aspects.

Miller, C.T., Poirier-McNeil, M.M., Mayer, A.S., 1990. Dissolution of Trapped Nonaqueous Phase Liquids: Mass Transfer Characteristics. Water Resour. Res. 26, 2783–2796. doi:10.1029/WR026i011p02783

Mills, R.T., Lu, C., Lichtner, P.C., Hammond, G.E., 2007. Simulating subsurface flow and transport on ultrascale computers using PFLOTRAN. J. Phys. Conf. Ser. 78, 12051. doi:10.1088/1742-6596/78/1/012051

Molins, S., Carrera, J., Ayora, C., Saaltink, M.W., 2004. A formulation for decoupling components in reactive transport problems. Water Resour. Res. 40. doi:10.1029/2003WR002970

Mondelli, C., Bardelli, F., Vitillo, J.G., Didier, M., Brendle, J., Cavicchia, D.R., Robinet, J.-C., Charlet, L., 2015. Hydrogen adsorption and diffusion in synthetic Na-montmorillonites at high pressures and temperature. Int. J. Hydrogen Energy 40, 2698–2709. doi:10.1016/j.ijhydene.2014.12.038

Morway, E.D., Niswonger, R.G., Langevin, C.D., Bailey, R.T., Healy, R.W., 2012. Modeling Variably Saturated Subsurface Solute Transport with MODFLOW-UZF and MT3DMS. Ground Water no-no. doi:10.1111/j.1745-6584.2012.00971.x

Motis, K., Grandia, F., Credoz, A., del Olmo, W., 2012. A potential site for CO2 geological storage: Los Paramos (Burgos, N Spain)., in: Proceedings of the VIII Spanish Geological Congress.

MUMPS Credits [WWW Document], 2017. URL http://mumps.enseeiht.fr/index.php?page=credits (accessed 5.8.17).

Muskat, M., 1949. Principles of Oil Production. McGraw Hill Book Co., New York.

Nardi, A., Idiart, A., Trinchero, P., de Vries, L.M., Molinero., J., 2014a. Interface COMSOL-PHREEQC (iCP), an efficient numerical framework for the solution of coupled multiphysics and geochemistry. Comput. Geosci. 69, 10–21.

Nardi, A., Sáinz-García, A., de Vries, L.M., Bayer, M., Trinchero, P., Idiart, A., Pekala, M., Abarca, E., Silva, O., Molinero, J., 2014b. iCP, Interface COMSOL PHREEQC User's guide.

Nasir, O., Fall, M., Evgin, E., 2014. A simulator for modeling of porosity and permeability changes in near field sedimentary host rocks for nuclear waste under climate change influences. Tunn. Undergr. Sp. Technol. 42, 122–135. doi:10.1016/j.tust.2014.02.010

Nedelec, J.C., 1980. Mixed finite elements in R3. Numer. Math. 35, 315–341. doi:10.1007/BF01396415

Neufeld, J.A., Hesse, M.A., Riaz, A., Hallworth, M.A., Tchelepi, H.A., Huppert, H.E., 2010. Convective dissolution of carbon dioxide in saline aquifers. Geophys. Res. Lett. 37.

Neumann, R., Bastian, P., Ippisch, O., 2013. Modeling and simulation of two-phase two-component flow with disappearing nonwetting phase. Comput. Geosci. 17, 139–149. doi:10.1007/s10596-012-9321-3

Nickalls, R.W.D., 1993. A new approach to solving the cubic: Cardan's solution revealed. Math. Gaz. 77, 354–359.

Niessner, J., Hassanizadeh, S.M., 2009. Modeling kinetic interphase mass transfer for two-phase flow in porous media including fluid--fluid interfacial area. Transp. porous media 80, 329–344.

Niessner, J., Hassanizadeh, S.M., 2008. A model for two-phase flow in porous media including fluid-fluid interfacial area. Water Resour. Res. 44, n/a-n/a. doi:10.1029/2007WR006721

Niessner, J., Helmig, R., 2007. Multi-scale modeling of three-phase–three-component processes in heterogeneous porous media. Adv. Water Resour. 30, 2309–2325. doi:10.1016/j.advwatres.2007.05.008

Nordbotten, J.M., Celia, M.A., 2006. An improved analytical solution for interface upconing around a well. Water Resour. Res. 42. doi:10.1029/2005WR004738

Nordbotten, J.M., Celia, M.A., Bachu, S., 2005. Injection and Storage of CO2 in Deep Saline Aquifers: Analytical Solution for CO2 Plume Evolution During Injection.

Transp. Porous Media 58, 339–360. doi:10.1007/s11242-004-0670-9

Nordbotten, J.M., Celia, M.A., Bachu, S., 2004a. Analytical solutions for leakage rates through abandoned wells. Water Resour. Res. 40. doi:10.1029/2003WR002997

Nordbotten, J.M., Celia, M.A., Bachu, S., Dahle, H.K., 2004b. Semianalytical Solution for CO2 Leakage through an Abandoned Well. doi:10.1021/ES035338I

Nordbotten, J.M., Dahle, H.K., 2011. Impact of the capillary fringe in vertically integrated models for CO2 storage. Water Resour. Res. 47, 2537.

Nordbotten, J.M., Kavetski, D., Celia, M.A., Bachu, S., 2009. A semi-analytical model estimating leakage associated with CO2 storage in large-scale multi-layered geological systems with multiple leaky wells. Environ. Sci. Technol. 43, 743–749.

Nuche, R., 2003. Patrimonio geológico de Castilla-La Mancha. ENRESA, Madrid.

Oelkers, E.H., Cole, D.R., 2008. Carbon dioxide sequestration a solution to a global problem. Elements 4, 305–310.

Orr Jr, F.M., 2009. CO_2 capture and storage: are we ready? Energy Environ. Sci. 2, 449–458.

Ozarslan, A., 2012. Large-scale hydrogen energy storage in salt caverns. Int. J. Hydrogen Energy 37, 14265–14277. doi:10.1016/j.ijhydene.2012.07.111

Pachauri, R.K., Allen, M.R., Barros, V.R., Broome, J., Cramer, W., Christ, R., Church, J.A., Clarke, L., Dahe, Q., Dasgupta, P., others, 2014. IPPCC,Climate change 2014: synthesis Report. Contribution of working groups I, II and III to the fifth assessment report of the intergovernmental panel on climate change. IPCC.

Panfilov, M., 2016. 4.1 Underground hydrogen storage as an element of energy cycle. Compend. Hydrog. Energy Hydrog. Storage, Distrib. Infrastruct. 91.

Panfilov, M., 2010. Hydrogen underground storage: natural methane generation and in-situ self-organisation. GAS 30–37.

Panfilov, M., Gravier, G., Fillacier, S., 2006. Underground storage of H_2 and H_2-CO_2-CH_4 mixtures, in: ECMOR X-10th Eur. Conf. Math. Oil Recover.

PARDISO 5.0.0 Solver Project [WWW Document], 2017.

Paris Agreement, 2015. United Nations. United Nations Treaty Collect. 1–27.

Parkhurst, D.L., Appelo, C.A.J., 2013. Description of input and examples for PHREEQC version 3: a computer program for speciation, batch-reaction, one-dimensional transport, and inverse geochemical calculations.

Parkhurst, D.L., Kipp, K.L., Charlton, S.R., 2010. PHAST Version 2—A Program for Simulating Groundwater Flow, Solute Transport, and Multicomponent Geochemical Reactions.

Paterson, L., 1983. The implications of fingering in underground hydrogen storage. Int. J. Hydrogen Energy 8, 53–59. doi:10.1016/0360-3199(83)90035-6

Pau, G.S.H., Bell, J.B., Pruess, K., Almgren, A.S., Lijewski, M.J., Zhang, K., 2010. High-resolution simulation and characterization of density-driven flow in CO_2 storage in saline aquifers. Adv. Water Resour. 33, 443–455.

Pawar, R.J., Zyvoloski, G.A., Tenma, N., Sakamoto, Y., Komai, T., 2005. Numerical simulation of laboratory experiments on methane hydrate dissociation, in: The Fifteenth International Offshore and Polar Engineering Conference. International Society of Offshore and Polar Engineers.

Peaceman, D., 1977. Fundamentals of numerical reservoir engineering.

Pfeiffer, W.T., al Hagrey, S.A., Köhn, D., Rabbel, W., Bauer, S., 2016. Porous media hydrogen storage at a synthetic, heterogeneous field site: numerical simulation of storage operation and geophysical monitoring. Environ. Earth Sci. 75, 1–18. doi:10.1007/s12665-016-5958-x

Pfeiffer, W.T., Beyer, C., Bauer, S., 2017. Hydrogen storage in a heterogeneous sandstone formation: dimensioning and induced hydraulic effects. Pet. Geosci. petgeo2016-050. doi:10.1144/petgeo2016-050

Phillips, S.L., Igbene, A., Fair, J.A., Ozbek, H., Tavana, M., 1981. A technical databook for geothermal energy utilization, Lawrence Berkeley National Laboratory.

Plummer, L., Wigley, T., Parkhurst, D., 1978. The Kinetics of Calcite Dissolution in CO2-Water Systems at 5^o to 60^oC and 0.0 to 1.0 ATM CO2. Am. J. Sci. 278, 179–216.

Poblete Piedrabuena, M.Á., n.d. Las últimas manifestaciones asociadas al vulcanismo del Campo de Calatrava (Ciudad Real): los manantiales termales.

Pokrovsky, O.S., Golubev, S. V, Schott, J., Castillo, A., 2009. Calcite, dolomite and magnesite dissolution kinetics in aqueous solutions at acid to circumneutral pH, 25 to 150 ^{o}C and 1 to 55 atm pCO2: New constraints on CO2 sequestration in sedimentary basins. Chem. Geol. 265, 20–32.

Powers, S.E., Abriola, L.M., Dunkin, J.S., Weber, W.J., 1994. Phenomenological models for transient NAPL-water mass-transfer processes. J. Contam. Hydrol. 16, 1–33.

Powers, S.E., Abriola, L.M., Weber, W.J., 1992. An experimental investigation of nonaqueous phase liquid dissolution in saturated subsurface systems: Steady state mass transfer rates. Water Resour. Res. 28, 2691–2705.

Pruess, K., 2008. Numerical modeling studies of the dissolution-diffusion-convection process during CO_2 storage in saline aquifers. Lawrence Berkeley Natl. Lab.

Pruess, K., Oldenburg, C.M., Moridis, G.J., 1999. TOUGH2 User's Guide Version 2. Lawrence Berkeley Natl. Lab.

Pruess, K., Spycher, N., 2007. ECO2N - A fluid property module for the TOUGH2 code for studies of CO2 storage in saline aquifers. Energy Convers. Manag. 48, 1761–1767.

doi:10.1016/j.enconman.2007.01.016

Rapaka, S., Chen, S., Pawar, R.J., Stauffer, P.H., Zhang, D., 2008. Non-modal growth of perturbations in density-driven convection in porous media. J. Fluid Mech. 609, 285–303.

Raviart, P.A., Thomas, J.M., 1977. A mixed finite element method for 2-nd order elliptic problems. Springer, Berlin, Heidelberg, pp. 292–315. doi:10.1007/BFb0064470

Redlich, O., Kwong, J.N.S., 1949. On the thermodynamics of solutions. V. An equation of state. Fugacities of gaseous solutions. Chem. Rev. 44, 233–244.

REE-Red Electrica de España, 2016. Estadisticas del sistem electricctrico español. Series estadisticas por comunidades autonomas. Intern. Rep.

REE-Red Electrica de España, 2011. Limites del sistema electrico a la integracion de generacion de regimen especial. Intern. Rep. 1–4.

Reed, W., Hill, T., 1973. Triangularmesh methodsfor the neutrontransportequation. Los Alamos Rep. LA-UR-73-479.

Riaz, A., Hesse, M., Tchelepi, H.A., Orr, F.M., 2006. Onset of convection in a gravitationally unstable diffusive boundary layer in porous media. J. Fluid Mech. 548, 87–111.

Rio Summit, 1992. United Nations Conference on Environment and Development. Earth Summit.

Robinson, D.B., Peng, D.-Y., 1978. The characterization of the heptanes and heavier fractions for the GPA Peng-Robinson programs. Gas Processors Association.

Russell, T.F., 1989. Stability Analysis and Switching Criteria for Adaptive Implicit Methods Based on the CFL Condition, in: SPE Symposium on Reservoir Simulation. Society of Petroleum Engineers. doi:10.2118/18416-MS

Saad, Y., 2003. Iterative Methods for Sparse Linear Systems. Society for Industrial and Applied Mathematics. doi:10.1137/1.9780898718003

Saad, Y., 1993. A Flexible Inner-Outer Preconditioned GMRES Algorithm. SIAM J. Sci. Comput. 14, 461–469. doi:10.1137/0914028

Saad, Y., Schultz, M.H., 1986. GMRES: A Generalized Minimal Residual Algorithm for Solving Nonsymmetric Linear Systems. SIAM J. Sci. Stat. Comput. 7, 856–869. doi:10.1137/0907058

Saaltink, M.W., Ayora, C., Carrera, J., 1998. A mathematical formulation for reactive transport that eliminates mineral concentrations. Water Resour. Res. 34, 1649–1656. doi:10.1029/98WR00552

Saaltink, M.W., Carrera, J., Ayora, C., 2000. A comparison of two approaches for reactive transport modelling. J. Geochemical Explor. 69, 97–101.

Saaltink, M.W., Carrera, J., Olivella, S., 2004. Mass balance errors when solving the convective form of the transport equation in transient flow problems. Water Resour. Res. 40, W05107--1.

Saaltink, M.W., Carrera, J.J., Ayora, C., 2001. On the behavior of approaches to simulate reactive transport. J. Contam. Hydrol. 48, 213–235. doi:10.1016/S0169-7722(00)00172-8

Saaltink, Pifarré, F.B., Ayora, C., Carrera, J., Pastallé, S.O., 2004. RETRASO, a code for modeling reactive transport in saturated and unsaturated porous media. Geol. Acta 2, 235–251. doi:10.1344/105.000001430

Sainz-Garcia, A., Abarca, E., Grandia, F., 2016. Efficiency and impacts of hythane (CH4+ H2) underground storage, in: EGU General Assembly Conference Abstracts. p. 16603.

Sainz-Garcia, A., Abarca, E., Nardi, A., Grandia, F., Oelkers, E.H., 2017. Convective mixing fingers and chemistry interaction in carbon storage. Int. J. Greenh. Gas Control 58, 52–61. doi:10.1016/j.ijggc.2016.12.005

Samper, J., Yang, C., Montenegro, L., 2003. CORE2D version 4: A code for non-isothermal water flow and reactive solute transport. Users Manual. Univ. La Coruña, Spain.

Sathaye, K.J., Hesse, M.A., Cassidy, M., Stockli, D.F., 2014. Constraints on the magnitude and rate of CO_2 dissolution at Bravo Dome natural gas field. Proc. Natl. Acad. Sci. 111, 15332–15337.

Sbai, M.A., 2007. A double porosity—double permeability model of the Bouillante geothermal production field (Guadeloupe). Technical Report RP-55418-FR, BRGM.

Settari, A., Aziz, K., 1975. Treatment of nonlinear terms in the numerical solution of partial differential equations for multiphase flow in porous media. Int. J. Multiph. Flow 1, 817–844. doi:10.1016/0301-9322(75)90037-3

Shao, H., Dmytrieva, S. V., Kolditz, O., Kulik, D.A., Pfingsten, W., Kosakowski, G., 2009. Modeling reactive transport in non-ideal aqueous–solid solution system. Appl. Geochemistry 24, 1287–1300. doi:10.1016/j.apgeochem.2009.04.001

Sheldon, J.W., Cardwell, W.T.J., 1959. One-Dimensional, Incompressible, Noncapillary, Two-Phase Fluid Flow in a Porous Medium. Pet. Trans. AIME 216, 290–296.

Sidborn, M., Sandström, B., Tullborg, E., Delos, A., 2010. SR-Site: Oxygen ingress in the rock at Forsmark during a glacial cycle, Swedish Nuclear Fuel. doi:SKB TR-10-57

Šimůnek, J., Genuchten, M. Van, 2006. The HYDRUS software package for simulating two-and three-dimensional movement of water, heat, and multiple solutes in variably-saturated media. Tech. manual,.

Šimůnek, J., Šejna, M., Saito, H., Sakai, M., 2009. The HYDRUS-1D Package for Simulating the Movement of Water, Heat, and Multiple Solutes in Variably Saturated Media, Version 4.08. Environ. Sci. ….

Sin, I., 2015. Numerical simulation of compressible two-phase flow and reactive transport in porous media-Applications to the study of CO2 storage and natural gas reservoir. Ec. Natl. Supérieure des Mines Paris.

Sin, I., Lagneau, V., Corvisier, J., 2017. Integrating a compressible multicomponent two-phase flow into an existing reactive transport simulator. Adv. Water Resour. 100, 62–77. doi:10.1016/j.advwatres.2016.11.014

Slim, A., Ramakrishnan, T., 2010. Onset and cessation of time-dependent, dissolution-driven convection in porous media. Phys. Fluids 22, 1–11.

Slim, A.C., 2014. Solutal-convection regimes in a two-dimensional porous medium. J. Fluid Mech. 741, 461–491.

Smith, W., Missen, R., 1982. Chemical reaction equilibrium analysis: theory and algorithms, John Wiley and Sons, xvi+ 364, 23 x 15 cm, illustrated.

Sousa, E. de, 2012. Groundwater modelling meets geochemistry: Building the bridge between FEFLOW and PHREEQC with IFMPhreeqc, in: International Mine Water Association .

Sovova, H., Prochazka, J., 1993. Calculations of compressed carbon dioxide viscosities. Ind. Eng. Chem. Res. 32, 3162–3169.

Spycher, N., Pruess, K., 2005. CO2-H2O mixtures in the geological sequestration of CO2. II. Partitioning in chloride brines at 12-100 ^{o}C and up to 600 bar. Geochim. Cosmochim. Acta 69, 3309–3320.

Steefel, C., 2009. CrunchFlow software for modeling multicomponent reactive flow and transport. User’s manual. Earth Sci. Div. Lawrence Berkeley, Natl.

Steefel, C.I., Appelo, C.A.J., Arora, B., Jacques, D., Kalbacher, T., Kolditz, O., Lagneau, V., Lichtner, P.C., Mayer, K.U., Meeussen, J.C.L., Molins, S., Moulton, D., Shao, H., Šimůnek, J., Spycher, N., Yabusaki, S.B., Yeh, G.T., 2015. Reactive transport codes for subsurface environmental simulation. Comput. Geosci. 19, 445–478. doi:10.1007/s10596-014-9443-x

Steefel, C.I., MacQuarrie, K.T.B., 1996. Approaches to modeling of reactive transport in porous media. Rev. Mineral. Geochemistry 34.

Stenhouse, M., 2009. Natural and industrial analogues for geological storage of carbon dioxide. IEA Greenh. Gas R&D Program. Cheltenham, UK.

Stocker, T.F., Qin, D., Plattner, G.-K., Tignor, M., Allen, S.K., Boschung, J., Nauels, A., Xia, Y., Bex, V., Midgley, P.M., 2013. IPCC, CLimate Change 2013: The Physical Science Basis. Contribution of Working Group I to the Fifth Assessment Report of the Intergovernmental Panel on Climate Change. Clim. Chang. 2013 5, 1535.

Stone, H.L., Garder, A.O., 1961. Analysis of Gas-Cap or Dissolved-Gas Drive Reservoirs. Soc. Pet. Eng. J. 1, 92–104. doi:10.2118/1518-G

Strang, G., 1968. On the Construction and Comparison of Difference Schemes. SIAM J.

Numer. Anal. 5, 506–517. doi:10.1137/0705041

Szulczewski, M.L., Juanes, R., 2013. The evolution of miscible gravity currents in horizontal porous layers. J. Fluid Mech. 719, 82–96.

Szulczewski, M.L., MacMinn, C.W., Herzog, H.J., Juanes, R., 2012. Lifetime of carbon capture and storage as a climate-change mitigation technology. Proc. Natl. Acad. Sci. 109, 5185–5189.

Talman, S.J., Wiwchar, B., Gunter, W.D., Scarge, C.M., 1990. Dissolution kinetics of calcite in the H_2O-CO_2 system along the steam saturation curve to 210 C. Fluid-Mineral Interact. A Tribut. to HP Eugster 41–55.

Tatomir, A.B., Schaffer, M., Kissinger, A., Hommel, J., Nuske, P., Licha, T., Helmig, R., Sauter, M., 2015. Novel approach for modeling kinetic interface-sensitive (KIS) tracers with respect to time-dependent interfacial area change for the optimization of supercritical carbon dioxide injection into deep saline aquifers, International Journal of Greenhouse Gas Control. doi:10.1016/j.ijggc.2014.11.020

Taylor, J.B., Alderson, J.E.A., Kalyanam, K.M., Lyle, A.B., Phillips, L.A., 1986. Technical and economic assessment of methods for the storage of large quantities of hydrogen. Int. J. Hydrogen Energy 11, 5–22. doi:10.1016/0360-3199(86)90104-7

Thomas, G.W., Thurnau, D.H., 1983. Reservoir Simulation Using an Adaptive Implicit Method. Soc. Pet. Eng. J. 23, 759–768. doi:10.2118/10120-PA

Tillier, E., Michel, A., Trenty, L., 2007. Coupling a multiphase flow model and a reactive transport model for CO2 storage modeling. Comp. Meth. Coupled Probl. Sci. Eng.

Toleukhanov, A., Panfilov, M., Panfilova, I., Kaltayev, A., 2012. Bio-reactive two-phase transport and population dynamics in underground storage of hydrogen: natural self-organisation, in: ECMOR XIII-13th European Conference on the Mathematics of Oil Recovery.

Trenty, L., Michel, A., Tillier, E., Le Gallo, Y., 2006. A sequential splitting strategy for CO2 storage modelling, in: ECMOR X-10th European Conference on the Mathematics of Oil Recovery.

Truche, L., Berger, G., Destrigneville, C., Guillaume, D., Giffaut, E., 2010. Kinetics of pyrite to pyrrhotite reduction by hydrogen in calcite buffered solutions between 90 and 180 C: Implications for nuclear waste disposal. Geochim. Cosmochim. Acta 74, 2894–2914.

Tsai, C., Yeh, G., Ni, C., 2013. HYDROGEOCHEM 6.0: A Model to Couple Thermal-Hydrology-Mechanics-Chemical (THMC) Processes USER GUIDE.

Van der Lee, J., Windt, L. De, Lagneau, V., 2003. Module-oriented modeling of reactive transport with HYTEC. Comput. Geosci.

van der Vorst, H.A., 1992. Bi-CGSTAB: A Fast and Smoothly Converging Variant of Bi-CG for the Solution of Nonsymmetric Linear Systems. SIAM J. Sci. Stat. Comput. 13, 631–644. doi:10.1137/0913035

van Genuchten, M.T., 1980. A Closed-form Equation for Predicting the Hydraulic Conductivity of Unsaturated Soils1. Soil Sci. Soc. Am. J. 44, 892. doi:10.2136/sssaj1980.03615995004400050002x

VanAntwerp, D.J., Falta, R.W., Gierke, J.S., 2008. Numerical Simulation of Field-Scale Contaminant Mass Transfer during Air Sparging. Vadose Zo. J. 7, 294. doi:10.2136/vzj2006.0126

Vilarrasa, V., 2012. Thermo-hydro-mechanical impacts of carbon dioxide (CO2) injection in deep saline aquifers.

Voskov, D. V., Tchelepi, H.A., 2012. Comparison of nonlinear formulations for two-phase multi-component EoS based simulation. J. Pet. Sci. Eng. 82, 101–111. doi:10.1016/j.petrol.2011.10.012

Vostrikov, V., 2014. Numerical simulation of two-phase multicomponent flow with reactive transport in porous media.

Ward, T.J., Cliffe, K.A., Jensen, O.E., Power, H., 2014. Dissolution-driven porous-medium convection in the presence of chemical reaction. J. Fluid Mech. 747, 316–349.

Wei, L., 2012. Sequential Coupling of Geochemical Reactions With Reservoir Simulations for Waterflood and EOR Studies. SPE J. 17, 469–484. doi:10.2118/138037-PA

Westerink, J.J., Shea, D., 1989. Consistent higher degree Petrov-Galerkin methods for the solution of the transient convection-diffusion equation. Int. J. Numer. Methods Eng. 28, 1077–1101. doi:10.1002/nme.1620280507

Wheeler, J., Wheeler, M.F., 2001. Integrated parallel and accurate reservoir simulator. Univ. Texas Austin.

White, M., Oostrom, M., 2006. STOMP: Subsurface Transport Over Multiple Phases, Version 4.0, User’s Guide. 2006. Pacific Northwest Natl. Lab. Richland, ….

Wissmeier, L., Barry, D.A., 2011. Simulation tool for variably saturated flow with comprehensive geochemical reactions in two- and three-dimensional domains. Environ. Model. Softw. 26, 210–218. doi:10.1016/j.envsoft.2010.07.005

Woods, A.W., Espie, T., 2012. Controls on the dissolution of CO2 plumes in structural traps in deep saline aquifers. Geophys. Res. Lett. 39, 8401--.

Xu, T., Apps, J.A., Pruess, K., 2005. Mineral sequestration of carbon dioxide in a sandstone--shale system. Chem. Geol. 217, 295–318.

Xu, T., Sonnenthal, E., Spycher, N., Pruess, K., 2006. TOUGHREACT-a simulation program for non-isothermal multiphase reactive geochemical transport in variably saturated geologic media: applications to geothermal injectivity and CO 2 geological sequestration. Comput. \& Geosci. 32, 145–165. doi:10.1016/j.cageo.2005.06.014

Xu, X., Chen, S., Zhang, D., 2006. Convective stability analysis of the long-term storage of carbon dioxide in deep saline aquifers. Adv. Water Resour. 29, 397–407.

Yang, C., and Yongan Gu, 2006. Accelerated mass transfer of CO_2 in reservoir brine due to density-driven natural convection at high pressures and elevated temperatures. Ind. Eng. Chem. Res. 45, 2430–2436. doi:10.1021/ie050497r

Yeh, G.-T., Tripathi, V.S., 1989. A critical evaluation of recent developments in hydrogeochemical transport models of reactive multichemical components. Water Resour. Res. 25, 93–108.

Yeh, G., Tripathi, V., Gwo, J., Cheng, H., 2012. Hydrogeochem: A coupled model of variably saturated flow, thermal transport, and reactive biogeochemical transport. Groundwater.

Yélamos, J.G., Redondo, R., Castro, F. De, Galván, A., Martínez-Rubio, J., Rebollo, L., Ruano, P., Senderos, A., Villarroya, F.I., 1999. Hidrogeoquímica y microbiología en Los Hervideros del Campo de Calatrava (Ciudad Real). Geogaceta 115–118.

Zapatero-Rodriguez, M.A., Suare-Diaz, I., Arenillas-Gonzalez, A., Catalina-Nita, R., Martinez-Orio, R., 2009. Project Geocapacity: Estimation of the european capacity for CO2 storage. The Spanish case. IGME 1–157.

Zhang, H., Schwartz, F.W., 2000. Simulating the in situ oxidative treatment of chlorinated ethylenes by potassium permanganate. Water Resour. Res. 36, 3031–3042. doi:10.1029/2000WR900173

Zhang, R., Hu, S., Zhang, X., Yu, W., 2007. Dissolution kinetics of dolomite in water at elevated temperatures. Aquat. Geochemistry 13, 309–338.

Zhao, B., MacMinn, C.W., Szulczewski, M.L., Neufeld, J.A., Huppert, H.E., Juanes, R., 2013. Interface pinning of immiscible gravity-exchange flows in porous media. Phys. Rev. E 87, 23015.

Zienkiewicz, O.C., Nithiarasu, P., Taylor, R.L., 2005. The finite element method for fluid dynamics. Butterworth-Heinemann.

Zuo, L., Krevor, S., Falta, R.W., Benson, S.M., 2012. An experimental study of CO_2 exsolution and relative permeability measurements during CO_2 saturated water depressurization. Transp. porous media 91, 459–478.